DOCTOR OF PHILOSOPHY

Temporal and spectral dynamics of coupled external cavity laser diodes

Ludwikow, Marek

Award date:
2011

Awarding institution:
Bangor University

[Link to publication](#)

Temporal and spectral dynamics of coupled external cavity laser diodes

PRIFYSGOL

BANGOR

UNIVERSITY

1884

Marek Jerzy Ludwików

School of Electronic Engineering

Bangor University

A thesis submitted in candidature for the degree of

Doctor of Philosophy

March 2011

Abstract

This thesis studies, both practical and theoretical, aspects of the synchronisation locking process of two external-cavity semiconductor lasers, optically coupled in a Master–Slave configuration. Such configurations have been the subject of a significant number of numerical and experimental investigations, mainly motivated by the desire to develop a secure communications scheme.

This thesis investigates the robustness of the chaos synchronisation process to parameter mismatch with regard to both experimentally adjustable parameters (optical injection ramping time between 0.4 ps and 10 ns, and optical injection strength between 3 and 164 ns^{-1}), and a range of intrinsic laser diode parameters (carrier lifetime between 2 and 4 ns, and linewidth enhancement factor between 4.0 and 6.5). A multiple averaging approach was adopted as a means of ascertaining the global effect these parameters have on the locking process. The dynamics induced by an introduced optical chopper to the injection arm were investigated for the first time and a previously unreported switching processes observed.

The spectral and temporal dynamics of both the TE–TM emission were investigated in an external-cavity laser diode configuration where the optical feedback was sufficient to induce chaotic oscillations. Specifically, the TM mode was observed to lase at various levels of feedback. Three possible explanations of the instabilities seen in the recorded spectra and the corresponding L–I curves were provided.

The tendency for entropy to increase in isolated systems is expressed in the second law of thermodynamics—perhaps the most pessimistic and amoral formulation in all human thought.

G. Hill and K. Thornley, *Principia Discordia* (1965)

Acknowledgments

First and foremost, I would like to express my sincerest gratitude for my supervisor Prof. **Paul S. Spencer** for his patience, guidance, and forbearance towards my somewhat lengthy approach to writing up. Everything I have ever needed to know about constructing and aligning chaos-synchronisation set-ups, I have gained from Drs **Jon Paul**, **Min Won Lee**, and **Yanhua Hong**. I am very grateful for their help, experimental know-how, and laser safety precautions which all greatly contributed to the general outlook of chapters 3 and 6. Twelve-hour-long marathons of staring at little red dots in a pitch-black lab would not have been the same without them. I also wish to thank **Sam J. Lea** for his Fortran expertise, sharing office space, and support from a fellow PhD in arms. Last, but not least, I wish to warmly thank **Leena Subramanian** for making sure this thesis would be submitted on time, not a single day later.

I would like to thank my parents for their love and support, and my long-standing life partner, **Magdalena**, for her encouragement and being my principal intellectual stimulus.

All the data analyses were performed in, and figures were obtained from Origin® from OriginLab Corporation. The simulation of semiconductor laser dynamics was written and compiled in Compaq Visual Fortran compiler (obsoleted; contemporarily know as Intel® Visual Fortran Compiler). The public domain Fast-Fourier Transform code was obtained from *Numerical Recipes* (1986). All the vector figures were prepared in Inkscape. The thesis was written in WinEdt® and typeset in MiKTEX. Lastly, I would like to avail myself of the opportunity and thank Prof. **Donald E. Knuth** for developing TEX, and **Leslie Lamport** for LATEX.

List of Figures

List of Tables

Contents

Glossary

BS	Beam Splitter
CC	Correlation Coefficient
CCC	Cross-Correlation Coefficient
CMA	Chaos Masking
CMO	Chaos Modulation
CSK	Chaos Shift Keying
D	Detector
ECM	External-Cavity Mirror
ECSLD	External-Cavity Semiconductor Laser Diode
HWP	Half-Wave Plate
ISO	Optical Isolator
LEF	Linewidth Enhancement Factor
LFF	Low-Frequency Fluctuations
ML	Master Laser
NDF	Natural-Density Filter
PBS	Polarising Beam-Splitter
SL	Slave Laser
SLD	Semiconductor Laser Diode
STF	Spectral Transfer Function
XCM	External-Cavity Mode

Chapter 1

Introduction

Ancient Greece and shaved heads

Humankind has always craved for and sought a secure means of delivering a message from the sender to the intended recipient. One of the most illustrious examples of how people went about effecting confidentiality of communication dates back to Ancient Greece, where the head of a messenger would be shaved, a secret message would be written on the scalp, followed by a prolonged period necessary for the hair to grow back, to conceal the message. When it did, the messenger would be sent on the way. Finally, upon arriving, he would tell the intended recipient to shave his head again thereby disclosing the message [1]. Obviously, this method of communication could not be exploited for delivery of urgent messages; moreover, the frequency of message exchange was restrained by the number of servants. On the other hand, those times could easily accommodate certain delay in transmission of information.

Definition

According to Oxford English Dictionary, 'cryptography' means:

> A secret manner of writing, either by arbitrary characters, by using letters or characters in other than their ordinary sense, or by other methods intelligible only

1

to those possessing the key. [...]

The definition of 'cryptanalysis', also taken from Oxford English Dictionary, states:

The art of deciphering a cryptogram or cryptograms by analysis.

Combining these two fields is 'cryptology', defined as [2, p. xvi]:

[...] the science that embraces cryptography and cryptanalysis, but the term 'cryptology' sometimes loosely designates the entire dual field of both rendering signals secure and extracting information from them.

Lastly, according to [3, p. 4] 'steganography' means:

[...] the art of concealed communication. The very existence of a message is secret.

1.1 Brief history of cryptography

Ancient Greek scytale

The first example of applied cryptography dates back to Ancient Greece, where an artefact in the form of a wooden rod was used [4]. The rod itself would have its parts cleaved off so as to form a polygon in cross-section. A piece of cloth with seemingly incomprehensible message would be wrapped around it in a form of a spiral revealing thereby the hidden message on one of the sides. Only rods of equal number of sides would allow for communication between the sender and recipient.

Caesar's code

The second example comes from the Roman Empire and is famed by Julius Caesar who applied it extensively. Caesar's Cipher belongs to a greater family of monoalphabetic substitution ciphers where the coding alphabet is shifted by an arbitrary, yet agreed upon by both parties, number. In this very case, the cipher is associated with a shift of three letters, as illustrated below:

Plaintext alphabet:

a b c d e f g h i j k l m n o p q r s t u v w x y z

Ciphertext alphabet:

D E F G H I J K L M N O P Q R S T U V W X Y Z A B C

Vigenère cipher

The greatest breakthrough of the Renaissance era within the context of cryptography is to be attributed to the development of the concept of a polyalphabetic cipher whereby every letter is enciphered in a different alphabet. In principle, the process is equivalent to applying a different Caesar's cipher on every letter. Although the cipher is generally misattributed to French diplomat, Blaise de Vigenère, its concept was originally described in 1466 by Florentine polymath Leon Battista Alberti in his essay on cryptography [5] (for a contemporary reprint, see [6]). Unfortunately, he failed to communicate his idea to the wider public. In 1549 Vigenère synthesised [7] a powerful polyalphabetic cipher that he called *Le Chiffre Indéchiffrable* (*The Indecipherable Cipher*); it would remain unbreakable for three centuries.

Auguste Kerckhoffs' Principle

In 1883 Dutch linguist Auguste Kerckhoffs von Nieuwenhof wrote a famous two-part article [8, 9] from which the following quote is taken (trans.):

> A cryptosystem should be secure even if everything about the system, except the key, is public knowledge.

This sentence would later become a fundamental premise in modern cryptology and it formed the corner stone of a new era—an era where the details of algorithms and implementations were to be discussed openly, and where the previously prevailing notion of 'security-by-obscurity' was shown to be based on a flawed assumption.

One-Time Pad

In 1917 Gilbert Vernam, then employee of AT&T, introduced the concept of a secret key's length being as long as the message itself, which results in the number of deciphered, equally plausible, versions increasing *ad infinitum*. Furthermore, there is no telling which of the possible versions is the true message. A year later, Major Joseph Mauborgne, then head of cryptographic research of US Army, developed the concept of a random key—previously keys almost exclusively consisted of common words or phrases, which made cryptanalysis easier. Combine these two concepts and one arrives at the Holy Grail of cryptography; as long as *all* the conditions are satisfied, *i.e.*:

- a message is encrypted with a key of the same length (or greater);

- that key is random;

- that key is *never* re-used,

then One-Time Pad offers *perfect* security. This fact was mathematically proven by Shannon in his seminal paper [10]. In his previous publication [11], he defined the grounds for a new scientific discipline—Information Theory.

However, insurmountable obstacles are inherently associated with the use of this scheme. They are mostly concerned with secure key distribution, which becomes more complex with a factorial of the number of participants. Another reason for this is the generation of random numbers of adequate quality and quantity. Hence the famous quote[1]:

> The generation of random numbers is too important to be left to chance.

Currently, this scheme is commonly used by bodies that require such confidentiality on a fundamental level and at the same time can afford the expense inextricably associated with using it. One of the examples being the Moscow–Washington hotline between the Presidents of Russia and the United States [2].

---

[1]Robert R. Coveyou used it as a title for one of his articles; after [12].

Enigma

Conquering the Enigma—the most symbolic cryptosystem in the history—is to be ascribed to a number of factors: initial disclosure of the mechanical and electrical intricacies of the device to the French Resistance [1], development of the first decryption technique by the three Polish mathematicians [13], as well as, further extension of this work by Alan Turing [14, 15].

Remarkably perhaps, the actual code was not broken *per se*. What allowed the Allies to read encrypted messages was mechanised brute-force exhaustion of key-space compounded with exploitation of a certain mannerism employed by German telegraphers when sending daily weather reports. The story of Enigma marks the end of time when linguists, crossword and riddle enthusiasts, polyglots, *etc.* were employed to break enciphered messages. From this point onwards, it became the game of mathematicians and computer scientists, and the individual approach was replaced by a mechanised, conveyor-belt-like process.

Diffie–Hellman and RSA

Another breakthrough came to be in 1976, when the seemingly insolvable, ever present dilemma of secure key exchange via insecure channel (without the key becoming compromised) was solved by the Diffie–Hellman–Merkle trio [16]. In their scheme, they exploited properties of modular algebra to guarantee confidentiality in what is now called the Public Key Exchange. Later, in 1978, the notion of an asymmetric cipher was developed by another trio: Rivest–Shamir–Adleman [17]. Until that point in time all the processes of encryption and decryption had dealt with a symmetric key, *i.e.* one which is used in the same form for both processes. The idea behind the RSA algorithm relied on the assumption that is it easy to multiply two large primes (which *de facto* constitute the secret key), but it would take incomparably long to factor the product.

Quantum Key Distribution (QKD)

The concept of employment of quantum states was conceived of in 1960s when Stephen Wiesner developed the idea of banknotes secured against forgery with quantum information [18]. He called it *quantum money*. Unfortunately, his idea was ahead of the time and therefore ignored. Approximately twenty years later, his idea served as inspiration for Bennett and Brassard, who invented QKD [19].

What is unique in this concept is its *modus operandi*, which exploits Heisenberg's uncertainty principle. An eavesdropper in an attempt to intercept the photons between the legitimate parties would inevitably perturb the quantum states of those photons thereby immediately signalling to the legitimate parties that they are being eavesdropped on. Unless a breakthrough in physics occurs, one that would allow probing a photon's quantum states without affecting them (*i.e.* in effect circumventing Heisenberg's uncertainty principle), Quantum Cryptography will remain secure on the grounds of fundamental laws of physics. Having said that, experimental set-ups have been presented to be capable of intercepting secret keys [20]. It needs to be stressed, however, that these set-ups exploit *hardware* imperfection [21–23].

Quantum Computers

Quantum computer is a computational device [24–27] that exploits quantum mechanical properties of atoms to perform calculations. The main difference in comparison to a classical computer is reliance on quantum properties like entanglement and superposition. Classical computer of four bits is a deterministic machine that at any time can be found in any *one* of 16 (2^4) states with probability of one. Quantum computer of four qubits (quantum bits) on the other hand can be found in *all* of the 16 states with a non-zero probability.

A physical device employing five qubits built on a silicon chip has been presented to successfully factor number 15 (into 3 and 5) [28]. Although the device is designed

6

specifically to factor that number and it certainly is a trivial case of factorisation, it nonetheless serves as a proof-of-concept, as well as, a promising platform for future scaling up to tackle real-life RSA-grade numbers. For previous attempts at constructing a quantum computer, refer to [29–31]. The first *programmable* quantum computer, *i.e.* not limited to one specific operation has, too, been presented [32]. It consisted of two qubits and was tested with 160 different operations.

The significance of quantum computers can be most readily expressed in a prospect of all the commonly used cryptographic schemes[2] being rendered invalid should quantum computers be made to employ Shor's algorithm [33]. It is no longer a question of whether the concept will materialise, but rather when. Another proven application is database search that relies on Grover's algorithm [34]. A fuller discussion of post-quantum landscape of the world can be found in [35–39].

Mary Queen of Scots and Zimmermann Telegram

Often times, lives of people depended on confidentiality of correspondence. One stark example is the story of Mary Queen of Scots who was accused of and convicted of conspiracy against Queen Elizabeth, and consequently beheaded on 8 February 1587. It would not have taken place had Queen Elizabeth's Secretary of State, Sir Francis Walsingham, not broken Queen Mary's intricate, and then state-of-the-art code [1].

Another illustrious example is the infamous Zimmermann Telegram. Germany's Foreign Minister Arthur Zimmermann while trying not to involve America in the Great War sent the telegram to the German Embassy in Mexico informing the German ambassador to encourage the Mexican president to attack the United States. His telegram was intercepted by the British on 17 January 1917, deciphered, and subsequently, although not immediately, handed over to the Americans thereby giving them a proof of German intentions. The note was presented to the President Woodrow Wilson and

---

[2]Amongst others, RSA and Diffie–Hellman, as well as, all the other schemes dependent upon them.

America did join the Great War [1]. In contrast to Mary Queen of Scots, Arthur Zimmermann's life was spared.

Conclusion

In the modern era, the much-coveted concept of *absolute* security has been disavowed on the grounds of One-Time Pad versus feasibility in favour of and replaced by *sufficient* security in all practical applications. This concept relies on the premise that every cryptogram may be eventually broken, however, before it does, a certain amount of time and resources would have to be invested in doing so. These days a message is considered secure if it would require thousands of years of the total computational power on Earth to be employed in breaking that message. Such an approach to message security relies on complexity and the impermeability of the encryption algorithm in conjunction with immense (astronomical to say) expense an opponent would have to face in pursuit of that message. In the nomenclature of cryptology, security of every cryptosystem relies on both, the complexity[3] of an algorithm (or mechanical construction of the encoder), and the key which is intended to remain secret.

The history of cryptography is nothing more than an ongoing struggle between those who devise ciphers and those who seek to break them. If there is but one lesson to be learned from that process, it is that what often seems impermeable and impervious to cryptanalysis and virtually unbreakable, ends up broken provided one possesses enough resources and motivation at his/her disposal.

---

[3]Specifically complexity—*not* obscurity.

1.2 Brief history of steganography

Ancient Greece

The practice of secret writing has always accompanied humankind either in form of primitive scrambled alphabets (as mentioned in the previous section) or as objects of everyday use. In addition to head shaving mentioned on page 1, Herodotus wrote in *The Histories* about Demaratus who, in 480 BC, had scraped wax off a wooden panel, written on it, then covered it again in wax and sent a slave messenger with it to warn the Greeks about imminent Persian invasion led by Xerxes, the king of Persia [4, 40].

Ancient China

Ingenious in its simplicity is an example coming from Ancient China, where messages would be written on pieces of silk, then put in wax, molded so as to resemble a small ball. Finally, a messenger would swallow it, travel to the intended recipient and excrete it [1]. This method has survived, with small modifications, to the contemporary times and is most commonly used to smuggle illicit substances across borders.

Another example from the Middle Kingdom is a scheme whereby both parties—sender and recipient—would be equipped in copies of the same paper mask with holes cut in random places. The sender would place the mask over a sheet of paper and write the secret message into those spots. Then, the mask would be removed and the remaining places on the sheet of paper would be filled with arbitrary content. The recipient would be able to read the secret message instantaneously by simply placing the mask over the sheet of that paper. This protocol was reinvented by Italian mathematician Cardan[4] in 16th century, and reinvented again by a British bank in 1992 [41].

---

[4]This is also the reason why this particular method of communication is now known as *Cardan grille.*

Invisible ink

Pliny the Elder, in his *Naturalis Historiæ*, wrote how the sap of a certain plant could be used as invisible ink. Later, heating the dried liquid would result in charring thereby revealing the message [42] (for a contemporary reprint, see [43]).

Giovanni Porta wrote in 16th century about using a mixture of alum and vinegar to write messages on the shells of hardboiled eggs, which would pervade the shell and leave the marking on the egg albumen. Therefore, for anybody to read it, the shell would have to be broken [4].

With time, invisible ink technology matured as more sophisticated substances were discovered—ones that would react to specific chemical compounds and developing procedures. Nevertheless, the advent of modern chemistry (specifically, the invention of universal developers) rendered invisible ink of little use. In addition, progress made in paper industry resulted in procedures of prefabricating sheets of paper that would reveal attempts at using invisible inks [44].

Microdots

Microfilm photography, as a concept, emerged in 1850s [45]. In *Encyclopædia Brittanica* under the headword 'microscope' Sir David Brewster suggested using this technique in order to convey a hidden message. In practice, microfilms were used for the first time in 1870–71 during Franco–Prussian War, when pigeons were used to carry microfilm messages [46, 47]. Another war, Russo–Japanese War of 1905, saw employment of hiding techniques of microfilms on or within human body [45]. Microfilms were finally subjected to further optical reduction thereby giving birth to microdot technique. German spies successfully employed it during WWI, and mastered it during WWII [48, 49].

Digital Era

In the contemporary era, the term 'steganography' has come to be understood in terms of hiding data in means of electronic communication, such as lossy audio files [3, 50–52], video files [50, 53], lossy image files [54, 55], watermarking web sites [56] or even millisecond-scale differences in transmission rate of data packets between computers [40, 57–60].

1.3 Brief history of chaos communications

Pendulum synchronisation

Although more renowned for his wave theory of light (*Traité de la lumière*, 1690), Christiaan Huygens played a fundamental role in inventing pendulum clocks and synchronising them.

When investigating two pendulums suspended under the same beam, he came across 'imperceptible movements' of that beam which, as he deducted, gave rise to anti-phase synchronisation of the pendulums. What is more, irrespective of initial conditions, even when perturbed, the pendulums in his experiment would return to anti-phase oscillation. In a letter sent to the Royal Society in 1665, he then wrote of:

> [...] an odd kind of sympathy perceived by him in these watches [two pendulum clocks] suspended by the side of each other.

In 1673 Huygens presented a mathematical analysis of pendulum motion in his book, *Horologium Oscillatorium sive de motu pendulorum*. What he did not know, however, was that the case of anti-phase synchronisation he had discovered is, in fact, only a special case in a broader and general set of pendulum motion. Huygens' observation was further explored in [61–63]. Finally, a detailed analysis of a two-pendulum system was presented in [64].

Scientific determinism

The notion of absolute or 'Laplacean determinism' was defined by Pierre Simon de Laplace in 1814 in his book *Essai philosophique sur les probabilités* (trans.):

> We must consider the present state of the Universe as the effect of its past state and the cause of its future state. An intelligence that would know all forces of nature and the respective situation of all its elements, if furthermore it was large enough to be able to analyze all these data, would embrace in the same expression the motions of the largest bodies of Universe as well as those of the slightest atom: nothing would be uncertain for this intelligence, all future and all past would be as known as present.

which, in other words, translated into a belief that every force, every dimension and every quantity could be measured with absolute certainty, and all these values would then fall perfectly in place with the equations describing every aspect of reality. The only reason experimental observations did not quite fit this belief was easily explained on the grounds of imperfection of measuring apparatus.

This standpoint was then reinforced by Sir Isaac Newton's treatise on mechanics (*Philosophiæ Naturalis Principia Mathematica*, 1687), which triggered the first great unification in physics, and is arguably the single most influential piece of writing in physics[5], that also encapsulated the beauty and *deterministic* nature of motion and acceleration.

Despite the fact that Sir Isaac wrote more works on occult and Biblical hermeneutics than hard science, he is most commonly known for discovering the law of universal gravitation, which he also warned against using to perceive the entire Universe as clockwork [65]:

> Gravity explains the motions of the planets, but it cannot explain who set the planets in motion. God governs all things and knows all that is or can be done.

---

[5]It is nonetheless closely followed by Albert Einstein's *Zur Elektrodynamik bewegter Körper* (1905) and James Clerk Maxwell's *Treatise on Electricity and Magnetism* (1873).

Nonetheless, it needs to be pointed out that Newton's laws of mechanics were and still are of great importance. Once published, they allowed for solving numerous previously unsolvable problems.

Poincaré and chaos theory

What started as an attempt at deriving an analytical solution to the three-body problem[6] during mathematical contest held in the name of King Oscar II of Sweden, ended with a revelation. Even though Henri Poincaré did not provide a full solution for the problem, he was chosen as the winner of the competition and his solution was officially published, despite the fact it then contained an important error. It was only after the contest when Poincaré realised the deterministic, yet *unpredictable* nature of the error—nature which he promptly excluded during the contest. For this discovery, he is quite often referred to as 'the Father of chaos'. He wrote in 1908 in his *Science et methodé* (trans.):

> If we knew exactly the laws of nature and the situation of the universe at the initial moment, we could predict exactly the situation of that same universe at a succeeding moment. But even if it were the case that the natural laws had no longer any secret for us, we could still only know the initial conditions approximately. If that enabled us to predict the succeeding situation with the same approximation, that is all we require, and we should say that the phenomenon had been predicted, that it is governed by laws. But it is not always so; it may happen that small differences in the initial conditions produce very great ones in the final phenomena. A small error in the former will produce an enormous error in the latter. Prediction becomes impossible, and we have the fortuitous phenomenon.

Last but not least, a solution to the elusive three-body problem was finally provided by Sundman in 1913 in [66], whereas a generalised solution for n-body problem (where $n > 3$) was provided by Wang in 1990 in [67].

---

[6]In the traditional sense, to mechanics of a system composed of three bodies affecting one another, for example a celestial set-up composed of the central star and two orbiting planets.

Heisenberg's uncertainty principle

Werner Heisenberg's uncertainty principle [68] heralded an inherent nature—a property inextricable from the system, often interpreted as (most notably by Niels Bohr and Heisenberg himself) a physical limit independent of experimental set-up on the precision with which a pair of certain physical variables may be measured, in this case position in space of a particle and its velocity:

$$\Delta x \Delta p_x \gtrsim h \tag{1.1}$$

where Δx corresponds to uncertainty of measurement of position in x-dimension, whereas Δp_x stands for uncertainty of measurement of momentum in x-dimension. However, it is the form as devised by Kennard in [69] that is the most prevailing one today:

$$\sigma_x \sigma_p \geq \frac{\hbar}{2} \tag{1.2}$$

where σ_x and σ_p stand for *standard deviations* of position and momentum, respectively.

An equivalent form of the Principle is expressed in energy–time coordinates, rather than position-momentum coordinates:

$$\Delta E \Delta t \gtrapprox \frac{\hbar}{2} \tag{1.3}$$

where ΔE corresponds to uncertainty of measurement of energy, and Δt stands for the time during which the system exists unperturbed.

Einstein's theory of relativity

Probably the largest conceptual change came to be in 1905, also known as the *Annus Mirabilis*, when Einstein published four revolutionary papers which have since completely changed the landscape of physics. What began as a *Gedankenexperiment* as to how

it might seem to travel at the speed of light ended with formulation and further announcement of the Special theory of relativity [70] in 1905, followed by the General theory of relativity [71] in 1917. This was the first time Newton's laws of mechanics were subjected to a thorough analysis.

With the onset of theory of relativity compounded with the uncertainty principle, the notion of absolute determinism lost its significance. Inadvertently, however, relativity began to be equated with philosophical and moral relativism, much to the dismay of Einstein.

1.4 Chaos communications

The origins of the concept of harnessing chaos to the purposes of communications can be traced back to the paper [72, 73] published by Yamada and Fujisaka in 1983 and 1984, which was then followed by work [74] done by Afraimovich et al. in 1986. Finally, in 1990, Pecora and Carroll published their seminal paper outlining a proof-of-concept [75]; it was they who speculated on the possible applications. Their vision embodied a set of electronic circuits rather than optic or optoelectronic components. Nonetheless, the concept was soon expanded by other research groups to include laser technology. An overview of influence of chaos theory on diverse areas of human activity can be found in [76–82].

All the schemes of chaos communications are dependent upon the underlying assumption that a secret message may be securely hidden in high-amplitude time-domain fluctuations of the carrier signal in the transmitting laser [83]. Legitimate reception of such a hidden transmission relies on a two-stage process—first, the incoming optical wave is split and half of it is sent to a detector; second, the other half is sent to the receiving laser (which is normally required to be as physically similar to the transmitter as it is possible). This laser would first be made synchronous with the transmitter

through the process of optical injection and subsequent alignment of receiver's external cavity [84], as well as, optimisation of other parameters so as to mimic the dynamics of the transmitter [85]. The quality of such synchronicity would be effected via monitoring the correlation coefficient between the incoming wave from the transmitter and the output wave of the receiver. Through the process of Chaos Pass Filtering [86–92], the hidden message would be attenuated in the receiver. Finally, the receiver's output waveform would be subtracted from the incoming waveform. The result would constitute the hidden message. The factual physical phenomena governing synchronisation of two chaotic systems are still not entirely understood.

The first experimental proof of chaos in Nd:YAG lasers was effected in bidirectional coupling configuration [93]. The reason for the presence of mirrors in optical pathways of both lasers is discussed in section 2.3.2. The configuration employed in that study is presented, along with the other two common set-ups, in figure 1.1. For a discussion on performance of open-loop[7] versus closed-loop[8] configuration, see [94–99]. CO_2 lasers also experience chaotic phenomena when subjected to appropriate conditions. The first experimental and theoretical proof of such nonlinear dynamics was shown in [100]; the configuration employed, amongst other elements, a saturable absorber inside the cavity. The first experimental proof of chaos in erbium-doped fibre lasers was given in [101]; this scheme was later analysed and broken [102]. It was followed by a series of publications related to erbium-doped fibre ring lasers [103–105]. Additionally, numerical analysis of high-dimensional synchronisation in coupled ring cavity was presented in [106].

Fine-tuning chaos properties by carefully choosing values of parameters to obtain chaotic attractors of desired properties was demonstrated in [107–110]. To date, gigahertz-scale chaos synchronisation [86, 94, 111], as well as, synchronisation over a long fibre [111, 112] have been presented. Influence of parameter mismatch on the quality of synchronisation was investigated in [111]. A brief review and unified frame-

---

[7]In such a configuration the SL is devoid of its ECM.
[8]Here, the ML and the SL are both used with an ECM.

work for treating various synchronisation schemes is provided in [113]. A thorough analysis of chaos-based communication systems in terms of applicability to real-life telecommunications channels and hardware was performed in [114–117].

Over the years, a few different synchronisation schemes have been developed, however, scholars have concentrated predominantly on the following three schemes:

- Chaos Masking (CMA);

- Chaos Modulation (CMO);

- Chaos Shift Keying (CSK) / Chaos Switching.

Chaos Masking

CMA concept was first proposed in [118, 119] and it relied on application of simple chaotic attractors [120]. In this scheme, secret message is externally added to the chaotic high-amplitude oscillation. The combined message is transmitted to the receiver, which through the process of Chaos-Pass Filtering attenuates the message. This attenuated trace is then subtracted from the incoming optical trace.

The concept of a return map was proposed to break it [121]. In response, an approach employing hyperchaotic attractor was developed to improve masking capabilities owing to more complex dynamics [122]. It was again countered by development of nonlinear dynamic forecasting [123, 124]. Additionally, low- and high-dimensional CMA was shown to be broken with use of wavelet transform and without resorting to chaos synchronisation at all [125]. Statistical analysis also proved CMA vulnerable [126, 127]. A high-pass filter was also successfully used without any knowledge of the chaotic transmitter [128].
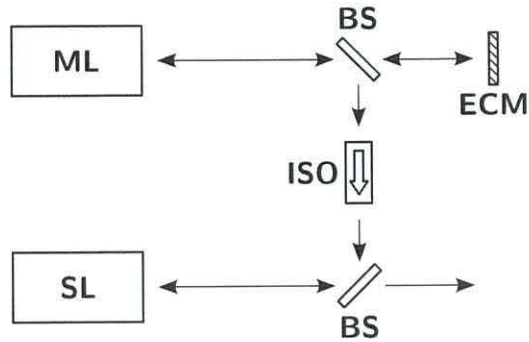
(a) Schematics of a unidirectional open-loop set-up. ML is rendered chaotic owing to its ECM; its optical field is unidirectionally injected into a solitary SL.
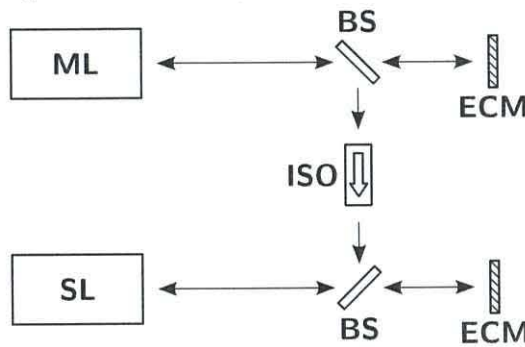
(b) Schematics of a unidirectional closed-loop set-up. ML and SL are both rendered chaotic owing to their ECMs. ML's optical field is unidirectionally injected into SL.
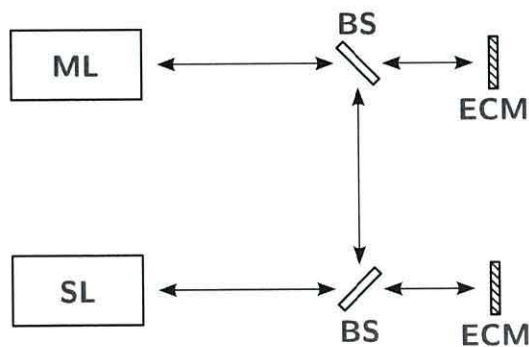
(c) Schematics of a bidirectional closed-loop set-up. ML and SL are both rendered chaotic owing to their ECMs. ML's optical field is injected into SL, and vice-versa.

Figure 1.1: Schematics of the three main injection-locking set-ups – BS (beam splitter), ECM (external-cavity mirror), ISO (optical isolator).

Chaos Modulation

CMO concept was first proposed in [129], and expanded in [119, 120, 122, 130–132]. In this scheme, secret message is not added to, but rather modulates the chaotic carrier oscillation. This compounded message is transmitted to the receiver. The process of message extraction is analogous to that in the CMA scheme.

CMO was first broken by application of return maps [121, 133]. In order to render return maps ineffective, diffusion of modulated parameters was proposed in [134]. Later, three research groups independently proved diffusion ineffective [135–137]. In [138, 139] it is found that even though CMO is more secure than CMA (in the CMA scheme the hidden message distorts the phase-space trajectory, while in CMO the hidden message becomes an integral part of a different trajectory), it is nevertheless still vulnerable.

A concept of zero-crossing detection was developed to unravel the modulation function [135], however, in order to hinder that particular alley of cryptanalysis, the authors suggested removing the relationship between the modulating function and the zero-crossing points. Nonetheless, it still was proven vulnerable in [140]. Again, a high-pass filter was successfully used without any knowledge of the chaotic transmitter [128]. Naïve eavesdropping was shown to be ineffective against CMO in [141], although the authors did not even try to unravel the hidden message—no tuning of external cavity resonance, or temperature, or drive current, or injection strength.

Chaos Shift Keying / Chaos Switching

CSK concept was first proposed in [142, 143]. In this scheme, secret message is used to switch between two chaotic attractors (which can be effected with either one or two master lasers). The process of message extraction is realised through monitoring synchronisation errors (which, again, can be effected with either one or two slave lasers).

CSK has been broken by subsequent application of a number of analytical approaches, such as:

- short time zero crossing rate [144];

- generalised synchronisation [145];

- spectrum analysis [146];

- neural networks [147];

- adaptive key identification [148];

- periodic orbit theory [149].

It was shown that use of multiple attractors improves performance of chaos communications system in presence of noise by a few orders of magnitude [150]. It was based on 'adding two chaotic signals to remove dc component' [151]. It was also based on linear combination of drive variables [152], which improves the quality of synchronisation when parameter mismatch is taken into account [153]. In response, high-dimensional CSK was broken in [145, 146]. CSK was also presented in an on/off configuration with a single receiver [154].

A comparison of a few CSK schemes is provided in [155]. It contains simulation results, as well as, a brief discussion regarding optimisation and sub-optimisation of transmitters and receivers. Although not a word on security aspects. It was shown in [156] that all three schemes (CMA [118, 119], CSK [142] and CMO [157]), when based on Lorenz attractor are susceptible to cryptanalysis. Moreover, hyperchaotic systems were also successfully compromised with various attack vectors [143, 152, 158–162]. Additional methods of breaking chaos communication schemes were referenced:

- based on auto-synchronisation [163, 164];

- based on algorithms for fitting differential equations to time series [162, 165, 166].

Apart from the three mainstays of chaos communications, three other means of

masked transmission are named as follows: key stream chaos [167–169], phase synchronisation [170, 171], and intermittent chaos [123, 167, 172–175].

Transmission properties of chaos communications

Chaos theory, apart from application in secret communications, together with spread-spectrum communications [176, 177, and references therein] present themselves with a range of certain advantages over narrowband transmission schemes [114], such as:

- higher resistance to multipath destructive interference and resulting attenuation;

- narrowband transmission cause higher interference with other narrowband transmissions;

- lower probability of interception due to spread nature of transmission.

Finally, apart from devising new communication schemes, followed closely by disclosing their vulnerabilities, scholars have also been involved in research aimed at exploiting the phenomenon of mode-locking for the purpose of transmitting data:

- semiconductor lasers [178];

- self-pulsating lasers [179–181];

- external-cavity lasers [182, 183];

- HeNe laser [184];

- argon and dye lasers [185, 186].

This area of scientific research, however, lies outside of the scope of this thesis.

Chaos communications versus cryptography and steganography

Steganography is the art and science of writing hidden messages in such a way that no one apart from the sender and intended recipient even realises there *is* a hidden

message. By contrast, cryptography obscures the meaning of a message, but it does not conceal the fact that there *is* a message [3, 40, 187].

In comparison, chaos communications conforms neither to cryptography, nor steganography. The main difference between a cryptographic system and communications based on chaos synchronisation are as follows:

- cryptosystems are based on a concept of a secret key (either symmetric or asymmetric) to encrypt and decrypt sensitive data, however, such a concept has neither a natural nor obvious adequate form in chaos communications;

- in spite of general recognition of Kerckhoffs' principle, many authors of publications claim security of their chaos communications systems on the basis of obscurity of their systems' parameters (which are either fixed or not feasibly changeable, which in turn defies argument that those parameters could serve as an actual secret key).

The principal common factor chaos communications shares with cryptography is such that all the parties (both, legitimate and eavesdroppers) realise where a communications channel is and that real data is going to be sent through it.

When it comes to commonality with steganography, chaos communications shares with it the concept of threshold beyond which data can be retrieved for certain modulation formats.

Concluding remarks

Most of the proposals pertaining to broadly understood chaos communications are set forth by either engineers or physicists, rather than mathematicians experienced in the intricacies of modern cryptosystems. Few of the proposed schemes underwent any form of critical analysis from a body of professional cryptanalysts at the time of their publication. Instead, security of these schemes was often proclaimed by the respective authors on the grounds of *human-eye* test, with the most convincing proof (in the

authors' minds) being lack of visible perturbations in the graphs of time-domain and frequency components.

The first such analyses to come from scientific community were focused on very fundamental concepts rather than full-fledged communication systems. Nevertheless, they shed light on the otherwise *terra incognita*. Other authors soon followed and disclosed numerous flaws in those schemes. To cite [171]:

> [...] some of them [are] fundamentally flawed by a lack of robustness and security.

To make matters worse (from the point of view of security), it is very difficult to discuss chaos communications system's security, as there is no *natural* secret key involved. Arguably, one could postulate that a certain transformation function (*e.g.* a polynomial) could serve the role. However, as it was shown in [140], an iterative approach based on minimisation of synchronisation error via local minima is sufficient to establish certain characteristic values of the system, which is being eavesdropped on.

Chaos as a concept is most concisely described as being extremely sensitive to the smallest of variations, discrepancies in values of initial conditions, *etc.* This very fact is very often used as an explanation as to why it could be difficult to eavesdrop on chaos communications system. As the review above has shown, this assumption is very often proven groundless. However, on the other side of the spectrum lies an example of a system, which is *too robust*—so robust, that eavesdropping on it can be effected with little effort [188].

Those publications that were written from a cryptanalysis' point of view tended to portray the potential security of chaos communications scheme in grim colours. Some papers [189, 190] even provided the community with step-by-step proof-of-concepts on breaking or circumventing the alleged security.

This thesis will not argue for or against a particular communications scheme. Its aim is not to evaluate those schemes, expose weaknesses and propose new, improved schemes. On the contrary, this thesis deals with dynamical properties of semiconductor lasers

exposed to external feedback. Its conception was strongly motivated by application to chaos communications, however, it revolves almost exclusively around dynamics of locking processes. The fact that aspects of security are mentioned above stems from the author's willingness to present the field and its background in a thorough manner.

The remainder of this thesis will focus on carrier dynamics and synchronisation properties of external-cavity semiconductor lasers.

1.5 Structure of the thesis

A general introduction to the fundamental concepts pertaining to this thesis, such as cryptography and steganography is presented in chapter 1. A historical outline of how these two fields emerged and evolved is also provided. The key notion of chaos communications as a field of scholarly research is presented along with characterisation of the most important subdivisions. Finally, a literature review is also included.

The mathematical and analytical frameworks employed in this thesis, necessary to adequately describe the dynamics and phenomena occurring in semiconductor lasers, are presented in chapter 2. The renowned Lang–Kobayashi model is presented and described along with the methodology adopted to numerically solve its extended version, which takes into account external optical injection. This chapter also covers a brief overview of the history of the development of semiconductor lasers, as well as, description of the five regimes of operation of a semiconductor laser subject to optical feedback.

The experimental methodology is first presented in chapter 3. In the first part of this chapter, the influence of drive current and temperature deviation on chaos synchronisation between two lasers is investigated. This effect is measured by cross-correlation function. In the second part, a trivial sinusoidal message is introduced to the Master laser, thereby employing the Chaos Modulation (CMO) scheme. The effect of various message frequencies and modulation depths on synchronisation quality

is investigated and measured through the correlation coefficient and cross-correlation function.

Following the introduction of the numerical approach to solving the Lang–Kobayashi model in chapter 2, the first numerical results are presented in chapter 4. Simulations were run with random initial conditions and multiple-averaging was performed, while varying various parameters, in order to gain an insight into the details of chaos synchronisation dynamics. The parameters varied were the injection strength and ramping time duration.

An investigation of synchronisation robustness constitutes the core of chapter 5. Numerical simulations were performed with the aim of establishing whether substituting one device for another, non-identical one, would significantly affect the chaos synchronisation process between the two lasers. Two parameters, carrier lifetime and linewidth enhancement factor, were separately investigated.

Chapter 6 deals with two experimentally observed phenomena. The first one being, temporal transients occurring in the Slave laser while subjected to optically chopped injection from Master laser. Perturbations introduced in this way gave rise to bistability. The second part of the chapter is focused on the spectral dynamics of TE and TM polarisations of a semiconductor laser subject to variable optical feedback.

A summary of the main results and observations is outlined, along with suggested future work in chapter 7.

Chapter 2

Semiconductor laser theory

In this chapter, a brief account of the history and development of lasers is provided along with a summary of the main characteristics of SLDs. Concepts crucial to the core of this thesis (such as Lang–Kobayashi model) are outlined and a mathematical framework devised to model the nonlinear dynamics of semiconductor lasers. An account of numerical approach taken to solve the Lang–Kobayashi equations is given in the last section.

2.1   Brief history of lasers

1917 Einstein published his seminal paper [191] titled: *Zur Quantentheorie der Strahlung* (*On the Quantum Theory of Radiation*).

1928 Landenburg experimentally showed [192] stimulated emission and negative absorption (*i.e.* amplification).

1939 Valentin Fabrikant in his PhD thesis predicted the use of the stimulated emission to amplify waves; after [193].

1947 Lamb and Retherford identified [194] and demonstrated [195–198] stimulated

emission in hydrogen spectra.

1950 Kastler proposed a method of optical pumping [199].

1954 Gordon, Zeiger, and Townes built the first microwave amplifier [200], although it was incapable of continuous output [201].

1955 Basov and Prokhorov suggested optical pumping of multilevel system as means of obtaining population inversion [202, 203].

1957 Schawlow and Townes published their groundbreaking theoretical calculations [204] on infrared maser and proposed extending the concept of maser to optical frequencies.

1957 Gordon Gould, while working on his PhD thesis on energy levels of excited thallium, invented a concept of an open resonator, but did not publish it; after [205].

1958 Prokhorov independently proposed an open resonator [206, 207].

1959 Gould coined the term 'laser' [208].

1960 Maiman built the first ruby laser [209], in spite of the fact that Schawlow had declared ruby incapable of inducing and sustaining stimulated emission; the laser, however, was only capable of pulsed output.

1960 Javan, Bennett, and Herriot built the first HeNe laser [210].

1962 Basov and Javan proposed a concept of a semiconductor laser diode. Four research groups independently demonstrated the first GaAs diode [211–214].

1970 Two research groups independently developed heterojunction SLDs: one led by Alferov et al. [215, 216] and the other by Hayashi et al. [217]. For an overview see [218].

1975 van der Ziel et al. built the first quantum-well semiconductor laser [219].

1980 Lang and Kobayashi published their paper [220] on aspects of SLD dynamics subject to external feedback.

1986 Tkach and Chraplyvy published phenomenological demarcation (see section 2.4.2) of boundaries between five regimes of operation of a DFB laser subject to external optical feedback [221]. The experimentally obtained plot is broadly applicable to all semiconductor edge-emitting lasers.

1990 Pecora and Carroll published the first in a series of papers on chaos in electronic circuits [75, 150, 222–225] that triggered off scientific inquiry into chaos in optoelectronic systems.

The above list provides details of the essential developments that have taken place in the realm of semiconductor lasers that pertains to the topic of this thesis. One can find many published materials that cover the history of lasers in great length and detail, such as: [205, 226, 227].

2.2 Characteristics of semiconductor lasers

The main characteristics of edge-emitting semiconductor lasers are listed as follows:

- Physical size ($\approx$ hundreds µm $\times$ ten µm $\times$ tens µm) is most often expressed in micrometres rather than centimetres or metres, which is several orders of magnitude smaller than that of other lasers.

- Amount of noise generated by the device is relatively high, as a result of spontaneous emission, high unit gain and broad amplification spectrum, which in turn is further compounded with interplay between gain and refractive index.

- Excitation of the electrons in the active layer through the direct injection of electrical current rather than by optical pumping (in solid-state lasers) or plasma excitation (in gas lasers).

- Owing to direct injection and invention of heterostructures, the efficiency of conversion of energy is very high (>50%), *ergo* there is no need for a complex cooling system to be installed on the laser itself, instead, a simple Peltier element is put in place; to put it in perspective, other types of lasers usually achieve external efficiencies of mere 1–5%, with the noble exception for CO_2 lasers that achieve level of *ca.* 10%.

- Due to their high unit gain, SLDs are most commonly operated without the need to keep the laser facets' reflectivity close to 100%. Consequently, SLDs are rarely used with ECMs, whereas other lasers (*e.g.* gas lasers, solid-state lasers) are dependent on the ECMs to obtain high values of cavity quality factor. As a result, SLDs display high sensitivity to perturbations coming from external sources.

- SLDs can be driven by direct electrical modulation or via external optical modulation.

- Maximum frequency of electrical modulation reached so far is 40 GHz [228, 229, and references therein]; further increase in modulation frequency requires the use of external modulators due to onset of deleterious relaxation damped oscillation.

- Linewidth enhancement factor (LEF, also known as the α-factor) is considerably higher in SLDs (in the order of 3–7) than in other lasers (where it is close to zero) [230]. LEF manifests itself as a connection between fluctuations in carrier density and gain—fluctuations in phase are translated into fluctuations in amplitude, and vice versa[1]. It remains a trait of semiconductor lasers that with injected carrier density, optical gain and refractive index of the active region are affected [233].

- Lifetime of a device is usually expressed in years (in comparison, that of gas or solid-state lasers is measured in hundreds of hours).

---

[1]Under certain circumstances LEF can also be used to narrow down the linewidth [231, 232].

2.3 Semiconductor laser theory

2.3.1 Maxwell–Bloch model

Before moving on to Lorenz–Haken model and further to the Lang–Kobayashi model, a derivation of semiconductor rate equations will be performed, starting from Maxwell's equations[2] [234–241]. Differential form of these equations (in terms of *free* charge, as opposed to *total*) take the following form:

$$\nabla \times \mathbf{E} = -\frac{\partial \mathbf{B}}{\partial t}, \tag{2.1}$$

$$\nabla \times \mathbf{H} = \mathbf{J}_f + \frac{\partial \mathbf{D}}{\partial t}, \tag{2.2}$$

$$\nabla \cdot \mathbf{D} = \rho_f, \tag{2.3}$$

$$\nabla \cdot \mathbf{B} = 0, \tag{2.4}$$

where $\mathbf{E}$ and $\mathbf{H}$ are the electric and magnetic field vectors, respectively, whereas $\mathbf{J}_f$ is the free current density vector, and ρ_f is the free charge density. The del differential operator ∇ is, in Cartesian coordinate system, defined as a partial derivative:

$$\nabla = \hat{x}\frac{\partial}{\partial x} + \hat{y}\frac{\partial}{\partial y} + \hat{z}\frac{\partial}{\partial z}, \tag{2.5}$$

where $\hat{x}$, $\hat{y}$, and $\hat{z}$ are unit vectors of respective dimensions. The dielectric flux vector $\mathbf{D}$ and the magnetic flux vector $\mathbf{B}$ are defined as:

$$\mathbf{D} = \varepsilon_0 \mathbf{E} + \mathbf{P}, \tag{2.6}$$

$$\mathbf{B} = \mu_0 \mathbf{H} + \mathbf{M}, \tag{2.7}$$

where ε_0 is the permittivity of free space, μ_0 is the permeability of free space, $\mathbf{P}$ is the polarisation vector, and $\mathbf{M}$ is the magnetisation vector.

---

[2]Maxwell's works triggered the second great unification in physics.

30

By taking a curl of the curl equations (2.1) and (2.2) and exploiting vector identity:

$$\nabla \times (\nabla \times \mathbf{E}) = \nabla(\nabla \cdot \mathbf{E}) - \Delta \mathbf{E}, \tag{2.8}$$

where Laplacian Δ is defined as $\Delta = \nabla \cdot \nabla = \nabla^2$, one arrives at a general form of wave equation:

$$\Delta \mathbf{E} - \mu_0 \frac{\partial}{\partial t} \left(\mathbf{J} + \varepsilon_0 \frac{\partial \mathbf{E}}{\partial t} + \frac{\partial \mathbf{P}}{\partial t} \right) = \frac{\partial}{\partial t} \nabla \times \mathbf{M} + \nabla (\nabla \cdot \mathbf{E}), \tag{2.9}$$

or in an alternative form:

$$\left(\Delta - \frac{1}{c^2} \frac{\partial^2}{\partial t^2} \right) \mathbf{E} = \mu_0 \left(\frac{\partial \mathbf{J}}{\partial t} + \frac{\partial^2 \mathbf{P}}{\partial t^2} \right) + \frac{\partial}{\partial t} \nabla \times \mathbf{M} + \nabla (\nabla \cdot \mathbf{E}), \tag{2.10}$$

where speed of light in vacuum c was defined by Maxwell as:

$$c = \frac{1}{\sqrt{\varepsilon_0 \mu_0}}. \tag{2.11}$$

For an homogenous ($\nabla \cdot \mathbf{E} = 0$), non-magnetic ($\mathbf{M} = 0$) medium of a refractive index η devoid of free charge ($\rho_f = 0$) and with no currents due to free charge ($\mathbf{J}_f = 0$), the wave equation (2.10) is simplified to [242–244]:

$$\left(\Delta - \frac{\eta^2}{c^2} \frac{\partial^2}{\partial t^2} \right) \mathbf{E} = \mu_0 \frac{\partial^2}{\partial t^2} \mathbf{P}. \tag{2.12}$$

If one further limits the deliberation to a linearly polarised wave propagating along z-axis, then equation (2.12) becomes:

$$\left(\frac{\partial^2}{\partial z^2} - \frac{\eta^2}{c^2} \frac{\partial^2}{\partial t^2} \right) E(z,t) = \mu_0 \frac{\partial^2}{\partial t^2} P(z,t), \tag{2.13}$$

where electric field E and polarisation P are dependent only on z and t.

Slowly-varying-envelope approximation (SVEA)

Another approximation commonly introduced in the theoretical analyses of SLDs is separating the field into rapidly oscillating plane-wave carrier

$$E(z,t) \quad = \quad A(z,t)e^{i(kz-\omega_0 t)} + c.c., \qquad (2.14)$$

$$P(z,t) \quad = \quad B(z,t)e^{i(kz-\omega_0 t)} + c.c., \qquad (2.15)$$

where $A(z,t)$ and $B(z,t)$ are assumed to vary slowly with the optical frequency. They still depend on both z and t, however their spatio-temporal dependence is lower than that of the exponential constituent. This simplification is known [245–248] as SVEA and has the following properties:

$$k^2 |A(z,t)| \gg k \left| \frac{\partial A(z,t)}{\partial z} \right| \gg \left| \frac{\partial^2 A(z,t)}{\partial z^2} \right|, \qquad (2.16)$$

$$\omega^2 |A(z,t)| \gg \omega \left| \frac{\partial A(z,t)}{\partial t} \right| \gg \left| \frac{\partial^2 A(z,t)}{\partial t^2} \right|, \qquad (2.17)$$

whereby highest-order derivatives are neglected.

Maxwell–Bloch equations

Including equations (2.14) and (2.15) into equation (2.13) leads to the following form:

$$\frac{\partial A}{\partial z} + \frac{\eta}{c} \frac{\partial A}{\partial t} = i \frac{k}{2\varepsilon_0 \eta^2} B, \qquad (2.18)$$

where angular wavenumber k is defined as $k = \eta \frac{\omega_0}{c}$, and ω_0 is the angular oscillation frequency.

Two additional quantities need to be defined—macroscopic equation for the polarisation:

$$\frac{dB}{dt} = -i(\omega_A - \omega_0)B + i \frac{\mu^2}{\hbar^2} W \left[A + A^* e^{-2i(kz-\omega_0 t)} \right], \qquad (2.19)$$

where $\omega_A = \omega_2 - \omega_1$ is the angular frequency of the electromagnetic wave emitted or absorbed in a two-level system; as well as population inversion:

$$\frac{dW}{dt} = \frac{1}{i\hbar}\left[AB^* - ABe^{2i(kz-\omega_0 t)} - c.c.\right].\qquad(2.20)$$

For details of derivation of the above two entities, see [249–251].

Rotating-wave approximation (RWA)

Another simplification [251–254] usually introduced to this deliberation is RWA, whereby high-frequency components $2\omega_0$ are removed from equations (2.19) and (2.20) thereby giving:

$$\frac{dB}{dt} = -i(\omega_A - \omega_0)B + i\frac{\mu^2}{\hbar^2}AW,\qquad(2.21)$$

$$\frac{dW}{dt} = \frac{1}{i\hbar}\left(AB^* - A^*B\right).\qquad(2.22)$$

The final form of the Maxwell–Bloch equations is obtained by combining equations (2.18), (2.21), and (2.22), as well as including phenomenological terms [251], such as pumping and decay on the right hand side of the following set:

$$\frac{\partial A}{\partial z} + \frac{\eta}{c}\frac{\partial A}{\partial t} = i\frac{k}{2\varepsilon_0\eta^2}B - \frac{\eta}{2T_{ph}c}A,\qquad(2.23)$$

$$\frac{\partial B}{\partial t} = -i(\omega_A - \omega_0)B + i\frac{\mu^2}{\hbar^2}AW - \frac{B}{T_2},\qquad(2.24)$$

$$\frac{dW}{dt} = \frac{1}{i\hbar}(AB^* - A^*B) + \frac{W_0 - W}{T_1},\qquad(2.25)$$

where W_0 is the inversion level in the absence of the optical field, T_{ph} is photon lifetime (photon relaxation), T_2 is polarisation (transverse relaxation), and T_1 is population inversion (longitudinal relaxation). Processes such as spontaneous emission and atomic collisions contribute to T_1 and T_2, whereas T_{ph} is dependent on cavity losses.

Langevin noise is often added to those equations to account for and represent spontaneous emission, ever present in lasers. The added term of spontaneous emission lowers the threshold current of otherwise noise-free laser. However, Langevin noise will be omitted since the scientific interest of this thesis lies with deterministic processes rather than stochastic ones, thus it was considered best not to introduce the noise term.

2.3.2 Classification of lasers

In response to the above Maxwell–Bloch equation set, as well as, in an attempt to further simplify the analysis of laser dynamics, a classification was proposed by Arecchi et al. [255], which provided an approximate division into three classes. Lasers fall into those classes depending on the difference in magnitude of the three characteristic timescales:

Class–A when $T_{ph} \gg T_2, T_1$. Rate equations for the polarisation and the population inversion become adiabatically eliminated, thus the only equation describing the laser is the field equation. This class is also the most stable—to become unstable, two or more additional degrees of freedom need to be introduced to the system. Typical representatives include: HeNe, dye, Ar-ion lasers; for almost edible lasers see references [256–258] and [259, p. 70–71].

Class–B when $T_{ph}, T_1 \gg T_2$. Only the rate equation for the polarisation inversion becomes adiabatically eliminated, thus the equations describing the laser are the field and population inversion equations. Even though the electric field is complex, it can be split into amplitude and phase. This class is stable—lasers do not display signs of chaotic oscillation, unless one or more degrees of freedom are introduced to the system. Typical representatives include: SLDs, CO_2, solid-state, fibre lasers. For a detailed stability analysis of Class–B lasers, see [260].

Class–C when all three times are of the same order. No variables are eliminated—they form three equations describing the laser. This class is unstable at pumping rates

higher than second threshold. Typical representatives include: infrared NH_3, NeXe, infrared HeNe.

Classes A and B are intrinsically stable (when operating as solitary lasers), nonetheless, they can display signs of chaotic oscillation provided at least one (Class B) or two (Class A) additional degrees of freedom are supplied. This can be effected through:

- external optical feedback;

- optical injection from another laser [261]:

  - low-frequency moderate injection [262–265];

  - high-frequency strong injection [266–268].

- modulation of accessible laser parameters;

- optoelectronic components inside laser's cavity [269].

2.3.3   Lorenz–Haken model

In 1975 Haken made a comparison between laser dynamics and turbulent Rayleigh–Bénard convective fluid dynamics [270], which had been used by Lorenz in 1963 in his seminal paper on unpredictability of atmospheric dynamics [271]. Lorenz's observation[3] gave rise to a new field of nonlinear dynamics, namely, the chaos theory. He is also credited with coining the term 'the butterfly effect'[4].

Further deliberation involves normalisation of the field, the polarisation and the

---

[3]It largely went unnoticed at the time of publication.

[4]In 1972 Lorenz gave a talk titled *Predictability: Does the Flap of a Butterfly's Wings in Brazil set off a Tornado in Texas?* as part of 139th annual meeting of the American Association for the Advancement of Science in Washington, DC, USA; after [272].

population inversion from equations (2.23), (2.24), and (2.25):

$$\overline{A} = \sqrt{\frac{\varepsilon_0 c \eta}{2}} A, \tag{2.26}$$

$$\overline{B} = \frac{k}{\varepsilon_0 \eta^2} \sqrt{\frac{\varepsilon_0 c \eta}{2}} B, \tag{2.27}$$

$$\overline{W} = \sigma_s W, \tag{2.28}$$

where the transition cross section σ_s is defined as:

$$\sigma_s = \frac{\mu^2 \omega_0 T_2}{2 \varepsilon_0 \hbar c \eta}. \tag{2.29}$$

By combining equations (2.23), (2.24), and (2.25) with equations (2.26), (2.27), and (2.28), as well as, negating $\partial A/\partial z$ as a small mean field propagating along the z-axis, one arrives at:

$$\frac{d\overline{A}}{dt} = i\frac{c}{2\eta}\overline{B} - \frac{1}{2T_{ph}}\overline{A}, \tag{2.30}$$

$$T_2 \frac{d\overline{B}}{dt} = -(1 - i\delta)\overline{B} - i\overline{AW}, \tag{2.31}$$

$$T_1 \frac{d\overline{W}}{dt} = \overline{W}_0 - \overline{W} + \frac{\Im\left[\overline{A}^*\overline{B}\right]}{I_{sat}}, \tag{2.32}$$

where $\delta = (\omega_0 - \omega_A)T_2$ represents the scaled atomic detuning, whereas the saturation intensity I_{sat} is defined as:

$$I_{sat} = \frac{\hbar^2 c \eta \varepsilon_0}{2\mu^2 T_1 T_2}. \tag{2.33}$$

The Lorenz–Haken model has been studied over the years from various angles. For a generalisation of the model, see [273], where two additional parameters were introduced to take into account asymmetric gain profile and inhomogeneous broadening. In [274] the Lorenz–Haken model was extended to include different relaxation rates for two levels.

2.3.4 A model of chaos

The original model formulated and published by Lorenz in [271] was devised to describe atmospheric phenomena through description of convective fluid flow. It consisted of three variables: X, Y, and Z, as well as, three chaos parameters: Σ, R, and β.

$$\frac{dX}{dt} = -\Sigma(X - Y), \tag{2.34}$$

$$\frac{dY}{dt} = RX - Y - XZ, \tag{2.35}$$

$$\frac{dZ}{dt} = -\beta Z + XY. \tag{2.36}$$

Maxwell–Bloch model can be rewritten to show it is identical to the Lorenz–Haken model. In order to do that, time variable t needs to be normalised to $t' = t/T_2$ (for notational simplicity, the prime will be dropped) whereas the variables obtained from equations (2.30), (2.31), and (2.32) need to be defined as:

$$x = \sqrt{\frac{b}{I_{sat}}}\,\overline{A}, \tag{2.37}$$

$$y = i\frac{cT_{ph}}{\eta}\sqrt{\frac{b}{I_{sat}}}\,\overline{B}, \tag{2.38}$$

$$z = \frac{cT_{ph}}{\eta}\left(\overline{W}_0 - \overline{W}\right). \tag{2.39}$$

Using these new variables, one finally arrives at the Lorenz–Haken model:

$$\frac{dx}{dt} = -\sigma(x - y), \tag{2.40}$$

$$\frac{dy}{dt} = -(1 - i\delta)y + (r - z)x, \tag{2.41}$$

$$\frac{dz}{dt} = -bz + \Re\left[x^*y\right], \tag{2.42}$$

where:

$$\sigma = \frac{T_2}{2T_{ph}}, \qquad r = \frac{W_0 cT_{ph}}{\eta}, \qquad b = \frac{T_2}{T_1}.$$

2.3.5 Semiconductor rate-equations

Inasmuch as semiconductor lasers should be modelled as band structure systems, their intra-band relaxation time (which is in the order of 10^{-13} s) is still four orders of magnitude smaller than carrier lifetime (10^{-9} s). As a result of this fact, as well as, reasons mentioned in section 2.3.2, semiconductor lasers can still be effectively approximated with a two-level model. The mathematical approach involving a rate-equation model is based on the following assumptions [275]:

- averaging over number of carriers (which can experience slightly different field intensities);

- all carriers are assumed to be virtually the same.

The change in intensity ΔI (where $I(t) = |E(t)|^2$) of an optical wave travelling through a homogenous medium can be written as:

$$\Delta I = -aI_0\Delta z, \tag{2.43}$$

where I_0 denotes the initial intensity, a denotes medium attenuation, and Δz denotes short distance along the z-axis such that $\Delta z \rightarrow 0$. When integrated, equation (2.43) gives:

$$I(z) = I_0 e^{-az}. \tag{2.44}$$

By inclusion of gain medium, as well as, phase change along the z-axis, one can rewrite equation (2.44) into the following set of equations describing the electric field propagating back and forth in a resonance cavity:

$$E_f(z) = E_{0f}e^{ikz+\frac{1}{2}(g-a)z}, \tag{2.45}$$

$$E_b(z) = E_{0b}e^{ik(l-z)+\frac{1}{2}(g-a)(l-z)}, \tag{2.46}$$
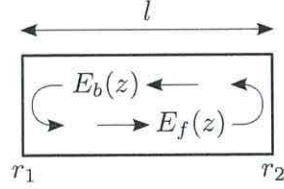
Figure 2.1: Longitudinal field propagation through internal laser cavity – For expressions describing propagation of the electric field in the cavity, see equations (2.45) and (2.46). Boundary conditions are expressed in equations (2.47) and (2.48).

where E_f and E_b are forward and backward propagating complex fields (see figure 2.1), l is the resonator length, g is the laser medium gain, and a is redefined to stand for the total loss in the medium (which is composed of material loss, internal loss, and absorption owing to external pumping [276]). The 1/2 coefficient stems from the fact that both gain and total loss were defined with respect to laser intensity, not amplitude.

By applying boundary conditions of a resonance cavity (where r_1 and r_2 denote amplitude reflectivity, which are related to optical intensity reflectivity such that $r^2 \equiv R$):

$$E_f(0) = r_1 E_b(0), \tag{2.47}$$

$$E_b(l) = r_2 E_f(l), \tag{2.48}$$

to equations (2.45) and (2.46), one arrives at

$$r_1 r_2 e^{2ikl+(g-a)l} = 1, \tag{2.49}$$

which may be further split into two separate—amplitude and phase—constituents:

$$r_1 r_2 e^{(g-a)l} = 1, \tag{2.50}$$

$$e^{2ikl} = 1. \tag{2.51}$$

Amplitude condition

By rewriting equation (2.50), threshold gain—the point where the internal losses a and reflection losses are balanced by gain medium—is henceforth defined as:

$$g_{th} = a + \frac{1}{l} \ln\left(\frac{1}{r_1 r_2}\right).$$ (2.52)

The above equation was derived with the assumption that only stimulated emission contributes to the radiative emission. In practice, however, g_{th} is lower than that predicted above due to the existence of spontaneous emission.

Phase condition

By solving equation (2.51), the phase condition for constructive interference is obtained:

$$kl = m\pi,$$ (2.53)

where wavenumber k is defined as:

$$k = \frac{\omega \eta}{c} = \frac{2\pi \nu \eta}{c},$$ (2.54)

where ν is the optical frequency, and η denotes the refractive index of the active layer. By isolating the frequency term in equation (2.54), the frequency of m-th mode ν_m, as well as, the frequency mode-spacing $\delta \nu$ can thus be obtained as a difference between two consecutive modes (*e.g.* the ν_{m+1} and ν_m):

$$\nu_m = m\frac{c}{2\eta l},$$ (2.55)

$$\delta \nu = \frac{c}{2\eta l}.$$ (2.56)

Single round-trip condition

The refractive index of the active layer η, which is dependent on both carrier density and optical frequency, can be defined as:

$$\eta = \eta_0 + \frac{\partial \eta}{\partial \nu}(\nu - \nu_{th}) + \frac{\partial \eta}{\partial n}(n - n_{th}), \qquad (2.57)$$

where η_0 is the refractive index at the threshold, ν_{th} is the optical frequency at the threshold, n is the carrier density, and n_{th} is carrier density at the threshold. By transforming further equation (2.57) one arrives at the following equality:

$$(\nu - \nu_{th}) = -\frac{\nu_{th}}{\eta_e}\frac{\partial \eta}{\partial n}(n - n_{th}), \qquad (2.58)$$

where η_e is the effective refractive index, which is defined as:

$$\eta_e = \eta + \nu\frac{\partial \eta}{\partial \nu}. \qquad (2.59)$$

The original definition of wavenumber k in equation (2.54) as a function of frequency and refractive index can be further specified as:

$$k = \eta\frac{\omega}{c} = \frac{\omega_{th}}{c}\left[\eta_0 + \frac{\partial \eta}{\partial n}(n - n_{th}) + \frac{\eta_e}{\omega_{th}}(\omega - \omega_{th})\right], \qquad (2.60)$$

where ω_{th} is angular frequency at the threshold, η_0 is the refractive index below the laser oscillation.

Equation (2.49) can be generalised to define the single round-trip gain:

$$G = r_1 r_2 e^{2ikl+(g-a)l}, \qquad (2.61)$$

which, taking into account the expansion in equation (2.60), can be split into two

components—one frequency-independent, and the other frequency-dependent:

$$G = G_1 G_2, \tag{2.62}$$

where

$$G_1 = r_1 r_2 e^{(g-a)l + i\phi_0}, \tag{2.63}$$

$$G_2 = e^{i\frac{2\omega_{th}l}{c}\left[\eta_0 + \frac{\eta_e}{\omega_{th}}(\omega - \omega_{th})\right]}, \tag{2.64}$$

and

$$\phi_0 = \frac{2\omega_{th}l}{c}\frac{\partial \eta}{\partial n}(n - n_{th}). \tag{2.65}$$

G_2 in equation (2.64) can be shown to be equivalent to:

$$G_2 = e^{i\tau_{in}(\omega - \omega_{th})}, \tag{2.66}$$

$$= e^{-i\omega_{th}\tau_{in}} e^{-\tau_{in}\frac{d}{dt}}.$$

The electric field after a single round-trip can be defined as:

$$E_f(t) = GE_f(t). \tag{2.67}$$

Taking advantage of equations (2.62) and (2.66), as well as, substituting into equation (2.67), will lead to:

$$E_f(t) = G_1 G_2 E_f(t), \tag{2.68}$$

$$= G_1 e^{-i\omega_{th}\tau_{in}} e^{-\tau_{in}\frac{d}{dt}} E_f(t).$$

The electric field $E_f(t)$ will now be split into a frequency-independent amplitude, and

a frequency-dependent component, such as:

$$E_f(t) = E_{0f}e^{-i\omega_{th}t},$$ (2.69)

which will allow for the following single round-trip simplification [249]:

$$E_{0f} = G_1 E_{0f}(t - \tau_{in}).$$ (2.70)

If the round-trip time τ_{in} is small enough, then equation (2.70) can be restated to:

$$E(t - \tau_{in}) = E(t) - \tau_{in}\frac{dE(t)}{dt},$$ (2.71)

where τ_{in} stands for round-trip time of light within the internal cavity, which is defined as:

$$\tau_{in} = \frac{2\eta_e l}{c}.$$ (2.72)

By combining equations (2.70) and (2.71) one obtains:

$$\frac{dE(t)}{dt} = \frac{1}{\tau_{in}}\left(1 - \frac{1}{G_1}\right)E(t),$$ (2.73)

where the $1/G_1$ term can be approximated as:

$$\begin{aligned}\frac{1}{G_1} &= e^{-\ln(r_1 r_2) - (g-a)l - i\phi_0} \\ &\approx 1 + \ln\frac{1}{r_1 r_2} - gl + al - i\phi_0.\end{aligned}$$ (2.74)

When one combines equations (2.74) and (2.73), as well as, (2.65) and (2.58), the following equality emerges:

$$\frac{dE(t)}{dt} = \left[-i(\omega_0 - \omega_{th}) + \frac{1}{2}\left(g\frac{c}{\eta_e} - \frac{1}{\tau_{ph}}\right)\right]E(t),$$ (2.75)

where ω_0 is the angular frequency of the laser oscillation, τ_{ph} is photon lifetime. The latter is defined as:

$$\frac{1}{\tau_{ph}} = \frac{c}{\eta_e}\left[a + \frac{1}{l}\ln\left(\frac{1}{r_1 r_2}\right)\right], \tag{2.76}$$

where $c/\eta_e = v_g = 2l/\tau_{in}$ is the group velocity of light in the laser cavity.

Linewidth enhancement factor

Further analysis of semiconductor lasers needs to take into account the effect which the linewidth enhancement factor has on the dynamics. To this end, the susceptibility of lasing medium needs to be considered. The complex susceptibility of the medium below the lasing threshold will be defined as $\chi_0 = \chi_0' + i\chi_0''$, whereas the complex susceptibility of medium owing to laser oscillation will be equal $\chi_l = \chi_l' + i\chi_l''$. The total susceptibility is a function of laser frequency and is also a sum of the aforementioned terms:

$$\begin{aligned}
\chi(\omega) &= \chi_0(\omega) + \chi_l(\omega) \tag{2.77}\\
&= \chi_0' + \chi_l' + i(\chi_0'' + \chi_l'').
\end{aligned}$$

Following certain derivation [249], the real part of susceptibility at lasing oscillation can be redefined to be:

$$\chi_l = 2\eta_b n\left(\frac{\partial\eta}{\partial n} - \frac{i}{2k_0}\frac{\partial g}{\partial n}\right), \tag{2.78}$$

where η_b is the refractive index below threshold.

The macroscopic complex refractive index η_c is given by:

$$\eta_c = \eta - i\eta', \tag{2.79}$$

where η' is the imaginary part of the refractive index and bears the following relation

with gain:

$$\eta^{'} = -\frac{1}{2k_0}g, \tag{2.80}$$

where k_0 is the wavenumber for propagation in vacuum.

Including equation (2.80) into (2.58) allows for the following derivation:

$$
\begin{aligned}
(\omega - \omega_{th}) &= -\frac{\omega_{th}}{\eta_e}\frac{\partial \eta}{\partial n}(n - n_{th}) \\
&= -\frac{\omega_{th}}{\eta_e}\frac{\partial \eta}{\partial \eta^{'}}\frac{\partial \eta^{'}}{\partial n}(n - n_{th}) \\
&= \frac{1}{2}\alpha v_g \frac{\partial g}{\partial n}(n - n_{th}).
\end{aligned}
\tag{2.81}
$$

Finally, the linewidth enhancement factor (also known as the α-factor) is defined as ratio of real and imaginary parts of susceptibility:

$$\alpha = \frac{\Re[\chi]}{\Im[\chi]} = -2\frac{\omega}{c}\frac{\partial \eta/\partial n}{\partial g/\partial n}. \tag{2.82}$$

While equal to almost zero in other types of lasers, in semiconductor laser diodes it amounts to a range between 3 and 7. Despite its name, the actual enhancement (*i.e.* broadening) of bandwidth is proportional to $1 + \alpha^2$ [233].

Gain

Nonlinear gain can be expressed in two forms: either by intrinsic nonlinearities of the gain medium [277–280], or by an effective nonlinearity ascribed to diffusion effects [281]. However, in this thesis, a standard model of linear gain compounded with gain expansion around the threshold will be adopted:

$$g = g_{th} + \frac{\partial g}{\partial n}(n - n_{th}), \tag{2.83}$$

where a redefined g_{th} denotes the gain for the carrier density at transparency n_0:

$$g_{th} = \frac{\partial g}{\partial n}(n_{th} - n_0).$$ (2.84)

This definition of gain threshold still implies balancing of all the losses incurred by the electric field by the gain medium. For a medium to experience lasing oscillation, its gain must exceed that of gain threshold. Well above that threshold, another effect—gain saturation—needs to be taken into account in order to adequately represent experimental results. Hereby, a gain saturation coefficient ε_s is introduced:

$$g = \frac{g_{th}}{1 + \varepsilon_s |E|^2}.$$ (2.85)

Electric field

By combining equations (2.75), (2.81), and (2.83), the following form of the electric field is obtained:

$$\frac{dE(t)}{dt} = \frac{1}{2}(1 - i\alpha)G_n\big[n(t) - n_{th}\big]E(t),$$ (2.86)

where G_n stands for linear gain defined as:

$$G_n = v_g \frac{\partial g}{\partial n}.$$ (2.87)

The photon lifetime can be shown to have the following relationship with the carriers and gain in equation (2.87):

$$v_g \frac{\partial g}{\partial n}(n_{th} - n_0) = \frac{1}{\tau_{ph}}.$$ (2.88)

If one splits the complex field in equation (2.86) into separate, amplitude and phase, components fulfilling the relation $E(t) = E_0(t)e^{-i\varphi(t)}$, the following two equations

emerge:

$$\frac{dE_0(t)}{dt} = \frac{1}{2}G_n\big[n(t) - n_{th}\big]E_0(t), \tag{2.89}$$

$$\frac{d\varphi(t)}{dt} = \frac{1}{2}\alpha G_n\big[n(t) - n_{th}\big]. \tag{2.90}$$

Carrier density is given [245] as:

$$\frac{dn(t)}{dt} = \frac{J}{ed} - \frac{n(t)}{\tau_s} - G_n\big[n(t) - n_0\big]|E|^2 \tag{2.91}$$

where J is the driving current density, d thickness of the active layer, e denotes the elementary charge, and τ_s stands for carrier lifetime. The first term represents current injection, the second—carrier recombination due to spontaneous emission, the third—carrier recombination due to stimulated emission.

2.4 Optical feedback and injection

Investigations of optical feedback effects started soon after the first physical demonstration of an SLD [282, 283]. A breakthrough came with seminal publication [220] by Lang and Kobayashi in 1980. Ever since, phenomena such as bistability, instability, self-pulsation, and coherence collapse have been observed and investigated [284–287].

Optical feedback has been used to achieve a variety of means:

- reduction of linewidth [288];

- mode selection;

- side-mode suppression;

- linewidth tuning [289].

Precise control, however, is a prerequisite in order to achieve and retain those qualities,

as the assorted feedback ranges are narrow (*vide* regimes III and V in section 2.4.2) in comparison to the range corresponding to chaotic oscillations (*i.e.* regime IV).

2.4.1 Optical feedback

Consider an extension of the simple internal resonance cavity (as shown in figure 2.1) by supplying it with an external-cavity mirror of reflectivity r_3. Such a configuration is presented in figure 2.2. A common simplification that will be introduced here is such that only one previous reflection is taken into account in the definition of the electric field propagating in the cavities. This approximation is valid for as long as amplitude reflectivity condition $r_2 r_3 \ll 1$ is satisfied. Otherwise, the definition of the electric field would need to include all the previous contributions from the past reflections, such as:

$$E^-(t)e^{i\omega_0 t} = \left[r_2 + (1 - r_2^2)r_3 e^{-i\omega_0 \tau_{ex}} + (1 - r_2^2)r_3^2 e^{-i2\omega_0 t} + \ldots \right] E^+(t)e^{i\omega_0 t}. \quad (2.92)$$

Consider the electric field $E_{ex}^+(t)$ leaving the internal cavity and propagating forward within the external cavity. It will be defined as:

$$E_{ex}^+(t) = \sqrt{1 - r_2^2}\, E^+\left(t - \frac{\tau_{in}}{2}\right), \quad (2.93)$$

where the square root $\sqrt{1 - r_2^2}$ is the amplitude transmission coefficient t_2, which follows from $t^2 + r^2 \equiv 1$. Next, taking into account equation (2.93), the electric field $E_{ex}^-(t)$ propagating backwards in the external cavity (reflected off the external mirror) is defined as:

$$\begin{aligned} E_{ex}^-(t) &= r_3 E_{ex}^+\left(t - \frac{\tau_{ex}}{2}\right) \quad (2.94) \\ &= r_3 \sqrt{1 - r_2^2}\, E^+\left(t - \frac{\tau_{in}}{2} - \frac{\tau_{ex}}{2}\right), \end{aligned}$$

where $E_{ex}^-(t)$ is simply $E_{ex}^+(t)$ after reflection.
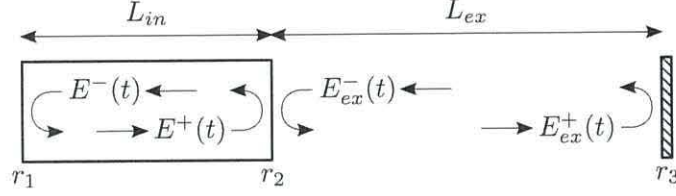
Figure 2.2: Longitudinal field propagation through internal and external laser cavities – The electric field has been split here into four components.

Lastly, taking into account equation (2.94), the electric field $E_2^-(t)$ which has propagated backwards through the rightmost laser facet, and is now propagating inside the internal laser cavity[5] can be defined as:

$$
\begin{aligned}
E_2^-(t) &= \sqrt{1 - r_2^2} E_{ex}^- \left(t - \frac{\tau_{ex}}{2} \right) \\
&= r_3 (1 - r_2^2) E^+ \left(t - \frac{\tau_{in}}{2} - \frac{\tau_{ex}}{2} \right),
\end{aligned}
\tag{2.95}
$$

where $E_2^-(t)$ is $E_{ex}^-(t)$ multiplied by amplitude transmission coefficient.

The following transformation:

$$
E^-(t) = r_2 E^+ \left(t - \frac{\tau_{in}}{2} \right) \qquad \Longrightarrow \qquad E^+(t) = \frac{1}{r_2} E^- \left(t + \frac{\tau_{in}}{2} \right),
$$

where $\tau_{in} = 2\eta_e L_{in}/c$ and $\tau_{ex} = 2L_{ex}/c$, allows for a simplification of equation (2.95):

$$
E_2^-(t) = \frac{r_3(1 - r_2^2)}{r_2} E^+(t - \tau_{ex}).
\tag{2.96}
$$

Finally, complex electric field equation, as stated by Lang and Kobayashi:

$$
\frac{dE(t)}{dt} = \frac{1}{2}(1 + i\alpha) \left[G(t) - \frac{1}{\tau_{ph}} \right] E(t) + \kappa E(t - \tau_{ex}) e^{-i\omega_0 \tau_{ex}},
\tag{2.97}
$$

---

[5]Subscript was added to avoid confusion and distinguish it from $E^-(t)$.

where the feedback rate κ is defined as:

$$\kappa = \frac{1}{\tau_{in}} \frac{r_3(1 - r_2^2)}{r_2}. \tag{2.98}$$

2.4.2 Feedback regimes

What began as an investigation into stability issues which plagued fibre transmission, where back reflections from the front fibre facet was inevitable and led to undesired perturbation of laser's electrical field, turned into attempts and efforts at stabilising lasers and narrowing their emission linewidth [265], especially as it was shown in [290] that laser locks on to the mode with lowest linewidth rather than lowest threshold gain.
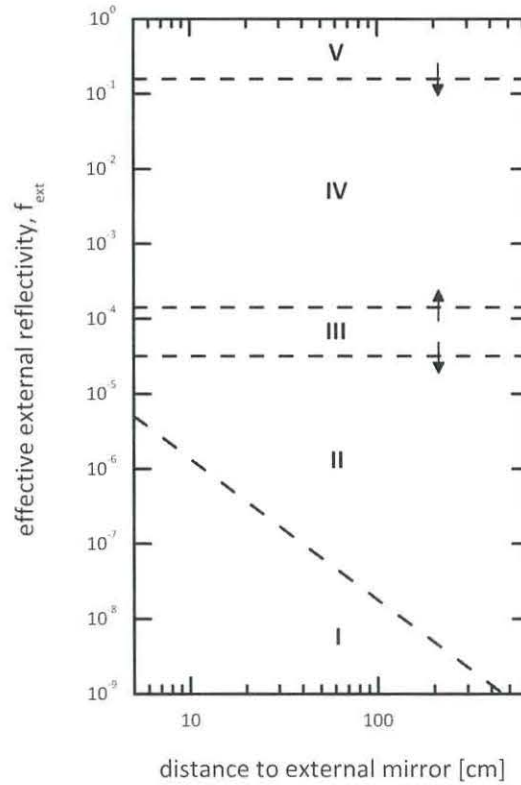
Figure 2.3: Five regimes of operation of a DFB laser subject to external optical feedback – Arrows indicate how the boundaries shift with an increase in drive current; after [221].

50

The five regimes of operation (presented in figure 2.3) of a semiconductor edge-emitting laser subjected to external-cavity feedback are described as [221]:

Regime V Very strong feedback (intentional). To reach this level of feedback, a laser facet (the one facing external feedback mirror) usually needs to be anti-reflection coated. In this case, the dynamics of compound laser cavity is governed by r_1 and r_3, with r_2 merely perturbing the field. Linewidth becomes very narrow and displays a high degree of coherence [291–295].

Regime IV Strong feedback. Termed 'coherence collapse' [286] due to spectacular and unique dynamic properties of compound laser cavity. They manifest themselves through significant reduction of coherence length (centimetres instead of metres), broadband spectrum (reaching tens of GHz), and seemingly erratic, unpredictable fluctuations of electric field [284, 296–298] (first explanation in [299]). It is this regime specifically, with which this thesis is concerned.

Regime III Moderate feedback. Single narrow line. Mode hopping is suppressed. Due to relatively small size, this regime is more difficult to find experimentally, henceforth it is also relatively easy to destabilise a laser operating in this regime through introduction of external perturbation.

Regime II Mode hopping. Multiple steady-state solutions exist, and the compound laser cavity switches between internal- and external-cavity modes. Linewidth is again dependent on both, distance to external feedback mirror and feedback fraction [220, 300–303].

Regime I Only a single external-cavity mode exists. Linewidth is dependent on feedback phase, which in turn is a function of both, distance to external feedback mirror and feedback fraction. As a result, linewidth may either broaden or become narrow [301–303].

Only regimes I and II depend on the feedback distance. The boundary line in figure 2.3 separating these regimes is defined as $C = 1$, where:

$$C = \kappa \tau_{ex} \sqrt{1 + \alpha^2}. \tag{2.99}$$

The exact values of external feedback reflectivity corresponding to boundary lines in figure 2.3 were measured and established for a DFB laser operating at 1.55 µm, therefore they are bound to differ when considering other lasers. However, qualitative result should remain the same [304].

For the explanation of the physical phenomenon[6] behind LEF see [305], whereas for details on quantifying LEF in semiconductor devices, see [306, 307].

LEF was also shown to be responsible for emergence of 'coherence collapse' regime in [290]. Additionally, in the same publication, it was shown that laser with longer internal cavities are less susceptible to chaotic oscillation—for longer diodes it takes higher feedback to enter 'coherence collapse'. It is also shown there that the transition from regime III to regime IV is independent of external cavity length. For discussion on dynamics of short external cavity, see [308–313], whereas for long external cavity, see [314, 315].

2.4.3 The extended Lang–Kobayashi model

This model builds upon the theoretical framework presented in the previous sections; it was first published by Lang and Kobayashi in 1980. The model takes into account optical feedback for each of the two lasers, as well as, the portion of ML's optical field which is injected into the SL; it can be easily extended to cover three or more lasers. It

---

[6]Which amounts to the asymmetric distribution of electrons and holes in semiconductors.

is conceptually equivalent to the schematic in figure 1.1b.

$$\frac{dE_m(t)}{dt} = \frac{1}{2}(1 + i\alpha)\left[G_m(t) - \frac{1}{\tau_{ph}}\right]E_m(t) \tag{2.100}$$
$$+ \quad \kappa_m E_m(t - \tau_{ex})e^{-i\omega_m\tau_{ex}},$$

$$\frac{dE_s(t)}{dt} = \frac{1}{2}(1 + i\alpha)\left[G_s(t) - \frac{1}{\tau_{ph}}\right]E_s(t) \tag{2.101}$$
$$+ \quad \kappa_s E_s(t - \tau_{ex})e^{-i\omega_s\tau_{ex}}$$
$$+ \quad \kappa_c(t)E_m(t)e^{i\Delta\omega t},$$

$$\frac{dN_{m,s}(t)}{dt} = \frac{J}{d} - \frac{N_{m,s}(t)}{\tau_n} - G_{m,s}(t)|E_{m,s}(t)|^2, \tag{2.102}$$

$$G_{m,s}(t) = \frac{g}{1 + \varepsilon|E_{m,s}(t)|^2}\left[N_{m,s}(t) - N_0\right], \tag{2.103}$$

where $\Delta\omega = \omega_m - \omega_s$ is the frequency detuning between the injected optical field from master laser, and that of the slave laser.

The first component on the righthand side of equation (2.100) corresponds to ML's internal field gain–attenuation condition, whereas the second component denotes ML's feedback strength (via κ_m) of the optical field delayed in time and shifted in phase. The first two components on the righthand side of equation (2.101) are analogous to those in equation (2.100). The third component, however, denotes the injected optical field from the ML characterised by injection strength κ_c and detuning $\Delta\omega$. The first component on the righthand side of equation (2.102) corresponds to carriers induced in the laser via direct electrical stimulation. The second and third component denote carrier loss due to spontaneous and stimulated emission, respectively.

The exact approach towards formulation of direct carrier stimulation followed that from [316], and it involves a redefinition of the leftmost term on the righthand side of equation (2.102), from J/d to J/e. Furthermore, the carrier injection term is defined as:

$$J = I_r I_{th}, \tag{2.104}$$

where I_r is a simple multiplication factor, whereas I_{th} denotes threshold current, which is defined as:

$$I_{th} = \frac{eN_{th}}{\tau_n},\tag{2.105}$$

and N_{th} stand for carrier number at threshold, which in turn is defined as:

$$N_{th} = N_0 + \frac{1}{g\tau_{ph}}.\tag{2.106}$$

Optical field intensity for ML and SL was calculated as [316]:

$$P_{m,s}(t) = \frac{\hbar\omega_{m,s}}{\tau_{ph}}|E_{m,s}(t)|^2.\tag{2.107}$$

2.5 Numerical simulation

Due to the complexity of that model, the nonlinear ordinary differential equations are solved numerically. For the purpose of numerically solving the Lang–Kobayashi model, a program was written in Fortran. In literature pertaining to chaos synchronisation phenomena, the three ordinary differential equations are usually integrated with the use of fourth-order Runge–Kutta algorithm as it offers higher accuracy than the Euler method [317] through process of calculating intermediate slope coefficients. Nonetheless, the author of this thesis adopted the latter approach, since it still produced results in qualitative agreement with the former, and was simpler to implement [318]. The results of such numerical simulations can be relied upon[7] to be representative of chaotic oscillations (certain bounds and limitations apply), which is expressed in the so-called 'shadowing lemma', which has been defined by Anosov and Bowen [319, 320]. The cumulative effect of such errors results in exponential divergence of chaotic trajectories, nonetheless it is still comparable with the effect of random noise or choosing slightly different values of initial conditions.

---

[7]Regardless of details of compiler implementation, round-off error or floating-point standard.

Table 2.1: Default numerical simulation parameters – Unless specified otherwise, the parameter values used throughout this thesis were those in this table.

Parameter	Symbol	Value
LEF	α	5
Carrier lifetime	τ_n	2 ns
Photon lifetime	τ_{ph}	2 ps
Internal-cavity round-trip time	τ_{in}	7 ps
External-cavity round-trip time	τ_{ex}	1 ns
Number of carriers at transparency	N_0	$1.5 \cdot 10^8$
Linear gain coefficient	g	$1.5 \cdot 10^{-8}$ ps^{-1}
Gain saturation coefficient	ε	$5 \cdot 10^{-7}$
Background refractive index	n	3.5
Wavelength	λ	780 nm
Facet reflectivity	r_1, r_2	0.548
ML ECM reflectivity	r_{3m}	0.05482
SL ECM reflectivity	r_{3s}	0.01645
Frequency detuning	$\Delta\omega$	0
Current multiplier	I_r	1.85

The set of equations constituting the model were numerically solved using the Euler's method [317]. The zeroth iteration contained values of initial conditions. In the first iteration, the Δ-increments were calculated from the equations and summed with the values from previous iteration. This process would be repeated for the entire simulation. All of the values listed in table 2.1 were taken from [316] and used throughout the whole thesis, unless otherwise stated.

The typical length of a simulation amounted to 220 ns (unless stated otherwise) with an iteration step of 0.2 ps, giving thereby a total number of data points for one variable of $1.1 \cdot 10^6$. The iteration step was chosen so as to amount to a tenth of the shortest characteristic time constant in the model, $\tau_{ph} = 2$ ps, thereby leaving a non-trivial margin for error. This approach was also employed in [316, 321].

Even though time-lag between ML and SL is dependent on the time-of-flight and

not the external-cavity round-trip time [86], the effect of time-of-flight between ML and SL was neglected to improve visualisation of data. Also, as indicated in table 2.1, all the numerical simulations were performed with frequency detuning set to zero.

ML and SL external mirror reflectivity values listed in the table come as a result of an assumption that ML self-feedback amounts to $\kappa_m = 10$ ns^{-1}, whereas SL self-feedback amounts to $\kappa_s = 3$ ns^{-1}. Facet power reflectivity coefficients were assumed to be equal and amount to $R_1 = R_2 = 30\%$, henceforth amplitude reflectiveness $r_1 = r_2 = \sqrt{0.3} \approx 0.548$. The value of r_{3m} was calculated in the following fashion $r_{3m} = \kappa_m \tau_{in} r_2 / (1 - r_2^2)$; the value of r_{3s} was calculated analogously.

In the case of averaged figures, randomisation of values of initial conditions was performed by applying a normally distributed random value of a given parameter up to $\pm 10\%$ of its initial value.

Definition of amplitude within the context of numerically solving the Lang–Kobayashi model is straightforward, however, the definition of phase need some explanation. Phase in every context used throughout this thesis will always mean the angle $\varphi(t)$ between the field vector $E(t)$ and its real component axis, as presented in figure 2.4:
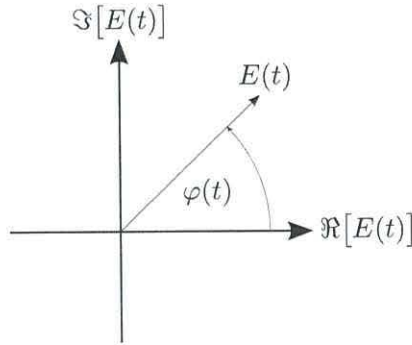
Figure 2.4: Illustration of complex field and optical phase.
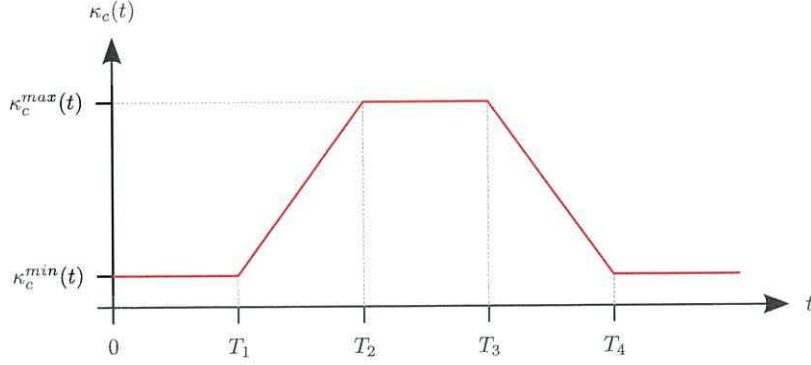
Figure 2.5: A general form of ramping function – For the definition, see equation (2.108).

Definition of ramping function

For the purpose of accounting of the influence of optical injection from ML into SL, the κ_c parameter is present in equation (2.101). However, in order to avoid abrupt step-like changes in injection (from zero to a pre-defined value), as well as, to allow for investigation of SL's dynamics before and after injection, a concept of ramping function was introduced in a form of a linear function. This way, optical injection was introduced into SL in a more gradual fashion.

In a general form, the ramping function is defined in terms of injection rate κ_c as:

$$\kappa_c(t) = \begin{cases} \kappa_c^{min}, & t \leq T_1; \\ \frac{\kappa_c^{max}-\kappa_c^{min}}{T_2-T_1}t + \kappa_c^{min} - \frac{\kappa_c^{max}-\kappa_c^{min}}{T_2-T_1}T_1, & T_1 < t < T_2; \\ \kappa_c^{max}, & T_2 \leq t \leq T_3; \\ \frac{\kappa_c^{min}-\kappa_c^{max}}{T_4-T_3}t + \kappa_c^{min} - \frac{\kappa_c^{min}-\kappa_c^{max}}{T_4-T_3}T_4, & T_3 < t < T_4; \\ \kappa_c^{min}, & t \geq T_4, \end{cases} \qquad (2.108)$$

where T_1 and T_2 stand for time points between which injection transits from the minimum to maximum value, and T_3 and T_4 stand for time points between which injection transits from the maximum to minimum, see figure 2.5.

Throughout this thesis it has been assumed that $\kappa_c^{min} \equiv 0$, thus the above set of equations can be simplified to the following form:

$$\kappa_c(t) = \begin{cases} 0, & t \leq T_1; \\ \frac{\kappa_c^{max}}{T_2-T_1}t - \frac{\kappa_c^{max}}{T_2-T_1}T_1, & T_1 < t < T_2; \\ \kappa_c^{max}, & T_2 \leq t \leq T_3; \\ -\frac{\kappa_c^{max}}{T_4-T_3}t + \frac{\kappa_c^{max}}{T_4-T_3}T_4, & T_3 < t < T_4; \\ 0, & t \geq T_4, \end{cases} \qquad (2.109)$$

where the value of κ_c^{max} is defined on a per-simulation basis.

2.6 Conclusions

This chapter constitutes the entire mathematical and physical framework of this thesis. It began with a brief reminder of the history and development of semiconductor lasers[8] in section 2.1. Then, in section 2.2, a summary of the most characteristic traits of semiconductor lasers against other lasers is provided.

Section 2.3 deals with the derivation of the mathematical apparatus, beginning from the Maxwell's equations, through Maxwell–Bloch model and Lorenz–Haken model, concluding with semiconductor rate-equations.

Section 2.4 is focused on phenomena accompanying optical feedback and optical injection. This is also where the Lang–Kobayashi model is presented along with phenomenological demarcation of feedback regimes.

Lastly, details and remarks on the approach to numerical simulation applied in this thesis are found in section 2.5.

---

[8]For the sake of brevity, only relevant topics and events directly pertinent to the matter of this thesis were included in that list.

Chapter 3

Experimental chaos synchronisation of ECSLDs

This chapter deals with two separate, yet similar, surveys of experimental synchronisation of two SLDs in a Master–Slave configuration. In both cases, the employed set-ups assumed the open-loop unidirectional configuration (see figure 1.1a). The motivation for these surveys was twofold:

- investigation of the influence of ML's and SL's drive currents and their temperatures on cross-correlation coefficient (CCC) and the calculation of the spectral transfer function (STF) (section 3.1);

- the influence of four sinusoidal messages on the correlation coefficient (CC), CCC, and STF as a function of message rf power ranging from -30 to -5 dBm, as well as, the efficacy of a naïve eavesdropper on the transmission channel (section 3.2).

The main objective for this chapter in general is to present initial results, as well as, to confirm that the methodology employed is adequate to analyse the data and draw conclusions.

Correlation coefficient

Correlation coefficient plots were also calculated in Origin® and obtained as a result of linear regression fitting with the ML time-domain data plotted against the SL time-domain data. The Origin® Reference Manual states that its implementation of the fitting function is defined in the form of $y_i = A + Bx_i$, where the A and B parameters are computed using the least-squares method. The former is calculated at the intercept:

$$A = \overline{y} - B\overline{x}, \tag{3.1}$$

where $\overline{x}$ and $\overline{y}$ represent arithmetic averages of x and y data sets, respectively. Finally, the latter (which denotes the slope) is calculated with the following formula:

$$B = \frac{\sum_{i}^{N}(x_i - \overline{x})(y_i - \overline{y})}{\sum_{i}^{N}(x_i - \overline{x})^2}. \tag{3.2}$$

Accordingly, the standard deviation SD is calculated with the following equation:

$$SD = \sqrt{\frac{\sum_{i=1}^{N}[y_i - (A + Bx_i)]^2}{N - 2}}, \tag{3.3}$$

where x_i and y_i are the data points, and N stands for the number of data points.

FFT

The spectral transfer function (STF) is defined here as a ratio of SL and ML amplitude spectra. All the Fast Fourier Transform calculations were performed in Origin®, which implements the Danielson–Lanczos method [322, 323]. This is a form of Discrete Fourier

Transform of length N, whose n-th point is denoted by F_n and defined as [324]:

$$
\begin{aligned}
F_n &= \sum_{k=0}^{N-1} e^{-2\pi i k n/N} f_k \\
&= \underbrace{\sum_{k=0}^{P-1} e^{-2\pi i k n/P} f_{2k}}_{\text{even } n} + W^n \underbrace{\sum_{k=0}^{P-1} e^{-2\pi i k n/P} f_{2k+1}}_{\text{odd } n} \\
&= F_n^e + W^n F_n^o,
\end{aligned}
\tag{3.4}
$$

where $W = e^{-2\pi i/N}$, $P = N/2$, and $n = 0, \ldots, N$.

Cross-correlation

All the cross-correlation (CCC) analyses were performed with use of Origin®, where this particular function is based on Fast Fourier Transform. The actual algorithm employed takes the following form:

$$
y(m) = \sum_{n=0}^{M-1} f(n)g(n-m) = \text{iFFT}(FG^*),
\tag{3.5}
$$

where $y(m)$ is the cross-correlation function, $f(n)$ and $g(n)$ are the input signals, iFFT denotes the inverse FFT, whereas F and G are the Fourier transforms of $f(n)$ and $g(n)$, respectively. Normalisation of input functions was not available in the 6.1 version of Origin®, hence the CCC plots do not conform to $[-1 : +1]$ value range.

3.1 Synchronisation of two SLDs

Experimental configuration

The experimental configuration employed in this experiment is depicted in figure 3.1; it is a practical implementation of the open-loop set-up as seen in figure 1.1a whereby only the ML was subject to variable optical feedback. The injection arm (*i.e.* the
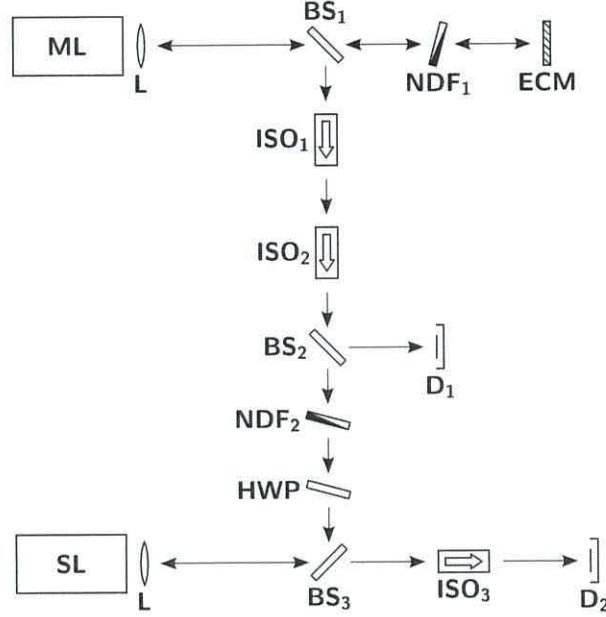
Figure 3.1: Experimental set-up – BS (beam splitter), D (detector), ECM (external-cavity mirror), HWP (half-wave plate), ISO (optical isolator), L (collimating lens), NDF (natural density filter).

one between beam splitters BS_1 and BS_3) was composed of two optical isolators, an optical attenuator, and a half-wave plate. Two isolators were used to achieve cumulative isolation of *ca.* -80 dB since a single isolator would be insufficient to block the back-reflection from SL resulting in deleterious modulation of ML *by* the SL (see figure 2.3). The ML's time-domain optical power trace was recorded with detector D_1, whereas SL's time-domain optical power trace was recorded with detector D_2.

Both SLDs used were single-mode, double-heterostructure, Fabry–Pérot Access Pacific APL830-40SM laser diodes; they shared the same value of solitary threshold current of $I_{th} \approx 27$ mA, and the same value of solitary lasing wavelength $\lambda \approx 830$ nm. They were driven by ultra-low-noise current sources ILX-Lightwave LDX-3620, and their temperature was controlled by thermo-electric controllers ILX-Lightwave LDT-5412 to a precision of 0.01 K. The laser output was collimated by an anti-reflection-coated laser-diode objective Newport FLA11. All the optical isolators were OFR-IO-5-NIR-HP with

Table 3.1: Default values of the parameters of the experimental chaos synchronisation employed in the parameter sweep.

Parameter		Value
I_{ML}	[mA]	30.09
I_{SL}	[mA]	29.99
T_{ML}	[°C]	24.17
T_{SL}	[°C]	23.17

nominal isolation of -41 dB. Lastly, both detectors were linear, multimode (62.5 μm), ac-coupled Newport AD-70xr with 3 dB voltage bandwidth of 6 GHz, 10–90% rise time of 70 ps, and spectral response between 700 and 1650 nm. The photodetectors' output voltage (linearly proportional to the incident optical power) was monitored on LeCroy WaveMaster 8600A digital oscilloscope with a bandwidth of 6 GHz.

The entire set-up was constructed so as to ensure that as far as possible all laser beams would remain either perpendicular to, or parallel with, one another, whilst being parallel with the plane of the optical table at all times. Both NDFs and the HWP were aligned obliquely so as to form a non-normal angle between the incident optical beam and the components' facets, thereby reducing the etalon effect and back-reflection. No optical attenuators were used to adjust power levels incident on the detectors.

Basic laser parameters

Drive currents and lasers' temperatures were adjusted; their default values are listed in table 3.1. ML self-feedback rate (via the NDF$_1$) and injection rate (via the NDF$_2$) were adjusted, however, their values were not recorded due to the physical size limit of the experimental set-up. Additionally, owing to the uncertainty associated with quantifying the injection rate in an experiment (owing to reflection losses or confinement factor), it will be assumed that the beam splitters separate the optical beams in 50–50 ratio. Each ISO was measured to attenuate the incident optical beam by *ca.* 1.5 dB.

Basic experimental procedure

The optimisation procedure followed is outlined below:

1. Upon switching both lasers on, their drive currents would be set to be *ca.* 10–20% above their threshold currents, and their temperatures would be set at the values that were established by the author to be stable in a previous experimental study using these devices. To prevent interaction between the lasers, the injection arm would remain blocked.

2. The set-up would be left undisturbed for 30 minutes[1] to reach equilibrium with the environment.

3. ML would be rendered chaotic through an iterative process of adjusting the values of the drive current, operating temperature, and self-feedback rate.

4. The injection arm would be unblocked.

5. Two optical isolators—ISO_1 and ISO_2—would be aligned so as to provide the isolation of *ca.* −40 dB each. The optical beam, after passing the two isolators, would be rotated by approximately $\pi/2$ in relation to the ML output optical beam.

6. The half-wave plate would be aligned so as to achieve the maximum injection rate by rotating the injected optical beam to be parallel with SL output optical beam. To this end, SL's optical power would be monitored in real time on the digital oscilloscope.

7. SL would be rendered chaotic through an iterative process of adjusting its drive current, operating temperature and injection rate (via the NDF_2). The synchronisation quality would be monitored in real time on the digital oscilloscope. Any further adjustments of SL's parameters would be introduced so as to bring the CC as close as possible to unity.

---

[1]Local practice.

Four separate surveys were performed—each time one variable was chosen and adjusted either side of a nominal value whilst keeping the other three constant. The four variables chosen were: ML drive current I_{ML}, SL drive current I_{SL}, ML temperature T_{ML}, and SL temperature T_{SL}. Every time, time-domain traces would be recorded for ML and SL, whereas their FFT spectra would be calculated afterwards (see figure 3.2).

To obtain CCC plots in figures 3.3 and 3.4, cross-correlation of ML and SL time-domain intensities was performed in Origin®. The resultant 2D plots were aggregated to form 3D contour plots. In addition, the peak values of the CCC were recorded separately and are presented in figure 3.5. To obtain the STF in figure 3.7, FFT of the SL time-domain optical power was divided by the FFT of the ML time-domain optical power and subsequently smoothed using 50-point adjacent averaging. All the intermediate STFs were aggregated together to form 3D contour plots.

Typical temporal and spectral traces

Typical time- and frequency-domain traces are presented in figure 3.2. In comparison to ML presented in figure 3.2a, the SL's time-domain optical power trace in figure 3.2b displays higher amplitude oscillation induced by the injection. The time-of-flight between the two lasers was not recorded as it was not the object of the experimental investigation. However, the optical path length approximately amounted to the length of ML external cavity (see equation (3.7)).

The multiple peaks seen in the spectra of the ML and SL in figures 3.2c and 3.2d are the consequence of external-cavity modes (XCMs) that satisfied the external-cavity resonance condition of the form:

$$f_m = m \cdot \frac{c}{2nL},$$ (3.6)

where m is integer and denotes subsequent cavity modes, f_m is the frequency of the
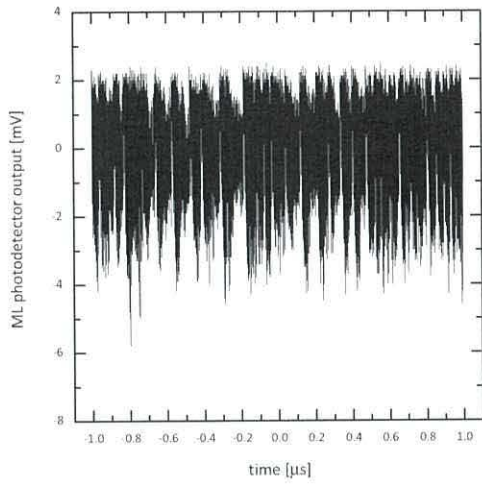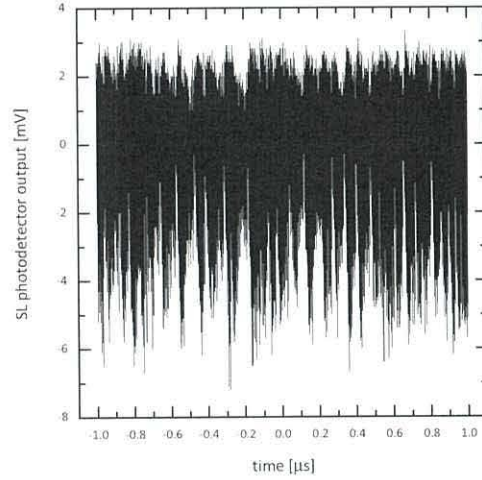
65

(a) ML time-domain optical power trace.

(b) SL time-domain optical power trace.
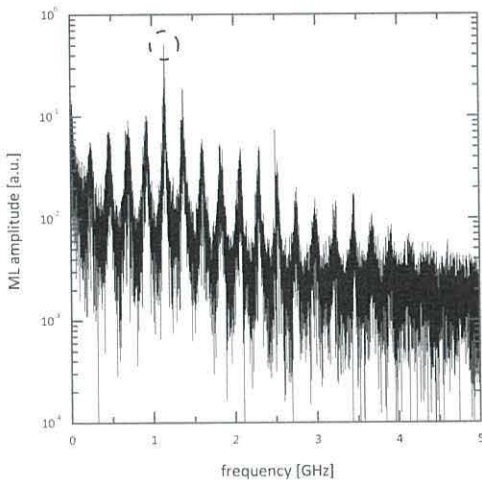
(c) ML frequency-domain amplitude trace.
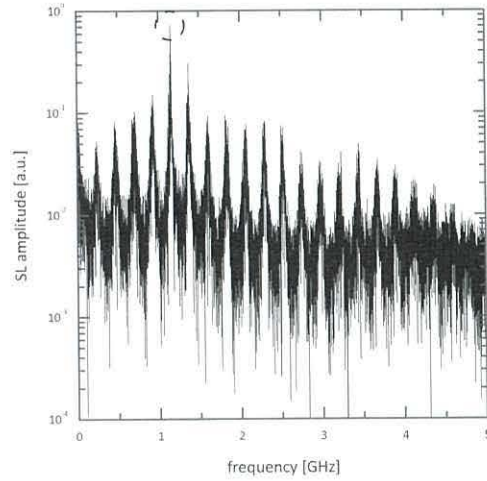
(d) SL frequency-domain amplitude trace.

Figure 3.2: Typical time-domain and frequency-domain traces for ML and SL – Time-domain traces were obtained simultaneously, whereas the FFT data were calculated separately after the experiment. The dashed circles indicate the highest peak in both spectra. Detector's typical conversion gain at 850 nm is 300 V/W.

given mode, c is the speed of light in vacuum, n is the refractive index of the propagation medium, and L is the length of the cavity.

To infer the approximate length of ML's external cavity L_{ex}, the highest peak in both the ML and the SL FFT spectra (as indicated with dashed circle in figures 3.2c and 3.2d) will be used; it is the fifth-order mode and it corresponds to the frequency $f = 1.151123$ GHz. Further, by neglecting the influence of ML's internal cavity[2] and essentially assuming that the medium of propagation is air (*i.e.* $n \equiv 1$), one arrives at the following transformation of equation (3.6):

$$
\begin{aligned}
L_{ex} &= m \cdot \frac{c}{2nf_m} \\
&= 5 \cdot \frac{299,792,458 \, \frac{m}{s}}{2 \cdot 1 \cdot 1.151123 \cdot 10^9 \, \frac{1}{s}} \\
&\approx 65.109 \text{ cm.}
\end{aligned}
\tag{3.7}
$$

The uncertainty of the value of the frequency was equal $\Delta f = 610$ kHz, which translates into uncertainty of the length of ML's external cavity of $\Delta L_{ex} \approx 0.035$ cm.

Results

As reported by other researchers [87, 88, 92], spectral profiles of the chaos-synchronised SL (as seen in figure 3.2d) clearly display attenuation of the low-frequency components, and amplification of high-frequency components with respect to spectrum of ML (figure 3.2c).

The blue and red horizontal lines present in figure 3.4 correspond to the local minima and maxima in CCC plots (for a cross-section, see figure 3.3). The vertical spacing between those lines corresponds to external-cavity round-trip time and amounted to

---

[2]Specifically, length of its internal cavity and its index of refraction.

Figure 3.3: Typical CCC plot of a state of high chaos synchronisation between ML and SL – The trace was normalised so as to reach unity at lag equal to zero.

$T_{rtt} = 4.3$ ns, which equates to ML's external-cavity length of:

$$
\begin{aligned}
L_{ex} &= \frac{c \cdot T_{rtt}}{2} \\
&= \frac{299,792,458 \ \frac{\text{m}}{\text{s}} \cdot 4.3 \cdot 10^{-9} \ \text{s}}{2} \\
&\approx 64.5 \ \text{cm}.
\end{aligned}
\tag{3.8}
$$

The uncertainty of the value of the round-trip time was equal $\Delta T_{rtt} = 0.1$ ns, which translates into uncertainty of the lengt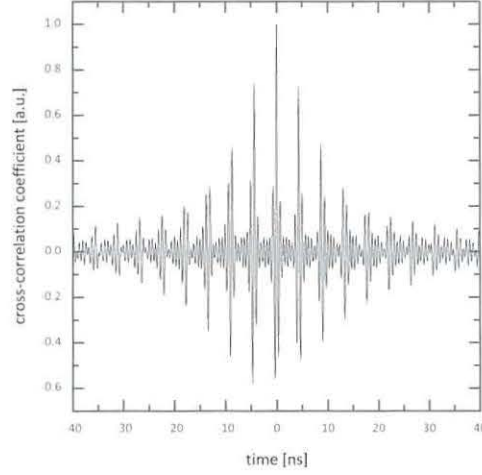h of ML's external cavity of $\Delta L_{ex} \approx 1.5$ cm. *Ergo*, the values obtained in equations (3.7) and (3.8) are in agreement.

Even though the set-up was aligned for a specific ML drive current and temperature, the CCC increased when the I_{ML} was increased (see figures 3.4a and 3.5a). Increasing the current, increases the injected optical power, which thereby affects the SL's optical field to a higher degree. As a consequence, the correlation between the two optical fields increases and SL's modulation performance also increases turning SL into an optical amplifier (one which also introduces some noise, especially in the high-frequency region).

(a) ML drive current sweep.

(b) SL drive current sweep.

(c) ML temperature sweep.

(d) SL temperature sweep.
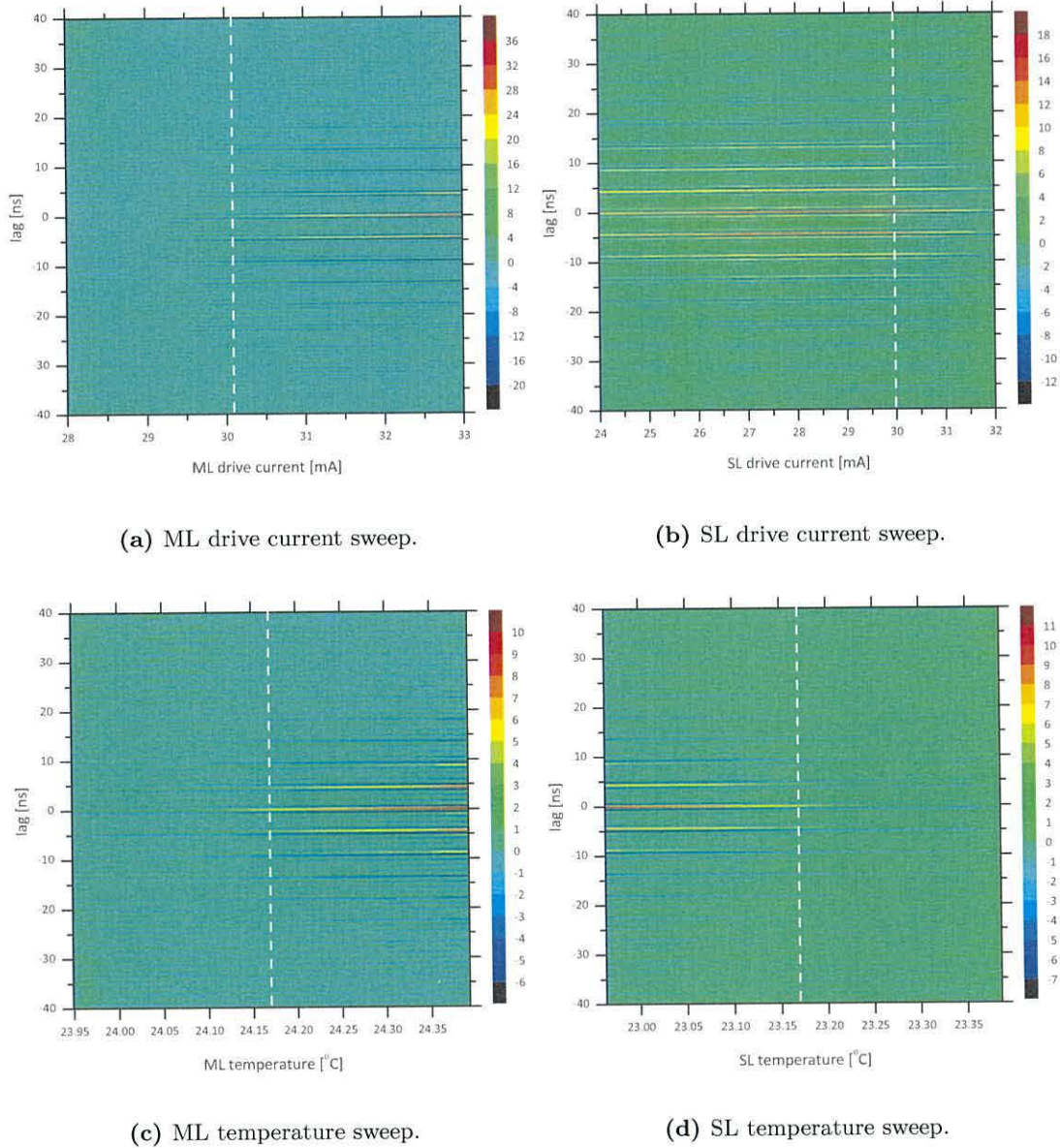
Figure 3.4: Contour plot of CCC for four sweeps – The colour scale denotes the magnitude of the CCC [a.u.]. The white dashed lines signify the default setting, see table 3.1.
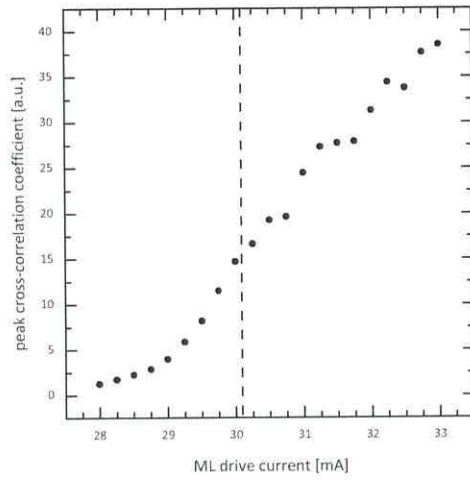
(a) ML drive current sweep.

(b) SL drive current sweep.

(c) ML temperature sweep.

(d) SL temperature sweep.

Figure 3.5: Maximum CCC for four sweeps – The black dashed lines signify the default setting, see table 3.1.

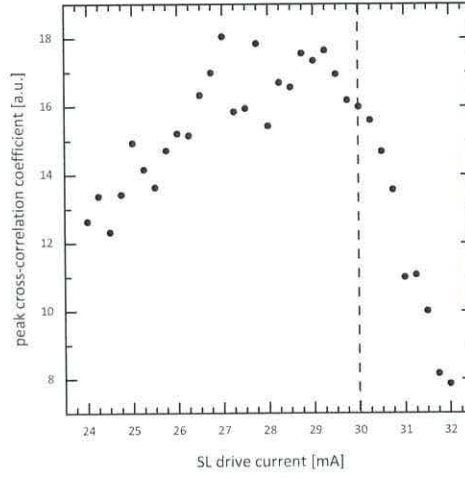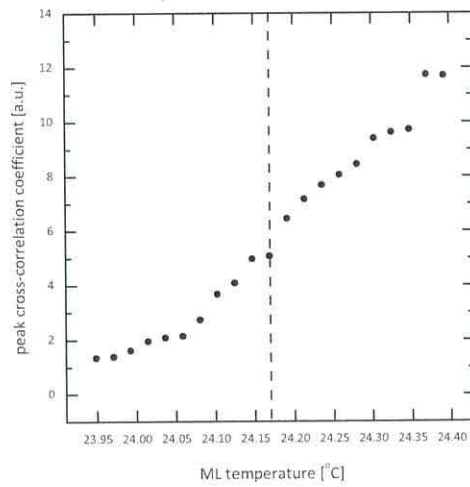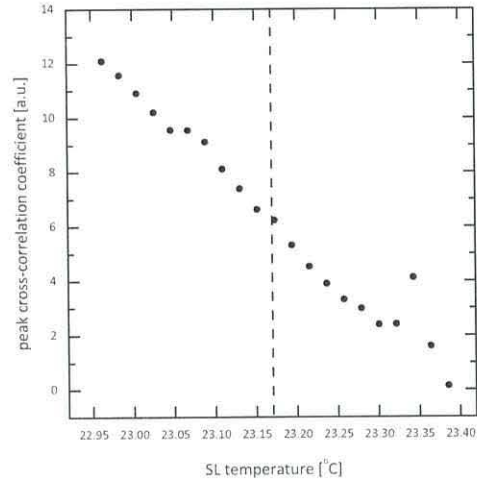The reason for flat CCC trace on the left hand side of figure 3.4a stems from the fact that the set-up was originally aligned for a current as indicated by the dashed line, therefore lowering the value of the ML drive current resulted in significant loss of synchronisation between the lasers. The lasers still oscillated chaotically, however, the quality of synchronisation was so low that the correlation pattern was of a negligible scale. Only after increasing the I_{ML} beyond the dashed line did the synchronisation sufficiently develop giving rise to stronger CCC (see figures 3.4a and 3.5a). In contrast, the CCC in figure 3.4b proved to be somewhat independent of I_{SL} for the chosen parameter space. Initially, with increasing I_{SL} the synchronisation improved, as the injected signal experienced more benefit from increased number of photons in the SL's cavity. Then a region of maximum synchronisation was achieved (for I_{SL} between 27 and 29 mA, see figure 3.5b). Finally, SL's dynamics overcame the injection from the ML and the SL's inherent dynamics dominated over the injected field thereby diminishing the CCC. A global maximum in the CCC as a function of I_{SL} was observed since the SL's dynamics (as expressed in equation (2.101)) are always dependent upon the balance between inherent and injected optical fields.

The temperature sweep performed on each laser is equivalent to altering the length of its internal cavity, thus altering its lasing frequency, which finally is equivalent to traversing the injection-locking diagram (see figure 3.6) *horizontally* (in contrast to the aforementioned current sweeps that traverse the diagram *diagonally*), hence the steep gradient of the scatter plots in figures 3.5c and 3.5d. Further information pertaining dynamics of frequency-mismatched lasers can be found in [325, 326]. Asymmetrical dependence on frequency detuning predicted theoretically [92] is not evident in figures 3.4c, 3.4d, 3.5c, and 3.5d which show a symmetrical nature of injection-locking dynamics between two frequency-mismatched SLDs.

Within the limited bounds of this survey, the inequalities $\omega_{ML} > \omega_{SL}$ and $\omega_{ML} < \omega_{SL}$ were found to be experimentally equivalent. It is speculated that due to relatively low
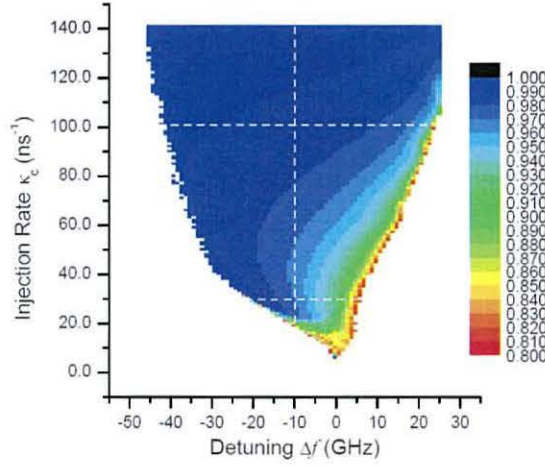
Figure 3.6: Typical injection-locking diagram – Contour plot values were calculated as a function of injection strength and frequency detuning between ML and SL. The colour scale denotes the maximum value of normalised CCC; after [316].

value of the drive current, the lasers could have been operating around the zero-detuning apex area at the bottom of injection-locking diagram, which is characterised by the diagram being less asymmetrical [263, 276, 327, 328].

The undulations found in figure 3.5a correspond to optical power undulation of an ECSLD as described in [220]. Even though the reference reports on undulations in optical power as a function of drive current, it is not unreasonable to claim that such undulations would translate into undulations in CCC of optical power traces. Alternatively, they could perhaps be attributed to the particular—not normalised—definition of CCC function used in Origin® (see equation (3.5)).

Comparing figures 3.7a to 3.5a, and 3.7b to 3.5b, would suggest that a hallmark of high-quality synchronisation is amplification in SL of the frequency components above *ca.* 2.5 GHz. It is also accompanied by minimal attenuation of low-frequency components. Decreasing the ML temperature (and consequently decreasing the effective length of the internal cavity) gave rise to significant damping of the frequency components up until 2 GHz, as presented in figure 3.7c. On the other hand, increasing ML temperature (and also increasing the effective length of the internal cavity) resulted in 1.5–4 GHz

(a) ML drive current sweep.

(b) SL drive current sweep.

(c) ML temperature sweep.

(d) SL temperature sweep.
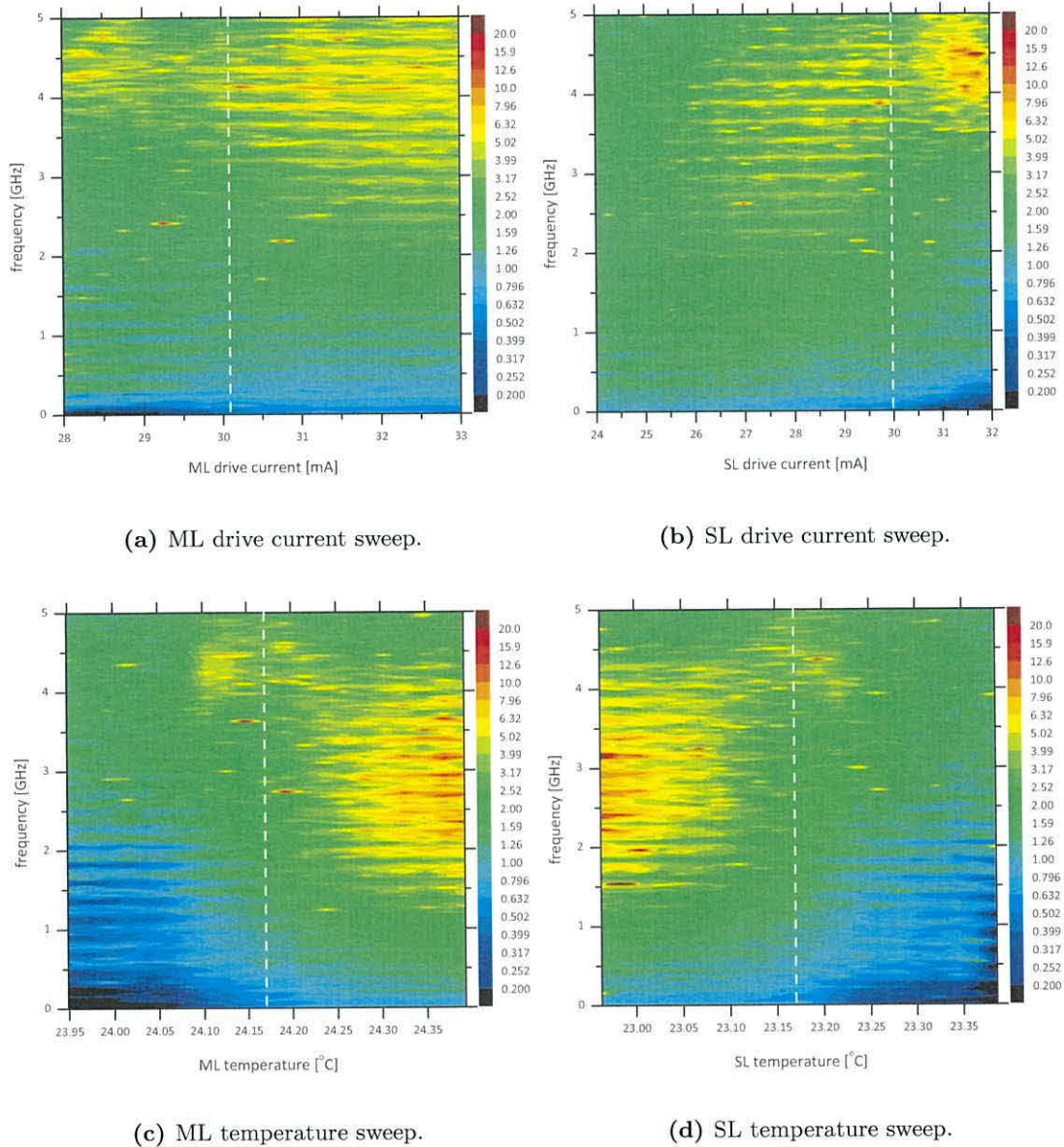
Figure 3.7: Contour plot of STF for four sweeps – The colour scale denotes the magnitude of the STF. The white dashed lines signify the default setting, see table 3.1. Data were smoothed with 50-sample adjacent smoothing.

frequency range experiencing significant amplification in the SL. Figure 3.7d displayed a mirrored pattern.

A certain correspondence exists between CCC plots and spectral features in STF contour plots. Namely, the highly correlated left hand side of figure 3.5c corresponds to the highly amplified frequency range 1.5–4 GHz in figure 3.7c. The poorly correlated right hand side of figure 3.5c corresponds to highly attenuated frequency range 0–2 GHz in figure 3.7c effectively preventing any synchronisation. The same pattern (albeit mirrored) was observed for T_{SL} sweep and is displayed in figures 3.5d and 3.7d.

Intriguing is the presence of amplified and concentrated high-frequency components between 4 and 5 GHz in figure 3.7b. What it could suggest is the emergence of a different chaotic attractor resultant from the SL overcoming the injection from the ML, which resulted in loss of synchronisation in figures 3.4b and 3.5b. For analysis of dynamics of a system where two chaotic attractors are present simultaneously, see [329].

3.2 Synchronisation and transmission of a message

Experimental configuration

The configuration employed in this experiment is depicted in figure 3.8. It was different from the previous set-up in that the ML was driven by both, a dc bias current and an ac signal component coming from a Marconi Instruments signal generator, model 2022, with a frequency range of 10 kHz–1 GHz. In effect, the ML employed Chaos Modulation (CMO) scheme (as described in section 1.4) in which this sinusoidal signal acted as a simple message. Experimental components employed here were identical with the ones used in the previous section. The influence of the message was investigated by varying the message power and frequency. Additionally, a naïve attempt at eavesdropping was performed [141]. For discussion on interception of message in open- and closed-loop set-ups, see [96].

Figure 3.8: Experimental set-up – BS (beam splitter), D (detector), ECM (external-cavity mirror), HWP (half-wave plate), ISO (optical isolator), L (collimating lens), NDF (natural density filter), SG (signal generator).

In this experiment, owing to the relative proximity of the values of lasers' drive currents to their threshold currents, they both operated in low-frequency fluctuation (LFF) regime which is characterised by occurrence of sudden drop-outs in power followed by gradual build-ups [299, 330–333]. This region is reported [334] to exist all along the boundary between regimes IV and V not only for drive current slightly above threshold, but specifically for higher values, too.

LFF was originally reported in [282]. Later, it was linked with a kink in light–current [335, 336] plots. LFF is also classified as time-inverted type-II intermittency [337] and origins of its power drop-outs are investigated in [338]. Statistical analysis of distribution of power drop-outs is performed in [339]; in general, LFF can occur without spontaneous emission [340], however, both spontaneous emission noise [341] and multi-mode effects [340] can affect LFF dynamics. When it comes to fulfilling external-cavity resonance condition, in the case of LFF it is mostly the maximum-gain

Table 3.2: **Parameters of the experimental chaos synchronisation with transmission of message.**

Parameter		Setting	
		Match	Mismatch
I_{ML}	[mA]	30.09	31.09
I_{SL}	[mA]	29.99	30.99
T_{ML}	[°C]		24.26
T_{SL}	[°C]		23.13

mode which is the most stable [333], whereas, far above threshold at weak feedback it is mostly the minimum-linewidth mode owing to linewidth enhancement factor (LEF) [290, 342]. Lastly, question of inducing LFF and stabilising LFF through drive current modulation is discussed in [343].

Basic experimental procedure

The procedure used was very much similar to the one employed in the previous section, however, the experiment consisted of two sub-experiments:

- the parameter-matched case, which was equivalent to legitimate chaos synchronisation;

- the parameter-mismatched case, when the lasers' drive currents were both increased by 1 mA (see table 3.2), which represented a hypothetical eavesdropper imperfectly synchronised with ML.

The aligning procedure was the same as the one mentioned in the previous section; the ML was rendered chaotic by adjusting its drive current, temperature and self-feedback rate. Subsequently, the SL was rendered chaotic by adjusting its drive current, temperature and injection rate. Up until this stage no message was applied and the synchronisation quality was approximately 65%.

The first sub-experiment began by fixing both lasers' parameters (see table 3.2, 'match' column). The message was then applied to ML without any further adjustment of the ML's and SL's parameters. Sinusoidal messages of four frequencies and six modulation depths were applied in separate measurements. The second sub-experiment followed the same procedure as the first one, with the only difference being adjustment of the values of I_{ML} and I_{SL} (see table 3.2, 'mismatch' column).

In order to estimate the ac currents flowing through ML when modulated by the signal generator, the Shockley ideal diode equation was employed:

$$I = I_0 \left(e^{\frac{qU}{k_B T}} - 1 \right), \tag{3.9}$$

where I is the diode current, I_0 denotes the reverse bias saturation current, U is the voltage across the diode, q is the elementary charge, k_B is the Boltzmann constant, and T is the absolute temperature of the p-n junction. Typical values of $I = 55$ mA and $U = 2$ V were obtained from the diode manufacturer's data sheet; those values were used to calculate $I_0 \approx 6.795 \cdot 10^{-36}$ A.

Equation (3.9) was then transformed in order to calculate the values of voltage across the diode for the two drive currents employed in this experiment:

$$U = \frac{k_B T}{q} \ln \left(\frac{I}{I_0} + 1 \right). \tag{3.10}$$

The two values of voltage (1.9846 V for matched and 1.9854 V for mismatched cases) from equation (3.10) were then used in calculation of dynamic slope resistance as a derivative of equation (3.9):

$$\frac{dI}{dU} = \frac{q}{k_B T} I_0 e^{\frac{qU}{k_B T}} = \frac{1}{R_d}. \tag{3.11}$$

Table 3.3: Message ac current for the matched case as a function of message power and frequency – Values displayed in milliamperes.

Power	Frequency			
[dBm]	1 MHz	10 MHz	100 MHz	1 GHz
−5	3.466	3.392	3.107	2.168
−10	1.947	1.962	1.804	1.475
−15	1.086	1.082	0.991	0.789
−20	0.598	0.575	0.541	0.420
−25	0.345	0.322	0.301	0.233
−30	0.197	0.187	0.168	0.131

Function generator output voltages were measured in an open circuit set-up for all the modulation depths and message frequencies, which then were used to calculate ac currents flowing through the diode:

$$i = \frac{u}{R_{fg} + R_d},$$
(3.12)

where R_{fg} stands for generator's output impedance of 50 Ω. The resulting values of current are presented in table 3.3. The difference between the ac current values for matched and mismatched case amounted to less than 0.05%, hence only values of the former are included. As can be appreciated from table 3.3, message power level of −5 dBm quite possibly could have forced the ML to operate below its threshold current, whereas −10 dBm brought the ML just above its I_{th}.

Figures 3.9 and 3.10 were obtained analogously to the ones in previous section. To obtain correlation plots in figure 3.11, the ML time-domain optical power was plotted against SL time-domain optical power and linear regression was performed for four frequencies and six modulation depths, for both parameter settings. The methodology employed to obtain all the CCC and STF contour plots was the same as that employed in the previous section.

Typical temporal and spectral traces

Typical time- and frequency-domain traces are presented in figures 3.9 and 3.10. The important observation here is the perturbation introduced to, and caused by the application of message in CMO scheme. Specifically, the time-domain traces upon closer inspection revealed a conspicuous waveform envelope, thereby immediately suggesting the presence of a non-chaotic component (highlighted by the red dotted curves in figures 3.9a and 3.9b, as well as, 3.10a and 3.10b). Application of messages at rf power levels of -25 dBm and above introduced perturbation to the time-domain traces in the form of the aforementioned waveform envelope. Those perturbations were the most pronounced for the rf message frequencies of 1 MHz and 10 MHz.

Another important point is that even at very low rf power (see figures 3.9c and 3.9d) the applied message can be readily extracted by a casual observer by subtracting the spectra of the intercepted optical beam from the spectra of the eavesdropper's laser and then applying low-pass filtering. The task becomes even easier for higher rf powers. For the message frequency of 1 GHz (as presented in figures 3.10c and 3.10d), the message suffered from attenuation. That attenuation of low-frequency components of SL spectrum in figures 3.9d and 3.10d is similar to that presented in the previous section in figure 3.2d. Nonetheless, even in such an unfavourable setting, message extraction could still be effected by a casual observer.

It is argued in [83] that the power of the hidden message needs to be kept below 5% of chaos power in order to remain inconspicuous. However, in this survey, messages as low as 0.7% could be appreciated by a casual observer. It is speculated that this almost an order of magnitude difference stems from the fact that in this experiment the lasers operated very close to their threshold currents.

In this experiment, it was the seventh XCM that was the most pronounced, and it corresponds to the frequency $f = 1.611938$ GHz (see figures 3.9c and 3.9d, as well as,
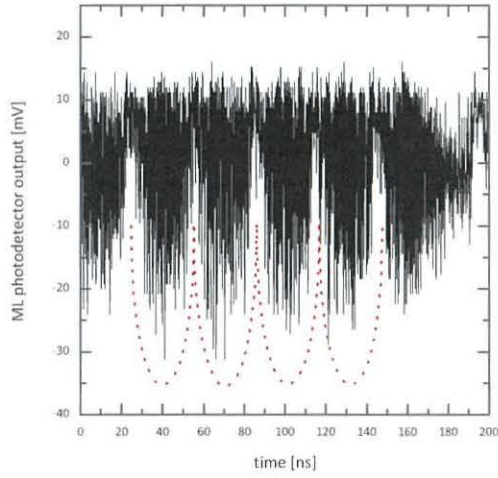
(a) ML time-domain optical power trace.
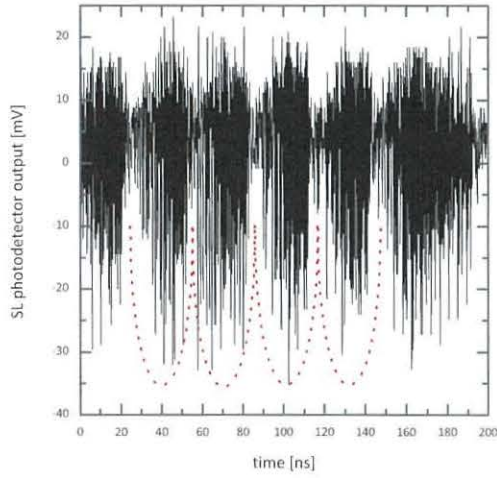
(b) SL time-domain optical power trace.
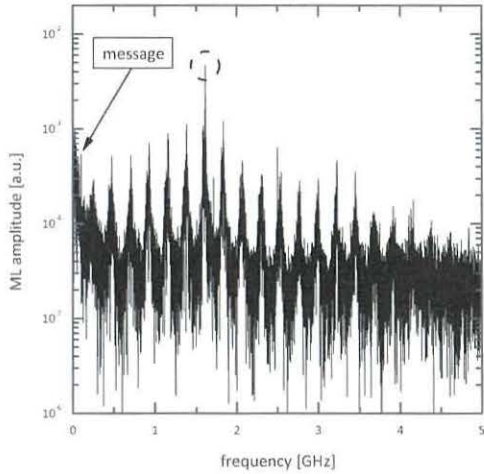
(c) ML frequency-domain amplitude trace.
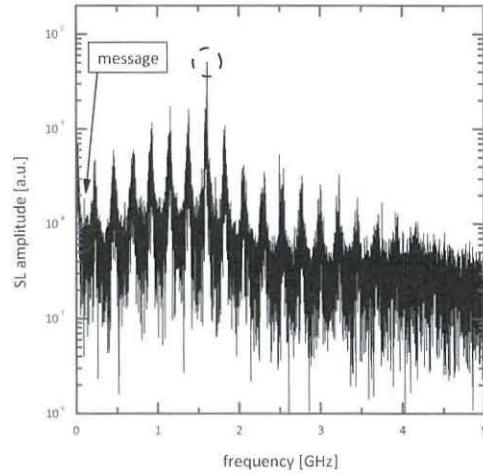
(d) SL frequency-domain amplitude trace.

Figure 3.9: Typical time-domain and frequency-domain traces for ML and SL with message frequency of 100 MHz at −25 dBm – Parameter-match set-up. Time-domain traces were obtained simultaneously, whereas the FFT data were calculated separately after the experiment. The dashed circles indicate the highest peak in both spectra. Red dotted curves highlight the effect of hidden message. Detector's typical conversion gain at 850 nm is 300 V/W.
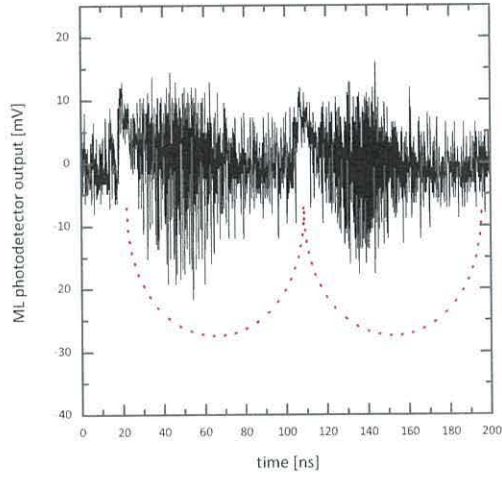
(a) ML time-domain optical power trace.

(b) SL time-domain optical power trace.
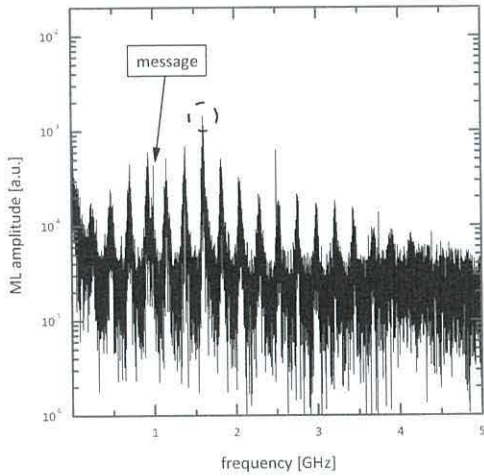
(c) ML frequency-domain amplitude trace.
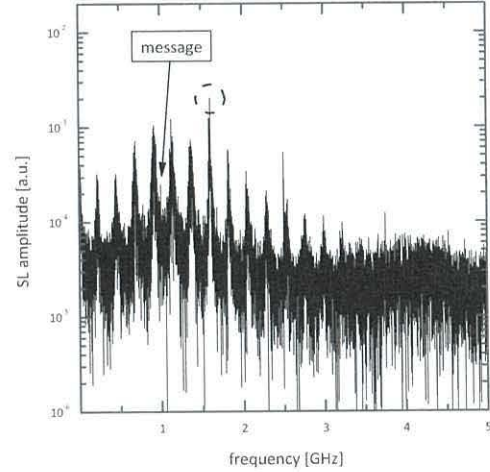
(d) SL frequency-domain amplitude trace.

Figure 3.10: Typical time-domain and frequency-domain traces for ML and SL with message frequency of 1 GHz at −10 dBm – Parameter-match set-up. Time-domain traces were obtained simultaneously, whereas the FFT data were calculated separately after the experiment. The dashed circles indicate the highest peak in both spectra. Red dotted curves highlight the effect of hidden message. Detector's typical conversion gain at 850 nm is 300 V/W.

3.10c and 3.10d). Therefore, frequency separation between XCMs amounted to:

$$
\begin{aligned}
f_{sep} &= \frac{f_m}{m} \\
&= \frac{1.611938 \cdot 10^9 \, \frac{1}{s}}{7} \\
&\approx 230 \text{ MHz},
\end{aligned}
\tag{3.13}
$$

which excludes the possibility that any of the message frequencies could have resonated as a harmonic of external round-trip time.

Results

For all the modulation depths the chaotic waveforms concealing a 100 MHz sine wave experienced the highest CC value (see figure 3.11a), especially between rf power levels of -25 and -20 dBm. Furthermore, in the parameter-mismatched case, the frequency of 100 MHz retained a fairly stable value of correlation, whilst the other three frequencies experienced a decrease (see figure 3.11b).

In general, increasing the rf power of the masked message resulted in decreased CCC, as can be appreciated in figures 3.12 and 3.13. In the parameter-matched and -mismatched set-ups 100 MHz CCC (figures 3.12c and 3.13c, respectively) experienced more peaks resulting from ML ECM, whereas the remaining three frequencies affected the CCC to a similar degree, both in parameter-matched case (figures 3.12a, 3.12b, and 3.12d), as well as -mismatched case (figures 3.13a, 3.13b, and 3.13d), which supports observation drawn from figure 3.11.

As seen in figures 3.12 and 3.13, the CCC traces are shifted towards positive time lag values, nonetheless, the maximum values of CCC still occurred for the time lag equal to zero. Additionally, in figure 3.12 one can appreciate significant side peaks in CCC contour plot of the 100 MHz message (figure 3.12c) in comparison to the remaining three frequencies. The most pronounced central peaks were recorded for rf level between

(a) Parameter-match set-up.

(b) Parameter-mismatch set-up.
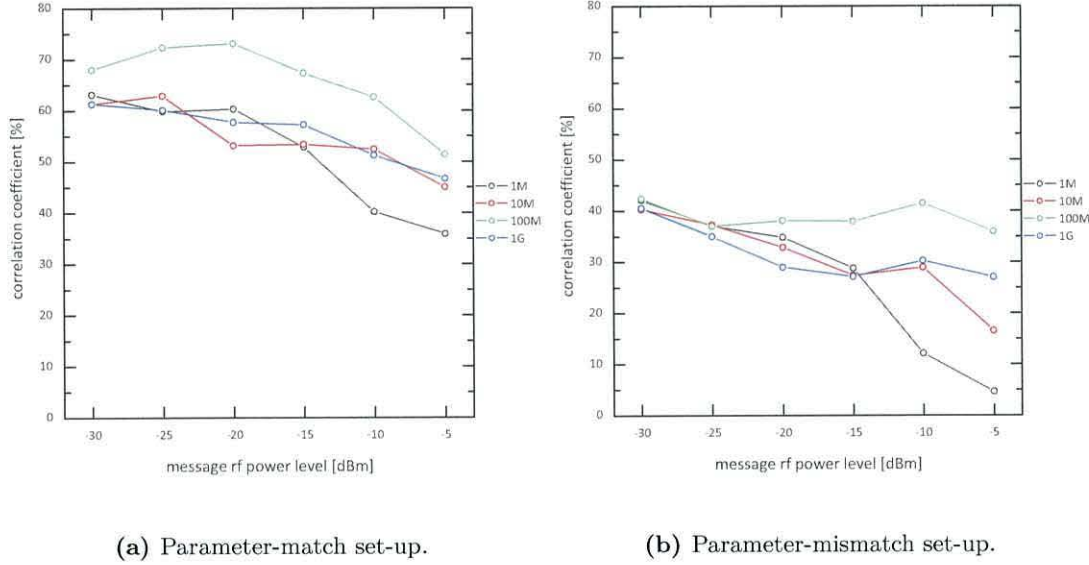
Figure 3.11: **Correlation coefficient for parameter matched and mismatched subexperiments** – Values of CC were calculated after the experiment.

−30 and −25 dBm and lag between −10 and zero nanoseconds, whereas, the most pronounced side peaks—for rf level of −20 dBm and for time lags between −40 and −30 ns and between 20 and 40 ns. Those side peaks in figure 3.12c (and to a lesser extent also those in figure 3.13c) could have been triggered by the applied rf message frequency of 100 MHz, although at this stage the significance of that particular frequency cannot be established.

Significant attenuation at high rf power levels is visible in figure 3.13a and can be linked to loss of synchronisation of 1 MHz message in figure 3.11b. Similar analogy can be drawn for 10 MHz message in figure 3.13b. This phenomenon alongside with the disappearance of the side-peaks with increasing rf power level in figures 3.12 and 3.13 can be explained on the grounds of switching the SL off by driving it repeatedly for relatively long periods (500 and 50 ns, respectively) of time below its threshold current, as indicated by table 3.3.

When interpreted from an eavesdropper's perspective, CCC plots suggest that

(a) 1 MHz.

(b) 10 MHz.

(c) 100 MHz.

(d) 1 GHz.
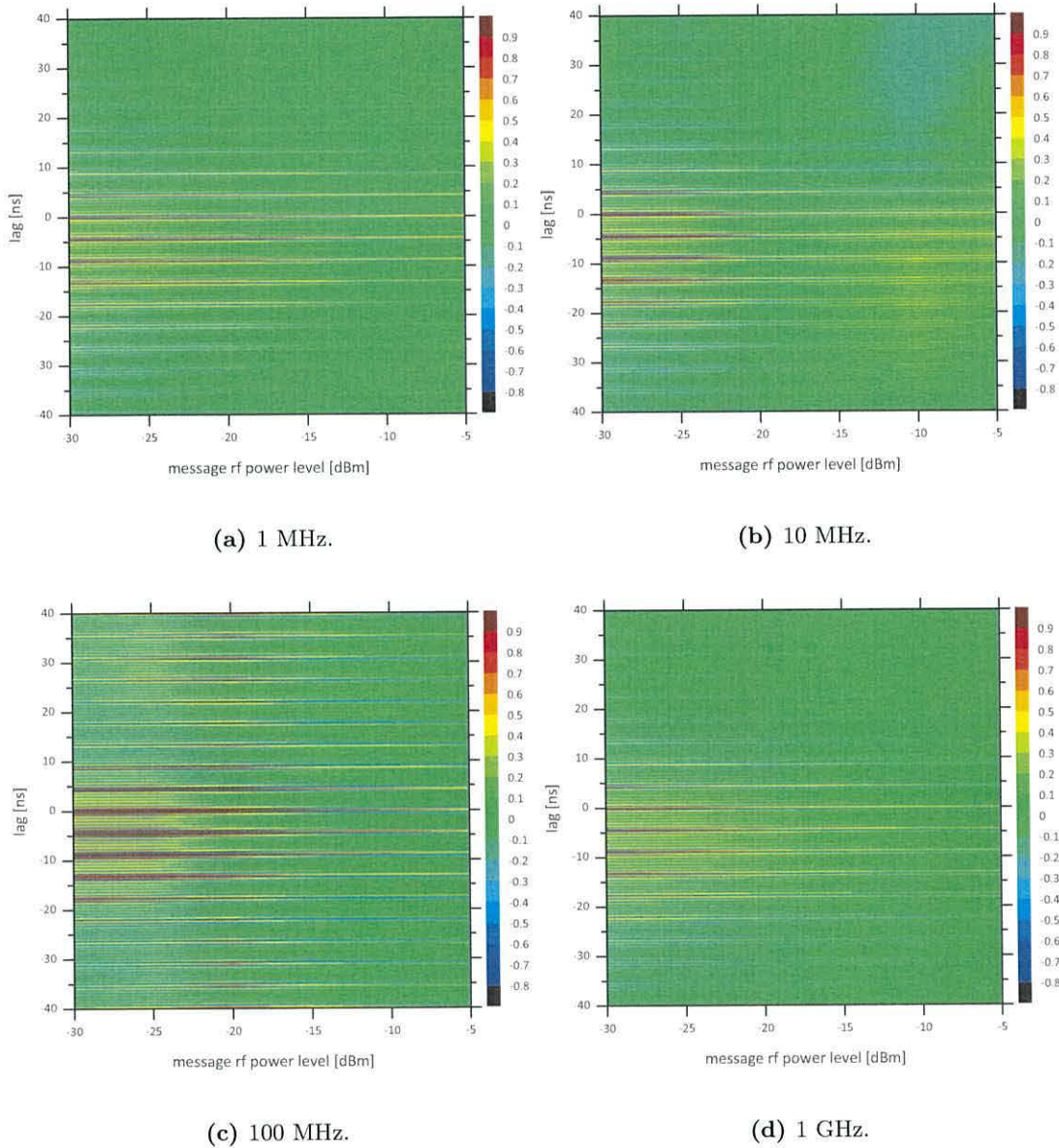
Figure 3.12: Contour plot of CCC for the parameter-match set-up – The colour scale denotes the magnitude of the CCC [a.u.].

(a) 1 MHz.

(b) 10 MHz.

(c) 100 MHz.

(d) 1 GHz.
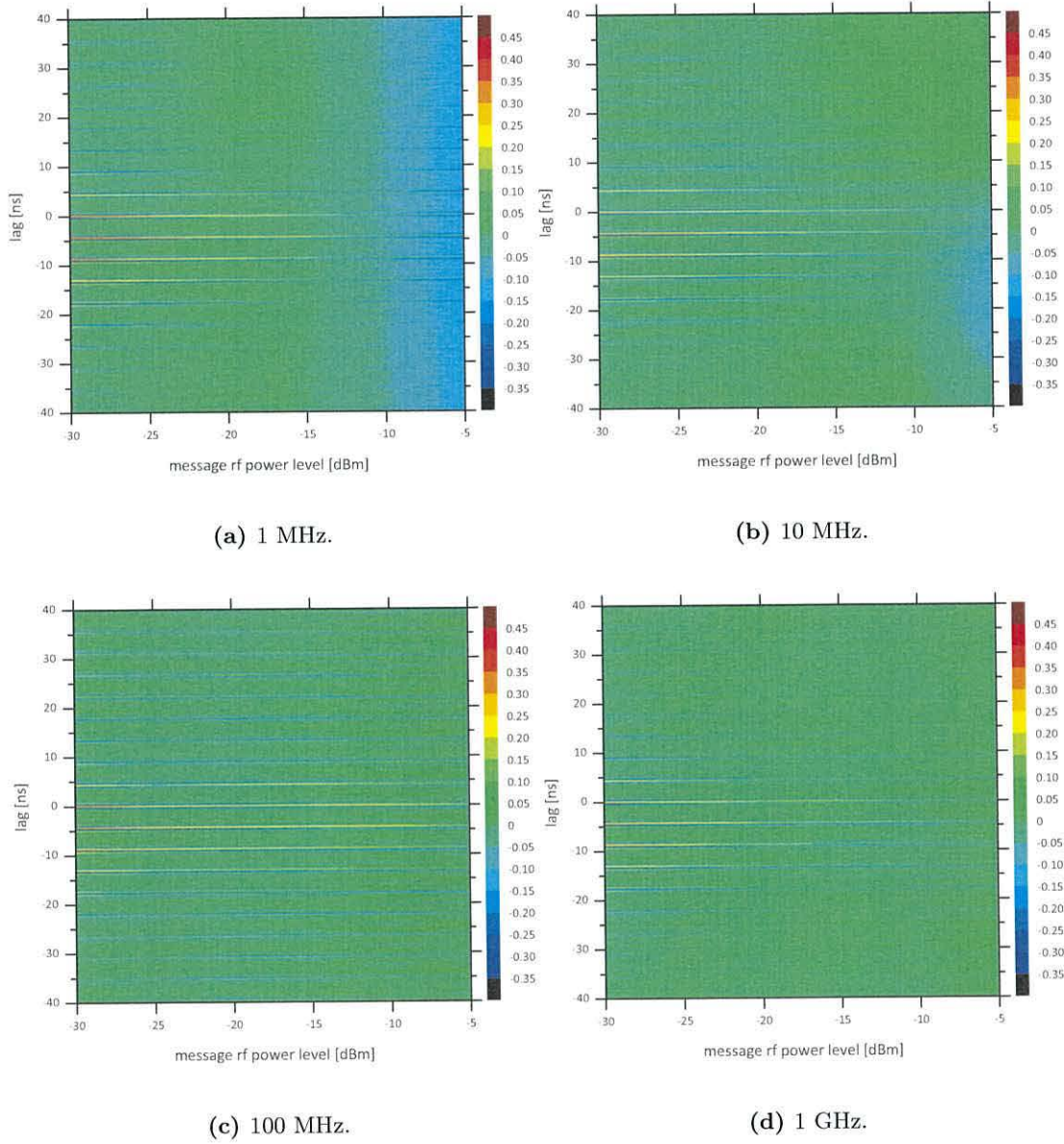
Figure 3.13: Contour plot of CCC for the parameter-mismatch set-up – The colour scale denotes the magnitude of the CCC [a.u.].

85

a potential attacker could still infer the length of ML's external-cavity through the analysis of CCC peaks (see equation (3.8)). All the features seen in figure 3.12 are still present in figure 3.13, albeit to a smaller degree owing to parameter mismatch and weaker synchronisation. Crucially, the side peaks of 100 MHz plot (figure 3.12c) can still be appreciated by an eavesdropper (figure 3.13c).

These figures could also be interpreted from the point of view of dynamic phenomena. Then figure 3.13 would serve as a testimony to the robustness of chaos synchronisation scheme; testimony that captured a snapshot of ML–SL dynamics at an intermediate point between two extremes of high-quality chaos synchronisation on one end and no synchronisation on the other.

Calculation of STF in figures 3.14 and 3.15 encompassed the division of the SL spectra with hidden message injected from ML by ML spectra *with* that message. On the other hand, calculation of STF in figures 3.16 and 3.17 involved division of SL spectra with the hidden message injected from ML by ML spectra *devoid of* that message. In other words, the former two figures represent dynamics of legitimate chaos synchronisation, whereas the latter two represent what an eavesdropper would perceive. This was done in order to investigate whether the hidden messages would become readily visible in STF plots. In contrast to FFT plots of ML or synchronised SL, the hidden message did not emerge clearly in the STFs.

It is speculated that multiple attenuation XCM peaks present in figures 3.14, 3.15, 3.16, and 3.17 could have originated in ML being rendered to operate below its threshold current a result of message's high rf power levels (especially -10 and -5 dBm) as presented in table 3.3. Modulation depth between -20 dBm and -10 dBm experienced the greatest amplification in figure 3.16c. The reason for that warrants further investigation.

Similarly to CCC plots discussed above, STF figures 3.14 and 3.15 allow an eavesdropper to draw certain conclusions regarding transmission. Firstly, an attacker could estimate the length of ML's external cavity through the analysis of spectral peaks (see

(a) 1 MHz.

(b) 10 MHz.

(c) 100 MHz.

(d) 1 GHz.
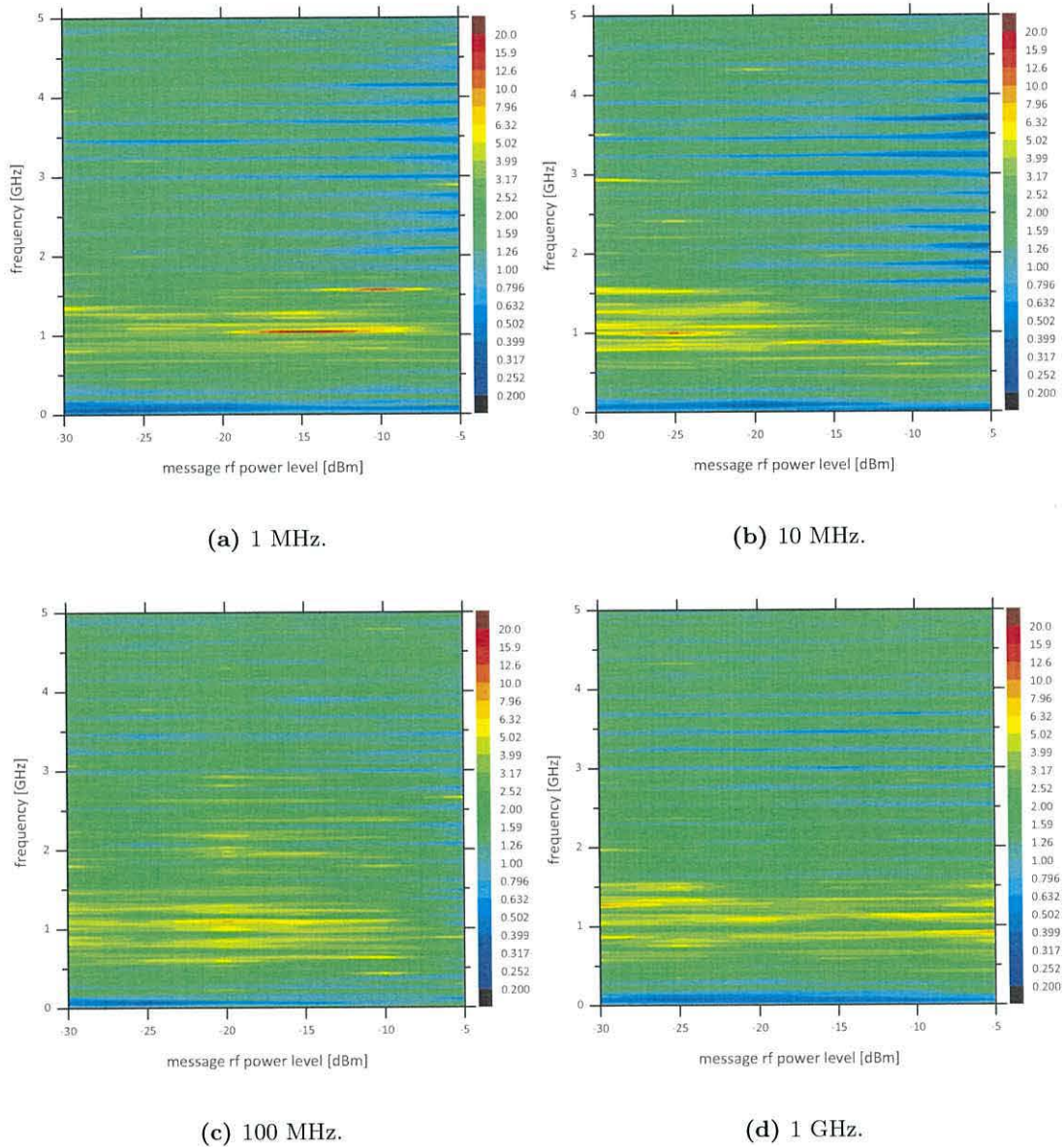
Figure 3.14: Contour plot of STF for the parameter-match set-up – The colour scale denotes the magnitude of the STF. Data were smoothed with 50-sample adjacent smoothing.

87

(a) 1 MHz.

(b) 10 MHz.

(c) 100 MHz.

(d) 1 GHz.
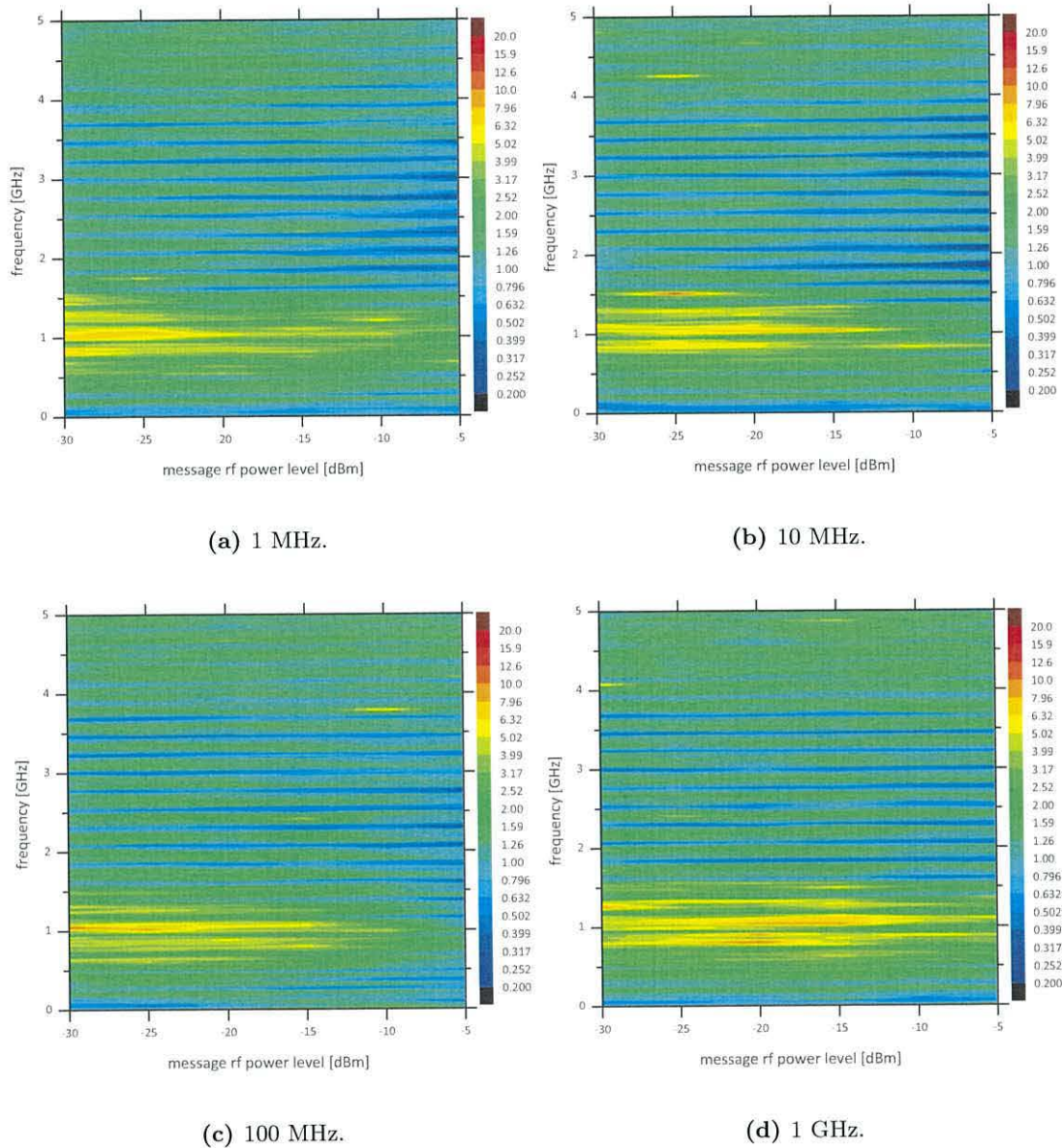
Figure 3.15: Contour plot of STF for the parameter-mismatch set-up – The colour scale denotes the magnitude of the STF. Data were smoothed with 50-sample adjacent smoothing.

(a) 1 MHz.

(b) 10 MHz.

(c) 100 MHz.

(d) 1 GHz.
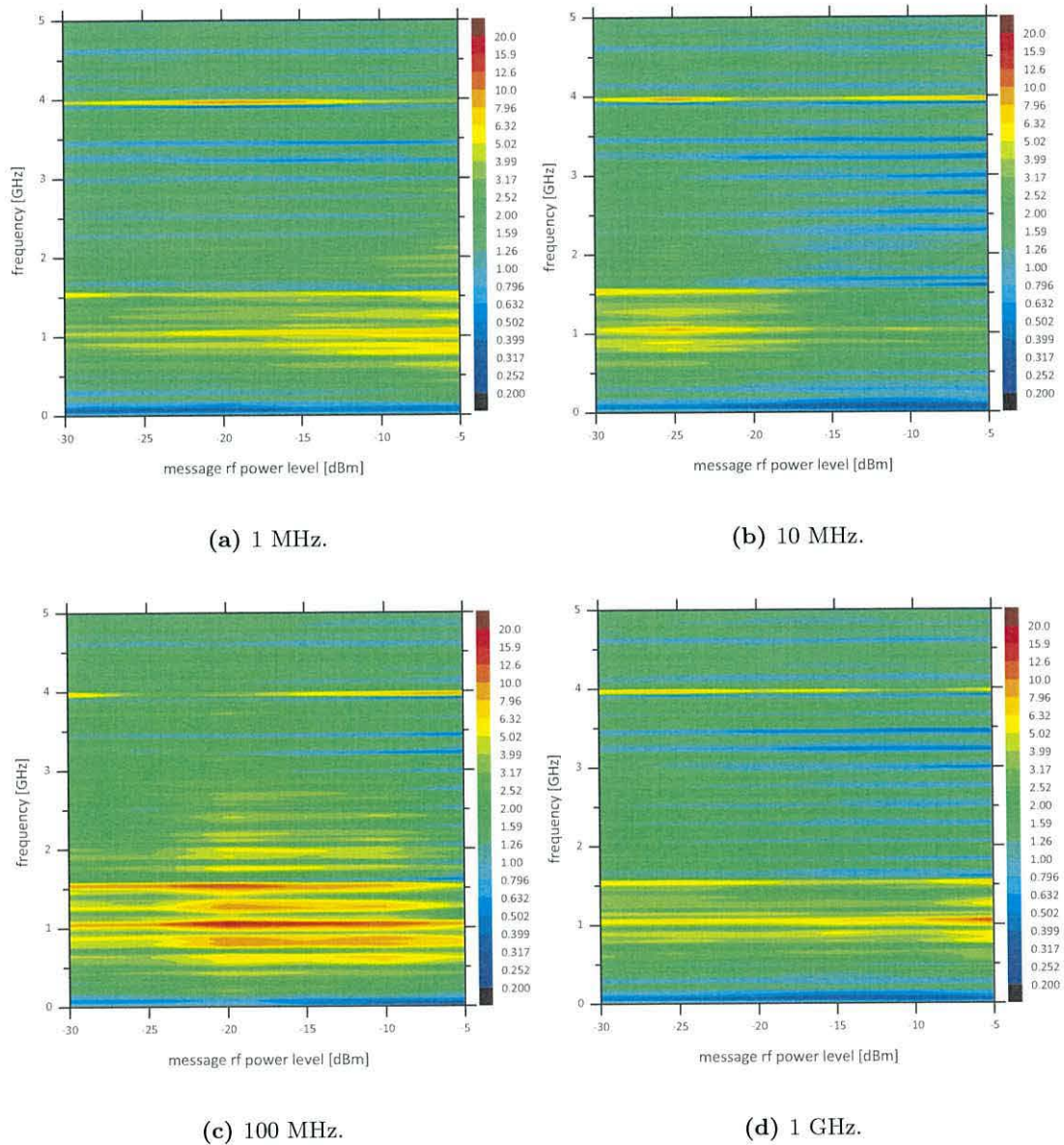
Figure 3.16: Contour plot of STF for the parameter-match set-up – ML no-modulation in denominator. The colour scale denotes the magnitude of the STF. Data were smoothed with 50-sample adjacent smoothing.

89

(a) 1 MHz.

(b) 10 MHz.

(c) 100 MHz.

(d) 1 GHz.
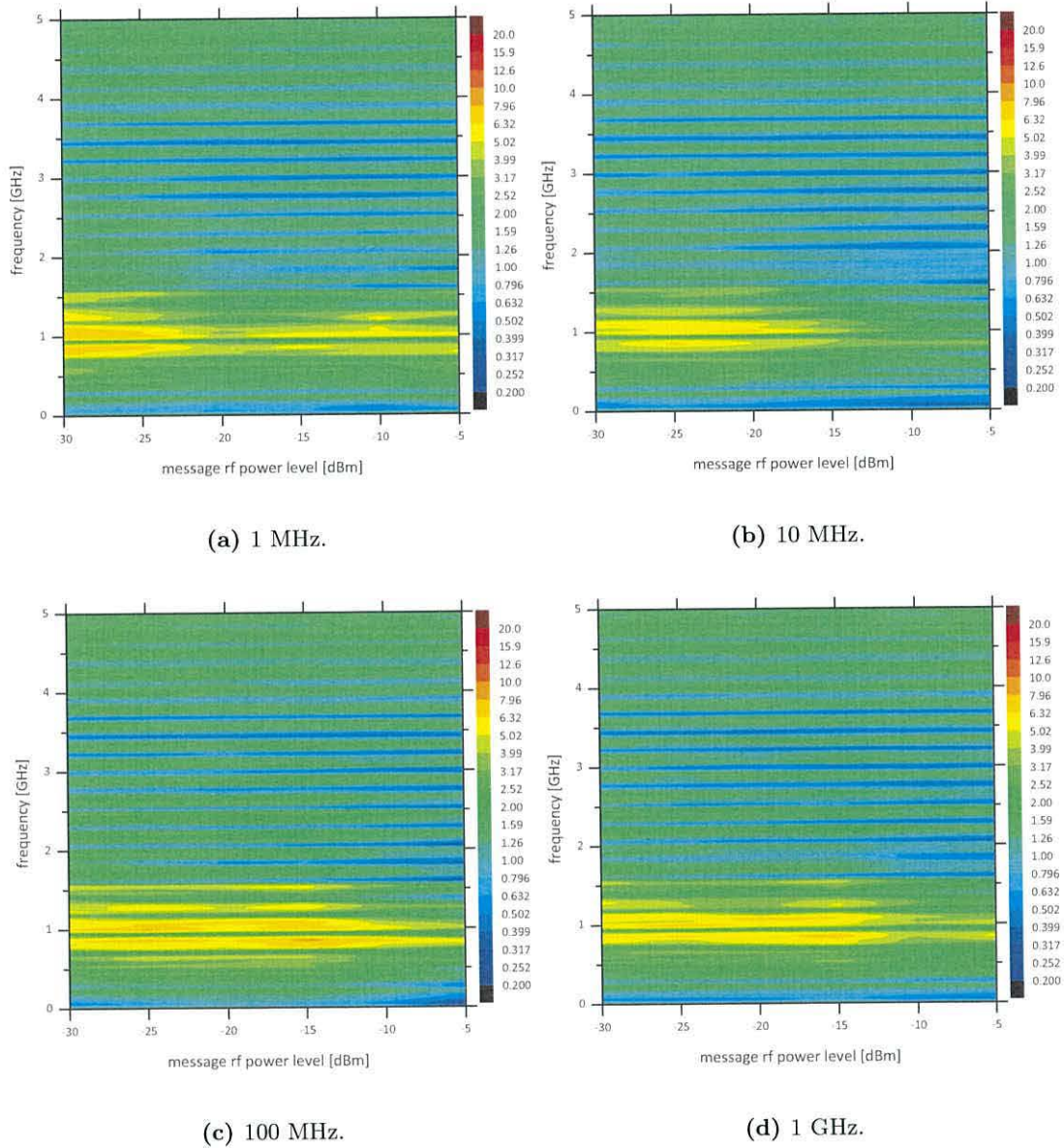
Figure 3.17: **Contour plot of STF for the parameter-mismatch set-up – ML** no-modulation in denominator. The colour scale denotes the magnitude of the STF. Data were smoothed with 50-sample adjacent smoothing.

equation (3.7)). Secondly, an estimate of the rf power level of the hidden message could be performed based on how much the frequencies around 1 GHz are amplified, as well as, on how much the frequency range 1.5–4 GHz experiences attenuation. Thirdly, one could also speculate on the frequency of hidden message, as the amplification region around 1 GHz displays less attenuation at high rf power for higher rf frequencies.

Emergence of attenuation peaks between 1.5 GHz and 4 GHz in figures 3.14a, 3.14b, 3.15a, and 3.15b can be tied back to figure 3.11 and explained as a result of driving SL below its threshold current.

It is conceivable that horizontal lines corresponding to 1.5 GHz and 4 GHz peaks present in figures 3.16 and 3.17 are nothing more than artifacts and stem from the fact that for all eight subfigures the same ML FFT spectrum was used. That single-trial spectrum did have larger than usual amplitudes of these two frequencies. They are therefore to be ignored.

Comparing figures 3.14 and 3.15 to figures 3.16 and 3.17 reveals that in the former case, low-frequency attenuation generally subsides for higher rf powers, whereas in the latter case, quite the contrary. Since the latter figures were prepared with fixed ML spectrum in the denominator, it would suggest that for higher rf powers SL was experiencing greater attenuation of low-frequency components. Finally, since the former figures experience decreasing attenuation for higher rf power, therefore it can be concluded that ML was experiencing even greater attenuation for the same frequency components.

3.3 Conclusions

Two experimental surveys were conducted—one focused on the effect of parameter deviation on chaos synchronisation quality, while the other on transmission of a message and its effect on synchronisation properties.

In section 3.1 the experimental procedure was introduced, as well as, the tools used to perform the calculations and obtain analytical results. The fluctuation found in CCC plots (see figures 3.5a and 3.5c) has been indirectly reported in the literature [220] as a fluctuation in optical power, although the CCC function used in Origin® may have made a small contribution to the undulations observed. Both sides of injection-locking diagram were investigated (see figures 3.5c and 3.5d) through temperature sweeps and were found to be symmetrical for the chosen parameter space. The experimental investigation and its results support the theoretical predictions found in the literature. The effect of parameter deviation was also presented in a form of STF (see figure 3.7) and a correspondence between correlation strength and amplification (or attenuation) of spectral components has been found. Poor synchronisation was accompanied by significant attenuation of low-frequency components or localised amplification in the high-frequency range, again in agreement with published work.

In section 3.2 the main focus was shifted towards transmission of a message and its impact on the dynamics and chaos synchronisation properties. Four different frequencies and six modulation depths were investigated. The process of extraction of the message was not performed due to conspicuousness of the masked messages in SL FFT spectra at all rf power levels. It was found, that for a message to remain hidden in CMO scheme, rf power levels below −25 dBm were required (see figure 3.9), which is lower than previously reported [83]. This difference is attributed to the lower dimensional chaos used, as the lasers were operating in the LFF regime. Laser synchronisation was also investigated under the condition of a large-amplitude signal modulation, which resulted in driving the ML below its threshold current. This regime is characterised by conspicuous time-domain waveform envelopes. The signal at 100 MHz had a much higher correlation coefficient than the other three frequencies (see figure 3.11), as well as, side peaks present in contour CCC plot (see figure 3.12). It is speculated at this point that an interplay between this frequency and the LFF might have taken place. It

was also discussed how much information an imperfectly-synchronised attacker could gain from eavesdropping on the communications channel without actually extracting the hidden message. It was found that the legitimate system's ML's external-cavity round-trip time could be easily deducted (through the CCC side peaks), and, with further analysis, also the modulation depth of the hidden message could be estimated. STF plots proved similarly useful in revealing the message.

Lastly, perfect synchronisation is not required if the system is operating in the LFF regime, as the message will be inherently insecure.

Chapter 4

Transient chaos synchronisation process—experimentally accessible parameters

The main motivation behind this chapter lies in the desire to investigate thoroughly the complex dynamics of an ECSLD and build upon the initial results obtained and presented in chapter 3. As a result, for the purpose of this study, a numerical model was written in Fortran to investigate the effect the parameters of the Lang–Kobayashi model have on lasers' dynamics. For a thorough description of the details of numerical computation employed throughout this thesis, see section 2.5.

Three aspects of dynamics of a ML–SL configuration employing optical injection and feedback were given consideration:

- various ramping durations of the optical injection (section 4.1);

- various maximum injection strengths (section 4.2);

- SL's injection-locked spectrum as a function of optical injection strength (section 4.3).

Respective sections contain a more detailed description of what actions were taken along with the results of said investigation.

Simulations performed throughout this thesis followed a standard approach found in the literature, whereby carrier diffusion is assumed to have negligible effect on lasers' dynamics. Nonetheless, numerical simulations of carrier dynamics where lateral carrier diffusion is taken into account were performed *e.g.* in [344], where large-scale stability was investigated, or [345], where a customised Lang–Kobayashi model was used, and it was found that carrier diffusion affects relaxation oscillation frequency.

Three straightforward concepts are used extensively throughout this and the next chapters, hence they will be introduced here, and they are as follows:

- power difference $P_s(t) - P_m(t)$ is defined and introduced here as a difference between SL and ML optical powers;

- phase difference $\varphi_s(t) - \varphi_m(t)$ is analogously defined as a difference between SL and ML optical phases;

- carrier transfer function $N_s(t)/N_m(t)$ is defined as a ratio of number of SL and ML carriers.

Except for different values of lasers' self-feedback ($\kappa_m = 10$ ns^{-1}, and $\kappa_s = 3$ ns^{-1}), the simulated lasers differed in no other aspect. Since optical injection increases the electric field inside an SLD's internal cavity, it depletes the carriers and yields an increased refractive index resulting in a decreased cavity resonance frequency [87, 88, 327]. Analogously to the point above, the approach employed in this thesis was a standard one[1], thus this effect was not compensated for.

---

[1]This approach recognises the fact that the above mentioned variables are by their nature coupled, and trying to untangle them would only introduce undue nonlinearities.

4.1 The effect of ramping at high optical injection rate

This subchapter investigates the effect the ramping function has on the SL's dynamics for a fixed value of κ_c^{max}. For the theoretical background see section 2.5. The numerical simulations were subdivided into the two following parts:

- section 4.1.1 deals with a number of ramping times ranging from 10 ns to 0.4 ps ($T_1 = 60$ ns; $T_3, T_4 \to +\infty$);

- section 4.1.2, on the other hand, revolves around one value of ramping time ($T_2 - T_1 = T_4 - T_3 = 50$ ns) simulated multiple times and subsequently averaged.

4.1.1 Sweep of short ramping time

The configuration employed in this section consists of a ML and SL in unidirectional closed-loop chaos-synchronisation configuration, as seen in figure 1.1b. The object of this study was the exploration of the influence of the duration of ramping time of a linear injection profile (as presented in figure 2.5) on the dynamics of SL.

Twenty-three simulations were run with identical values of initial conditions, and with ramping time duration assigned values between 10 ns and 0.4 ps. The former boundary was chosen as it was ten times greater than the usually assumed ramping time of one nanosecond. The latter boundary was chosen as a double of the simulation's iteration step of 0.2 picosecond. The maximum value of injection rate, $\kappa_c^{max} = 164$ ns^{-1}, would be reached after a respective ramping time. The carrier lifetime was set to $\tau_n = 1$ ns. All the other parameters' values can be found in table 2.1.

Figures 4.1a and 4.1b were obtained by calculating the difference between SL's and ML's optical phases. The contour plot in figure 4.2 was obtained by calculating the carrier transfer function for six[2] values of ramping time and aggregating the data.

---

[2]For the sake of greater readability.
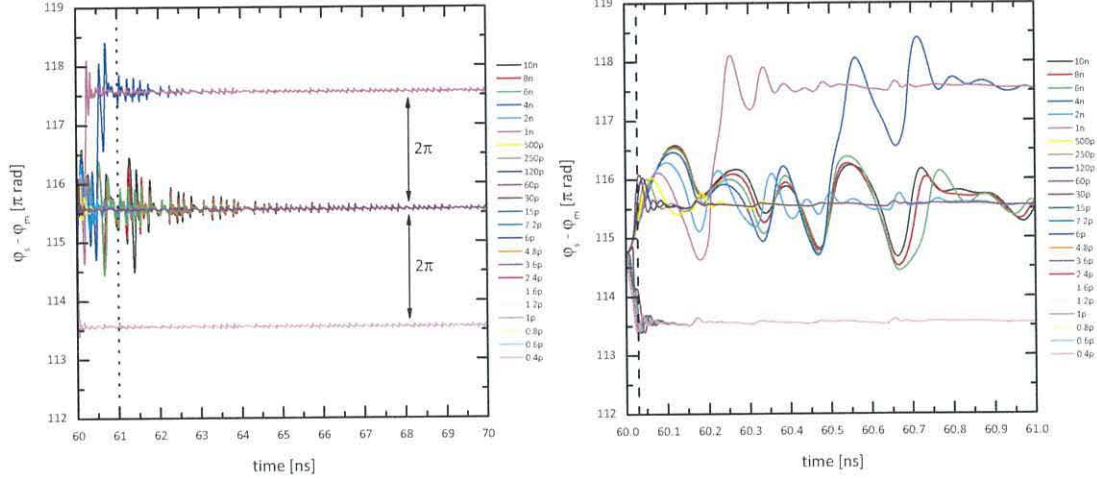
(a) 10 ns from the onset of injection.

(b) Transient dynamics to the left of the dotted line in figure 4.1b.

Figure 4.1: Phase difference between SL and ML on the rising slope of the ramping function – The legend corresponds to ramping times denoted in seconds. Optical injection from chaotic ML ($\kappa_m = 10$ ns^{-1}) into hitherto unsynchronised chaotic SL ($\kappa_s = 3$ ns^{-1}). Vertical dotted line in figure 4.1a denotes the one nanosecond time window used in figure 4.1b. Vertical dashed line in figure 4.1b denotes the shortest phase lock-on.

The shorter values of ramping time (between 0.4 ps and 30 ps) employed in the study experienced phase-lock at $\varphi_s - \varphi_m = 113.5\pi$ rad, as presented in figure 4.1a. The longer ones (between 60 ps and 10 ns), on the other hand, locked a full period later at 115.5π rad. However, two somewhat intermediate values (*i.e.* 1 ns and 4 ns) locked yet another full period later at 117.5π rad. While it is not surprising to see longer ramping times experiencing a phase-lock later, the reason for those two aforementioned cases to lock *two* full periods later is yet to be determined. Since each ramping time was simulated only once[3], it cannot be conclusively stated whether this artefact is to be ascribed to an underlying physical phenomenon, or to a rare, if not peculiar, happenstance. It is hypothesised, however, that this particular feature should be ascribed to the latter.

Longer values of ramping time experienced initial transients upon injection from

---

[3]When this survey was conducted the multiple-run averaging had not been implemented, yet.
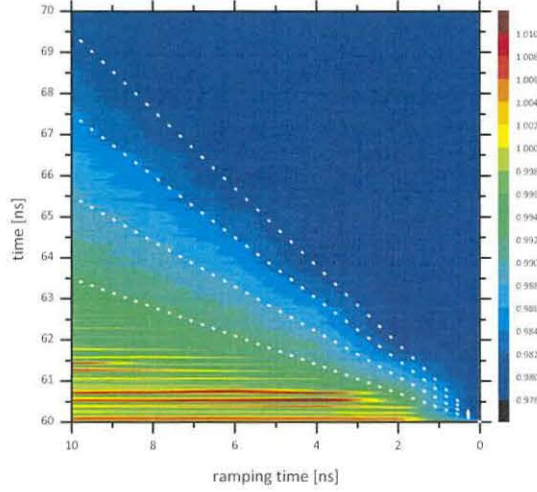
Figure 4.2: Carrier transfer function on the rising slope of the ramping function – Optical injection from chaotic ML ($\kappa_m = 10$ ns^{-1}) into hitherto unsynchronised chaotic SL ($\kappa_s = 3$ ns^{-1}). White dotted line were provided as a visual cue to allow for easier assessment of linearity of carrier transfer function. The 0.4 ps ramping time was rounded here to zero.

ML. One can also appreciate periodic perturbations seen in figure 4.1b. The shortest time between the onset of injection and a peak in optical phase difference amounted to *ca.* 27 ps and took place (unsurprisingly) for the shortest ramping time (*i.e.* 0.4 ps), as indicated by vertical dashed line in figure 4.1b. Since longer ramping times of 0.6, 0.8, and 1 ps saw an almost identical result it is therefore speculated the maximum frequency of a message to be hidden in optical phase (for the chosen parameter space) would be approximately equal to 37 GHz. Further extensive investigation would be required in order to establish the relationship between maximum frequency and system's parameters (*e.g.* carrier lifetime and linewidth enhancement factor).

For considerations regarding application of phase in chaos synchronisation schemes, see [170, 171, 346–356] and in particular [355] where the actual message was encoded with a frequency of 1 kHz over a carrier frequency of 100 MHz. A different approach was employed in [352], where a hidden message modulated (through a piezo element) the distance between ML and ML's ECM in a unidirectional closed-loop configuration.

The maximum bit rate of 100 Mbit/s was achieved with lasers' optical frequencies differing by no more than 1 GHz; this switching speed was shown to be limited by synchronisation transients.

The carrier transfer function for six values of ramping time is presented in figure 4.2. The four white dotted lines are included in the figure in order to highlight and provide a linear fulcrum. Judging by these lines, it can be said that carrier transfer function follows a linear profile closely, with perhaps one exception for ramping time duration of approximately 2 ns, where a slight nonlinearity can be seen. Since, as it was aforementioned, this survey only entailed one simulation per duration of ramping time, at this stage it cannot be conclusively stated what the cause of the nonlinearity is.

What can nonetheless be said is that in the injection-locked state the carrier transfer function retains a stable level, as signified by the uniformity of the shade of blue. Conversely, one can also appreciate transient instabilities between ramping times of 10 and 2 ns, as denoted by red and brown horizontal shades. These transients are akin to those in figure 4.1 that also finally subside.

4.1.2 Longer ramping time

Having briefly investigated the effect of short and extremely-short ramping times on SL's dynamics in section 4.1.1, this section will focus on multiple-run dynamics of SL subjected to a long rise- and fall-time of injection profile. A series of 10,240 simulations with random initial conditions were conducted with the aim to uncover the underlying mean profile (which is normally masked by high-amplitude chaotic oscillations).

Ramping time was set to 50 ns—five times longer than the longest duration of ramping time employed in the previous section. This duration could not have been chosen to be much longer than that due to memory limitations. Maximum injection rate was set to $\kappa_c^{max} = 160$ ns^{-1}. Transition times were chosen to be $T_1 = 30$, $T_2 = 80$, $T_3 = 140$, and $T_4 = 190$ ns. The orange trace in figure 4.3a of the SL's optical power

was calculated as arithmetical average of 10,240 simulation runs with random initial conditions, whereas the black trace denotes a single simulation. The SL's carrier transfer function in figure 4.3b was prepared analogously. Figure 4.3c of phase difference was prepared in a similar manner, however, for the purpose of greater readability only the mean trace of phase difference is plotted. In all the figures, the red dashed line is provided as a visual cue and presents the ramping profile used in the simulations.

In the switch-on stage ($t \in [0, 30]$ ns) in figure 4.3a, the single-run black trace displays signs of initial, yet diminishing, oscillation; the average orange trace, on the other hand, suggests that a form of a limited resonance builds up. The rising slope ($t \in [30, 80]$ ns) brings about tightening of the range of values of the orange trace (hence suggesting an increased randomness pool) accompanied by conspicuous high-amplitude transients of the black trace induced by varying the value of optical injection. During the stable-lock stage ($t \in [80, 140]$ ns), average power difference retained a very stable level confined to narrow range of values. The falling slope ($t \in [140, 190]$ ns) mirrors the pattern seen on the rising slope. In the final stage ($t \in [190, 220]$ ns), the mean trace averages to an almost flat line, however, the envelope of the black trace displays signs of diminishing oscillation—the sheer presence and, if so, the shape of this feature are very sensitive to initial conditions and the shape of injection profile.

On the rising- and falling-slopes high-amplitude transients can be seen in SL's optical power time-domain trace in figure 4.3a. In figure 4.3b one can easily spot the following characteristic features:

- the initial dip representing the transition in SL's dynamics between being subjected only to its own ECM ($\kappa_s = 3$ ns^{-1}) and being subjected to external injection;

- semi-exponential follow-up leading later to linear-like response for greater values of injection ($\kappa_c \geq 40$ ns^{-1}).

On the rising slope, the initial gradient decreased and gave way to the second one
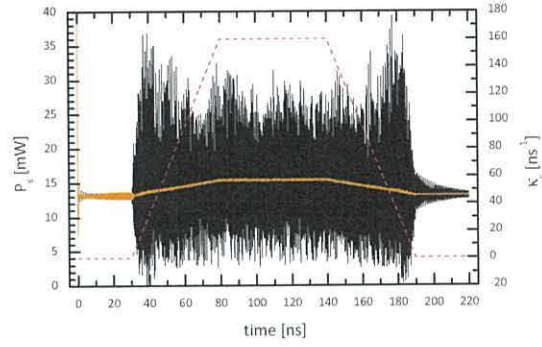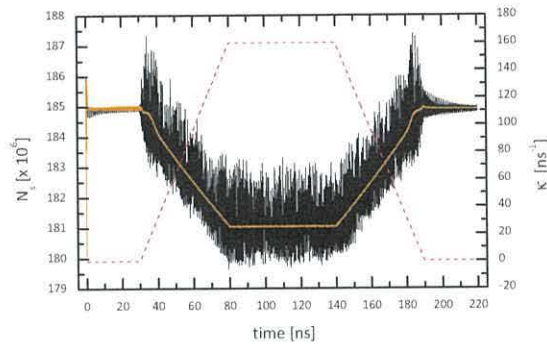
(a) SL optical power.

(b) SL carriers.
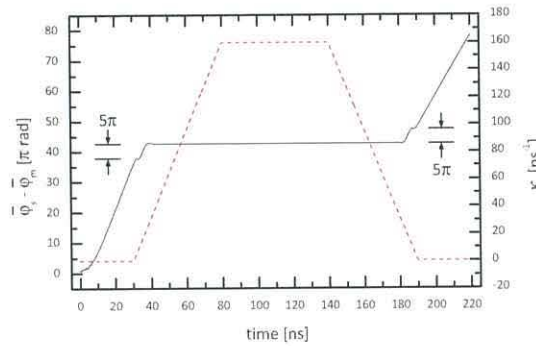
(c) Average phase difference.

Figure 4.3: ML and SL optical power, carriers, and average phase for 50 ns ramping function – Orange trace corresponds to 10,240 simulations performed with random initial conditions and subsequently averaged. The carrier lifetime was fixed at $\tau_n = 3$ ns. Red dashed line signifies the trace of ramping function.

after a period of *ca.* 10 ns. This behaviour was mirrored on the falling slope.

Approximately two nanoseconds after the injection started ($\kappa_c \approx 3$ ns^{-1}) the average phase difference (figure 4.3c) experienced its local maximum. At that point the average SL carriers (figure 4.3b) also exhibited a dip. Then, after another 0.8 ns ($\kappa_c \approx 8.9$ ns^{-1}) the phase difference reached its local minimum. During that short period of time, the SL appears to have reach an inflexion point, where for an instant a phase-lock was obtained only to be soon lost owing to increasing κ_c. The second local maximum was reached almost 9 ns ($\kappa_c \approx 29$ ns^{-1}) after the injection began (and approximately 5π rad from the first maximum). Finally, the phase difference levelled after another 3 ns ($\kappa_c \approx 39$ ns^{-1}), almost 12 ns after the injection began. This pattern was repeated on the falling slope of ramping function, as well.

Since this trace was so heavily averaged and since chaos is very sensitive to minuscule differences in parameters' values, one can assume that any non-recurring artefact would be blurred beyond recognition. The phase double-dip, however, not only is clearly defined, but is also symmetrical. This feature was also found for ramping time of 10 ns at variable injection, in sections 4.2.2 and 4.2.3.

Building upon the results in the previous section, as well as, these presented here, the carrier double-gradient feature does not appear to be sensitive to the *gradient* of injection, but rather to absolute value of κ_c. Hence, it is postulated that slow injection will not mitigate the phenomenon.

4.2 The effect of injection strength on dynamics

While the previous subchapter was focused on the dynamic effects in SL subjected to high optical injection with variable ramping time, this subchapter, in contrast, takes the opposite approach by keeping the ramping time fixed and varying the injection strength. The scope and extent can be most succinctly summarised as:

- section 4.2.1 investigates the effect the injection strength has on chaotic SL;

- section 4.2.2 contains a survey of lasers' dynamics when subjected to relatively low values of injection after averaging;

- section 4.2.3, similarly to the one above, is also focused on average dynamics, however, for high values of optical injection.

4.2.1 Sweep of injection strength

Injection values ranged from $\kappa_c^{max} = 3$ to 80 ns^{-1}. The transition times were chosen to be $T_1 = 60$, $T_2 = 70$, $T_3 = 140$, and $T_4 = 150$ ns thereby making the ramping time equal to 10 ns. One simulation was run for every injection strength. All 24 simulations shared the same initial conditions. The only parameter changed throughout this survey was κ_c^{max}.

SL's optical power traces were aggregated in a contour plot and are presented in figure 4.4. Figures 4.4a and 4.4c were prepared for $\tau_n = 2$ ns, whereas figures 4.4b and 4.4d for $\tau_n = 3$ ns. The ragged profile seen in figure 4.4 is to be attributed to transient spikes. No multiple-run averaging was performed, however, adjacent-averaging covering 20,000 samples was employed. Also, in black are overlaid the dashed-dotted contour lines denoting a given value of injection strength, expressed in ns^{-1}. These are included and meant as a visual cue. Figure 4.5 was obtained by plotting all the 24 traces of phase difference over the rising slope.

As expected, power levels in figure 4.4 were affected via the first two components on the right-hand side of equation (2.102)—carrier recombination ($\propto \frac{1}{\tau_n}$), as well as, through carrier injection's dependence on carrier lifetime ($J \propto I_{th} \propto \frac{1}{\tau_n}$) through threshold current, as defined in equations (2.104) and (2.105). These two factors resulted in bringing SL's optical power level from approximately 19.4 mW for $\tau_n = 2$ ns down to 13.1 mW for $\tau_n = 3$ ns outside of the injection window, and from 21.4 mW

to 14.5 mW inside, respectively. The colour-scale levels mostly lie within the supplied injection-strength contour lines; those levels are better confined for the case of $\tau_n = 2$ ns rather than 3 ns. In general, figure 4.4 indicates that SL's power follows the injection profile approximately linearly.

Four traces of SL's optical power ($\kappa_c^{max} = 10$, 36, 50, and 80 ns^{-1}) oscillated at a lower post-injection value (see black traces in figure 4.4b). Bearing in mind that each κ_c^{max} value was simulated once, this feature is most likely to have resulted from unique combination of parameters' values and as such will not be interpreted here as a reproducible phenomenon. The results indicate that higher values of τ_n are more likely to induce post-injection oscillations in SL's dynamics.

The most striking characteristic of the average phase-difference in figure 4.5 is the step-like nature of the $\tau_n = 2$ ns traces, compared to conspicuously smooth nature of the traces corresponding to $\tau_n = 3$ ns. Since the value of carrier lifetime was the only parameter that differed between the two surveys, it is concluded that this unexpected nature of phase difference is to be ascribed to carrier lifetime.

Three regions of injection have been observed in figure 4.5:

- semi-solitary for $\kappa_c^{max} \in [\,3,\,10\,]$ ns^{-1}, where SL exhibits perturbations mainly due to its ECM, rather than injection from ML;

- intermediate region for $\kappa_c^{max} \in [\,10,\,30\,]$ ns^{-1}, where rapid and erratic processes of locking in and out occur;

- stable locking for $\kappa_c^{max} \in [\,30,\,80\,]$ ns^{-1}, with linear dependence of SL's power on injection rate.

The boundaries between the above mentioned regions are included in figure 4.4 in the form of white vertical dashed lines. Due to discretisation of κ_c^{max} scale, this division should not be treated literally, but rather as an approximation. Nonetheless, under the conditions assumed, injection level of *ca.* 30 ns^{-1} was found to be sufficient to guarantee
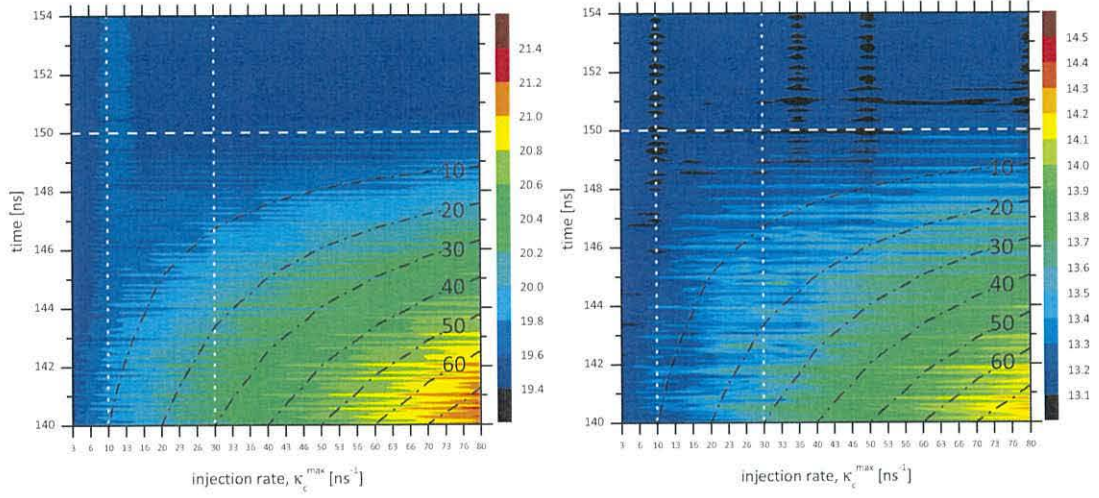
(a) Falling slope of ramping function, $\tau_n = 2$ ns.

(b) Falling slope of ramping function, $\tau_n = 3$ ns.
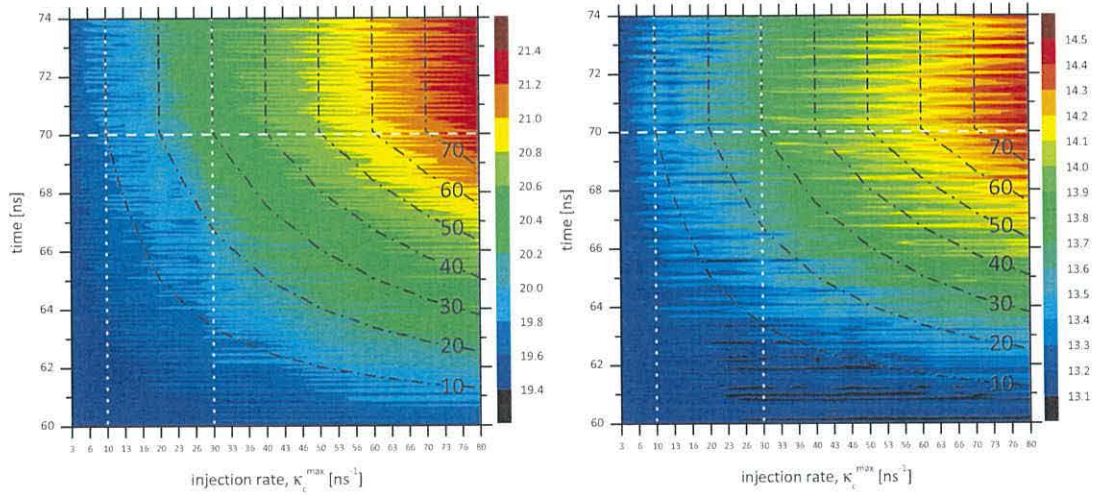
(c) Rising slope of ramping function, $\tau_n = 2$ ns.

(d) Rising slope of ramping function, $\tau_n = 3$ ns.

Figure 4.4: SL optical power as a function of injection strength for two values of carrier lifetime – Colour scale denotes optical power in milliwatts. 20,000 samples adjacent averaging was performed on each of the 24 traces. White dashed horizontal line denotes the moment when the injection reached zero (for falling slope, figures 4.4a and 4.4b), or κ_c^{max} (for rising slope, figures 4.4c and 4.4d). White dashed vertical lines separate three regions of SL's dynamics. Black dashed-dotted lines have been overlaid and denote the boundaries of the injection crossing given injection strength denoted in ns^{-1}.

105

(a) $\tau_n = 2$ ns.   (b) $\tau_n = 3$ ns.
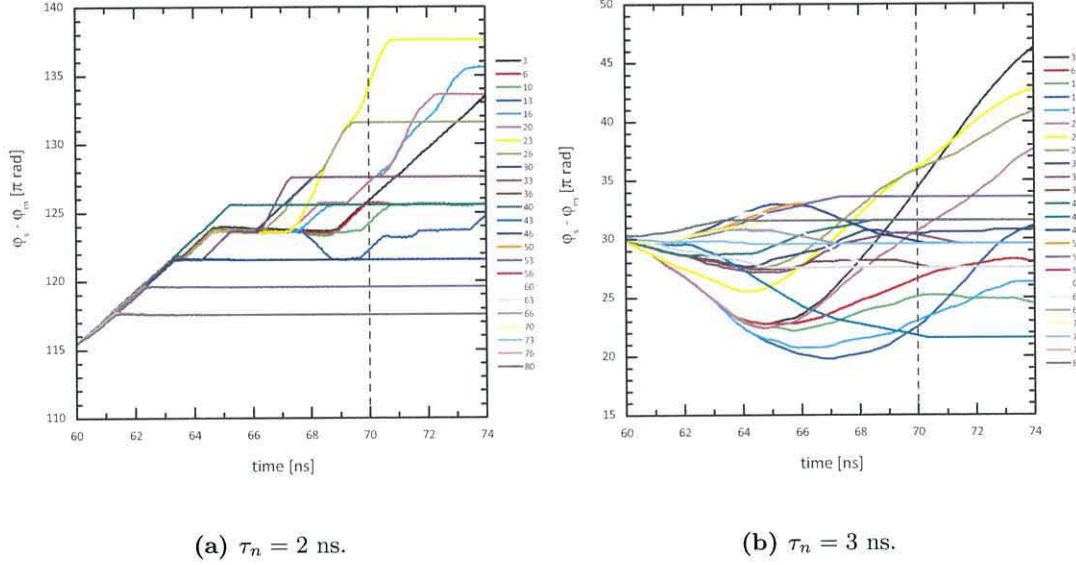
Figure 4.5: Optical phase difference on the rising slope of ramping function – 20,000 samples adjacent averaging was performed on each of the 24 traces. The legend corresponds to injection strength denoted in ns^{-1}. Black vertical dashed line denotes the moment when injection reached κ_c^{max}. These lines are equivalent to white horizontal dashed lines in figures 4.4c and 4.4d.

stable locking. Phase difference was more stable in case of shorter τ_n (staircase-like, with the offset dependent on injection rate), whereas for longer τ_n it presented itself in a more unpredictable way without any obvious pattern (with phase-lock offset assuming random values). Moreover, on the rising slope, the phase difference assumed predominantly positive inclination for $\tau_n = 2$ ns (figure 4.5a), whereas for $\tau_n = 3$ ns (figure 4.5b) it developed a clearly negative dip from which it recovered after a few nanoseconds. Three traces are not phase-locked at $t = 74$ ns in figure 4.5a in contrast to eight in figure 4.5b, hence the carrier lifetime can be said to have a direct impact on probability of phase locking, and specifically, the longer the carrier lifetime, the more unstable is the phase difference.

4.2.2 Sweep of small injection strength

Having conducted in the previous section a broad-scope, yet unaveraged, survey of SL's dynamics subject to various levels of optical injection, this section will focus instead on just a handful of chosen values of κ_c^{max}, with particular interest in traces of averaged dynamics. Four injection strengths were chosen: 20, 30, 40, and 50 ns^{-1}; each κ_c^{max} level was simulated 10,240 times with random initial conditions. The carrier lifetime was set at 3 ns. The same temporal coordinates were used as in the previous section.

Figure 4.6 was prepared by plotting the difference of optical powers (figure 4.6a), optical phases (figure 4.6b), as well as, the ratio of average carriers (figure 4.6c). The injection window is presented along with visual cues representing:

- the rising slope of ramping function—between points T_1 and T_2 denoted by vertical dashed and dotted lines, respectively;

- the constant, maximum injection—between points T_2 and T_3 denoted by vertical dotted lines;

- the falling slope of ramping function—between points T_3 and T_4 denoted by vertical dotted and dashed lines, respectively.

The pre- and post-injection range of values in figure 4.6a is dramatically different for all four traces—with the post-injection window being stabilised by the external injection. Nonetheless, optical powers difference unsurprisingly retains the same mean value of approximately -0.1 mW on either side of injection window. The range of values within the injection window is dependent upon the injection level—the higher the κ_c^{max}, the smaller the range.

In general, the average phase difference in figure 4.6b is characterised by three different gradients over these three temporal windows:

- the pre-injection window for $t \in [0, 60]$ ns;
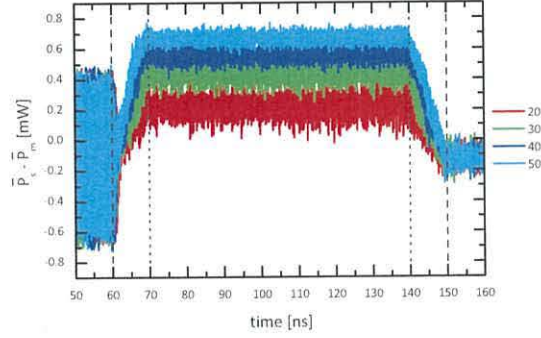
(a) Difference of average optical powers.
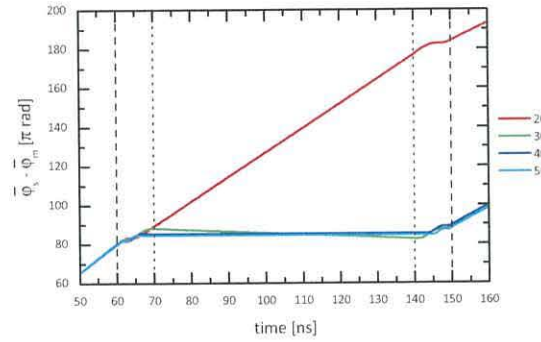
(b) Difference of average optical phases.
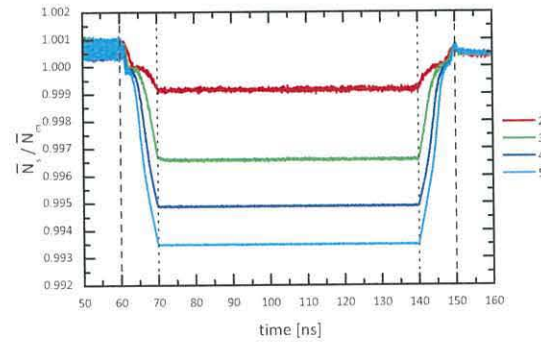
(c) Ratio of average carriers.

Figure 4.6: **Optical power and phase difference, and carrier ratio for small injection strength** – 10,240 simulations were performed with random initial conditions and averaged for each of the four values of injection strength. The legend corresponds to κ_c^{max} values expressed in ns^{-1}.

- the full injection window for $t \in [70, 140]$ ns;

- the post-injection window for $t \in [150, 220]$ ns.

The trace of $\kappa_c^{max} = 20$ ns^{-1} over the full injection window would suggest that, on average (and for the chosen parameter-space), this amount of optical injection is insufficient to facilitate a phase-lock, hence the oblique line in the full injection window. Nonetheless, the features visible in windows corresponding to rising- ($t \in [60, 70]$ ns) and falling-slopes ($t \in [140, 150]$ ns) were found to be present irrespective of the value of κ_c^{max}. The other three traces exhibited a phase-lock over the injection window.

The most significant transition occurred between κ_c^{max} values of 20 ns^{-1} and 30 ns^{-1}, similarly to section 4.2.1, where $\kappa_c^{max} = 30$ ns^{-1} was found to be an approximate boundary between semi-stable and stable regimes.

The carrier ratio in figure 4.6c displays the pattern already seen in figure 4.6a, where increasing κ_c^{max} decreased the range of values, which is not surprising, since increasing the optical injection increases the number of photons in laser's cavity, which then translates into greater suppression of carriers.

In the case of $\kappa_c^{max} = 20$ ns^{-1} SL's average carriers displayed signs of a nonlinear response to the linear ramping function—more like an exponential, followed by a plateau, followed by exponential. However, in case of $\kappa_c^{max} = 40$ ns^{-1} and especially 50 ns^{-1}, the feature was stretched thereby linearising what previously resembled an exponential trace. Similarly to optical power differences seen in figure 4.6a, here, the pre-injection range of values is greater than post-injection level. SL's dynamics are stabilised by the brief moment of external injection. Also, note the nonlinear vertical spacing between the traces over the injection window.

4.2.3   Sweep of high injection strength

In a similar vein to the investigation performed in the previous section, this one will focus on the same principles, but for a different range of κ_c^{max} values. Here, the injection strength will be higher than that considered in previous simulations. Specifically, five injection strengths were chosen: 80, 100, 120, 140, and 160 ns^{-1}; each κ_c^{max} level was simulated 10,240 times with random initial conditions. Carrier lifetime was set at 3 ns and the same temporal coordinates were used as in the previous two sections. Figure 4.7 was prepared analogously to figure 4.6.

The average optical power difference in figure 4.7a either side of injection window (*i.e.* between 50 and 60 ns, as well as, between 150 and 160 ns) retained approximately the same average value and range of values, in contrast to figure 4.6a. Two-gradient slopes can also be appreciated in that figure (whereas in figure 4.6a this feature is arguably non-existent, or at least inconspicuous). The slope itself is super-linear and the temporal occurrence of the 'kink' appears to be dependent on the injection strength, *i.e.* the stronger the injection, the sooner the 'kink' appears. Not only is the temporal dependence evident, but also the actual value of power difference is affected in a similar manner, *i.e.* the stronger the injection, the greater the value of power difference at which the 'kink' appears. This feature is also not exactly symmetric—on the rising slope, the value of power difference for a 'kink' is higher than on the falling slope.

All the traces in figure 4.7b exhibited a stable phase-lock with the same double-dip features as seen in figure 4.6b. These traces would suggest that in spite of very strong injection, the average phase difference displays a certain jitter, which is to be ascribed to the effect of random initial conditions which do affect the exact time when the two lasers synchronise, hence a non-zero offset between the traces.

The two-gradient feature can also be found in figure 4.7c, albeit in this case, the traces are much smoother than those in figure 4.6c. What is significant, however, is that another feature of optical injection was exposed *specifically* owing to that smoothness.
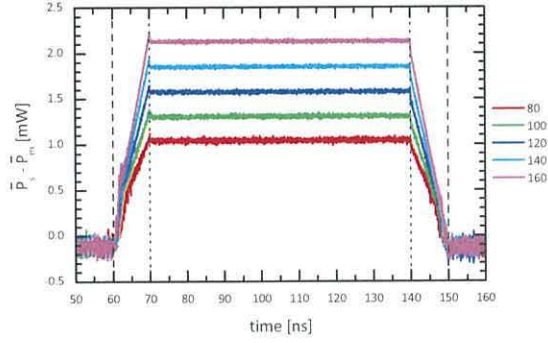
(a) Difference of average optical powers.
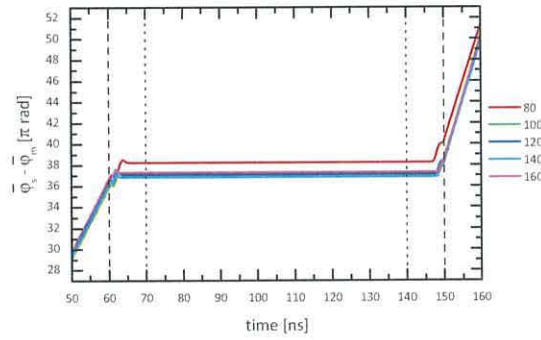
(b) Difference of average optical phases.
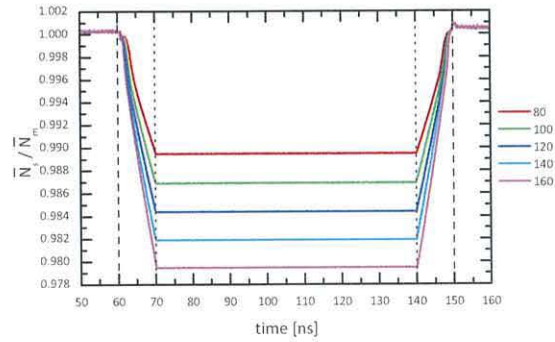
(c) Ratio of average carriers.

Figure 4.7: Optical power and phase difference, and carrier ratio for high injection strength – 10,240 simulations were performed with random initial conditions and averaged for each of the four values of injection strength. The legend corresponds to κ_c^{max} values expressed in ns^{-1}.

111

On the rising slope of ramping function a little negative dip is clearly visible. Later, it is followed by the aforementioned two-gradient slope. On the falling slope the same feature is visible, as well, although it bears a non-symmetric feature of a negative dip followed immediately by a positive one. The temporal position of the negative dips is dependent upon the value of injection strength as is its depth, however, to a smaller degree. Conversely, the positive dip appears to be independent. It is speculated that the positive dip is a result of a lower number of photons in the cavity, which is compensated by the delayed field circulating in the laser's external cavity.

Lastly, the vertical spacing between the traces is much more uniform in figure 4.7c, than it was in figure 4.6c. Further deliberations on such nonlinearities, *e.g.* when SL is subjected to various levels of modulation depth, can be found in [321].

4.3 Spectrum of locked SL as a function of injection

Finally, building upon SL's dynamics investigated in detail in previous sections, this section's focus will lie on the spectral properties of SL subjected to various levels of optical injection. Four values of injection strength ($\kappa_c^{max} = 40$, 80, 120, and 160 ns^{-1}) were chosen to be representative of the investigations performed in sections 4.2.2 and 4.2.3. Furthermore, figure 4.8 was prepared by aggregating respective spectral traces collected while performing surveys in those two sections. Each value of κ_c^{max} was averaged over 10,240 simulations which were run with random initial conditions. Carrier lifetime, as in previous sections, was equal to 3 ns.

The SL's spectrum in figure 4.8a displays strong signs of a second resonance peak's sensitivity to optical injection—not only does the second peak shift towards higher frequencies with increasing κ_c^{max}, but also the relative height of the peak decreases, *i.e.* increasing the injection strength suppresses the SL's plateau. This phenomenon could be explained on the grounds of SL's complex field equation becoming dominated by the

(a) Average SL spectrum.

(b) Average STF.
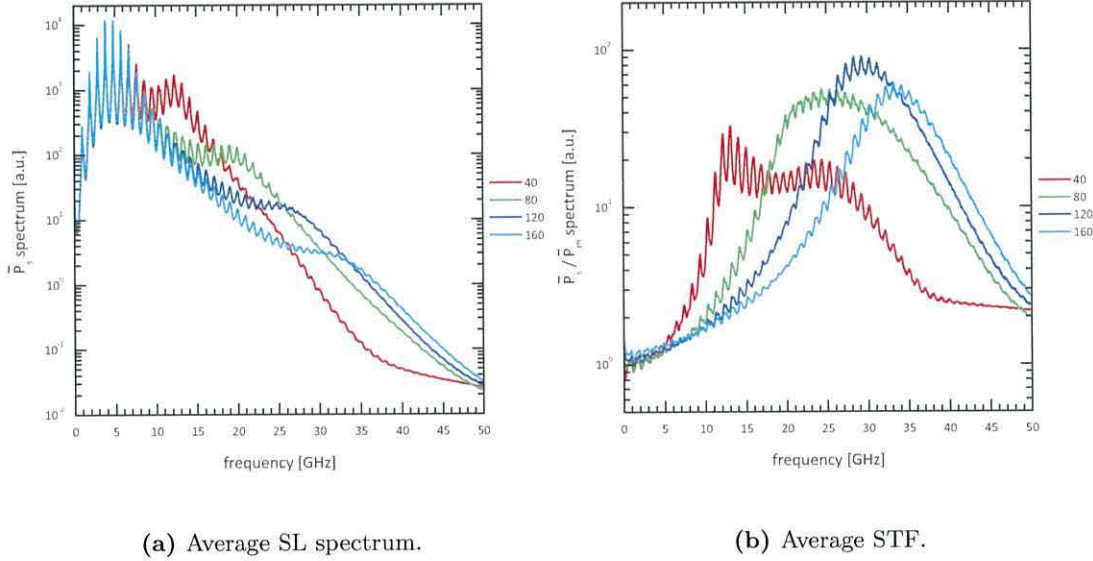
Figure 4.8: SL spectrum and STF for four values of injection strength – The legend corresponds to κ_c^{max} values expressed in ns^{-1}.

external injection component rather than SL inherent gain component.

Spectrum transfer function in figure 4.8b lends even more evidence with respect to the resonance peak shift as a function of κ_c^{max}. The 40 ns^{-1} trace clearly displays two distinct peaks, the second of which is no longer present for higher values of injection strength. The first peak is shifted towards higher frequencies, and its maximum value was found to be equal to 89.8 for $\kappa_c^{max} = 120$ ns^{-1} at the frequency of 29.3 GHz.

What this signifies is the fact that even above the injection strength of 30 ns^{-1} (see the red trace in figure 4.8b), which has been identified as a lower boundary of stable locking, the SL exhibits a secondary resonance peak in its spectrum. This peak diminishes with increasing injection; it is gone at the levels of injection above 60 ns^{-1}.

4.4 Conclusions

In section 4.1.1 twenty-three single-run simulations were performed to investigate SL's dynamics when subjected to various ramping time durations. Ramping times of 60 ps

and longer induced transient fluctuations in the phase locking. These phase transients at times reached amplitude of almost 2π rad, however, they also settled after half the duration of the given ramping time (at which point half the value of κ_c^{max}, *i.e.* 82 ns^{-1}, was reached). The shortest phase-lock was achieved 27 ps after the injection had begun, thereby translating into 37 GHz of message bandwidth should one choose to use the phase as the carrier; the value obtained is much higher than that of 1 GHz found in published material. The carrier transfer function revealed a mostly linear carrier dependence on injection profile. Nonetheless, initial perturbations seen for longer ramping times, as well as, nonlinear dependence for ramping times of the order of carrier lifetime prompted a more thorough investigation in the next section, 4.1.2, where an underlying mean profile was discovered through averaging of multiple simulations run with random initial conditions. A double-gradient profile was seen here in the mean trace of SL carriers. Moreover, a double-dip was found in the plot of average phase difference. The minima and gradients observed in the carrier transfer function, as well as, in the average phase difference traces are features of underlying physical dynamics normally obscured by high-amplitude oscillations. Further observations of this feature in the carrier transfer function are presented in chapter 5.

In section 4.2.1 the effect of injection strength was investigated for two values of carrier lifetime. The SL optical power figures showed a more ragged profile when the carrier lifetime was set to $\tau_n = 2$ ns rather than 3 ns. Also, as expected, the absolute power levels were lower for the larger values of τ_n. Carrier lifetime was found to have a significant effect on lasers' dynamics—the lower value of carrier lifetime proved much more stable in terms of obtaining phase-lock. Longer τ_n resulted in SL taking more time to lock on to the ML while, conversely, phase-lock was retained for a shorter period of time. Also, three regions of injection stability were observed. Sections 4.2.2 and 4.2.3 employed averaging to reveal the underlying dynamics unobscured by noise. An asymmetric double-gradient feature of the power difference was observed in rising- and

falling-slope windows. Negative and positive dips, as well as, linearised double-gradient traces were seen in the carrier ratio figures; the temporal occurrence and the actual magnitude of these features was determined to be dependent upon injection strength, as was the magnitude of carrier suppression, with the exception of post-injection positive 'kink' which has been assumed to be a result of a lower number of photons in the cavity due to delayed circulating field in the external cavity. The range of values of the power difference and carrier ratio traces was found to be inversely proportional to the injection strength. The features present in the rising- and falling-slopes of phase difference were found to be independent of the value of κ_c^{max}.

Investigation of spectrum transfer function was performed for various levels of injection strength in section 4.3. STF for $\kappa_c^{max} = 40$ ns^{-1} displayed two peaks, the second of which subsides with increasing injection. The position and magnitude of the first peak in STF was found to be dependent upon the value of injection strength; moreover, this peak also becomes more symmetric with increasing κ_c^{max}. The presence of the secondary resonance peak in STF at $\kappa_c^{max} = 40$ ns^{-1} suggests a possibility of a yet another dynamical regime, in addition to the three originally identified in this chapter. The third, stable, regime would be divided into two subregimes—one covering SL dynamics whereby the secondary peak is present (at around 30–40 ns^{-1}), and the other without (for $\kappa_c^{max} \geq 60$ ns^{-1}). The exact boundary between these subregimes would require further investigation in order to be accurately defined. Lastly, a local maximum in STF was found for $\kappa_c^{max} = 120$ ns^{-1}.

Chapter 5

Transient chaos synchronisation process—intrinsic device properties

An initial sensitivity analysis of the robustness of the chaos synchronisation locking process was undertaken via variations in the intrinsic laser device parameters. The aim is to establish what the effect would be if one of the laser diodes was replaced by a similar, but not identical, device.

Two parameters were varied:

- carrier lifetime (section 5.1);

- linewidth enhancement factor (section 5.2).

The simulations in this chapter followed the same methodology as that outlined in the previous chapter.

5.1 Comparison of three values of carrier lifetime

The main focus of this survey was to investigate the effect the carrier lifetime has on the dynamics of ML–SL synchronisation. To this end, three values of carrier lifetime, τ_n, were chosen: 2, 3, and 4 ns; each was simulated 10,240 times with random initial conditions. For each of the three simulation series, the value of τ_n was applied simultaneously to both the ML and the SL.

The same configuration was assumed as in chapter 4 with unidirectional optical injection (see figure 1.1b), ML's feedback at $\kappa_m = 10$ ns^{-1}, and SL's at $\kappa_s = 3$ ns^{-1}. The optical injection strength was set at $\kappa_c^{max} = 160$ ns^{-1}. The meaning of vertical dashed and dotted lines in all the figures within this chapter was retained from section 4.2.2, as were the exact values of the characteristic temporal points T_1, T_2, T_3, and T_4.

Figure 5.1a was obtained by means of averaging 10,240 traces for each τ_n, separately. The resultant three average traces were then used to calculate and plot the first temporal derivative traces, which are presented in figure 5.1b. Figure 5.2a shows a two nanosecond window of the full dataset shown in figure 5.1a; periodic fluctuations are clearly visible. The frequency domain analysis of the pre-injection data is shown in figure 5.2b. The same averaging method was applied to the average phase difference in figures 5.3a and 5.3b, as well as, the average carrier difference in figures 5.4a and 5.4b. Certain selected parts of figure 5.4a were used in figures 5.4c and 5.4e to highlight features found in the rising- and falling-slope temporal windows. Similarly, parts of figure 5.4b were shown in figures 5.4d and 5.4f. Lastly, the average STF calculated within the full-injection window for the three values of τ_n is presented in figure 5.5.

Similarly to simulations performed in section 4.2.1, also here the power levels were affected by carrier lifetime. As stated on page 103, carrier injection and carrier number are proportional to $1/\tau_n$. Furthermore, reduced carriers lower the gain (see equation (2.103)), which in turn lowers the lasers' oscillation amplitudes.
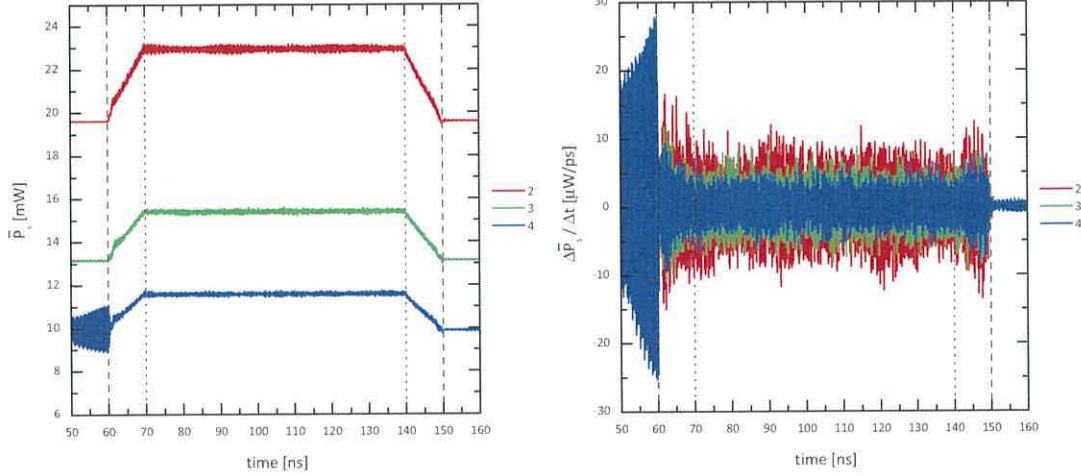
(a) Average SL power.

(b) First derivative of the average SL power.

Figure 5.1: Average SL power and its first derivative – 10,240 simulations were performed with random initial conditions and averaged for each of the three values of τ_n. The legend corresponds to carrier lifetime expressed in nanoseconds.

As a result of the aforementioned effect, the SL's average power outside of the injection window in figure 5.1a for the $\tau_n = 2$ ns trace equalled 19.8 mW, whereas for the $\tau_n = 4$ ns the power stabilised at *ca.* 10 mW. The same effect also applied within the injection window and resulted in an offset inversely proportional to the carrier lifetime. Not only did the power levels themselves change, but also, the gradients of the rising and falling edges of the optical injection profile changed accordingly. This feature is reflected in the greater range of values for smaller τ_n in figure 5.1b.

Intriguing is the range of values in the rising- and falling-slope injection windows in figure 5.1b. In the rising-slope window (between the vertical dashed and dotted lines of 60 and 70 ns, respectively), a conspicuously large fluctuation can be seen. The maximum amplitude of that range occurs at $t \approx 62.3$ ns, which in turn corresponds to the 'kink' in the rising-slopes in figure 5.1a. Similarly, in the falling-slope window in figure 5.1b (between the vertical dotted and dashed lines of 140 and 150 ns, respectively), the magnitude of the fluctuations is greater than in the injection window; it is, nonetheless,

118

still smaller than in the rising-slope window. The maximum amplitude occurs for times between 145 and 148 ns, which, again, corresponds to the (much less conspicuous) 'kink' in the falling-slope in figure 5.1a.

The occurrence of an expanding envelope for the $\tau_n = 4$ ns up until $t = 60$ ns in both, figure 5.1a and 5.1b, will be ascribed to a particular value of carrier lifetime that resulted in damping chaotic dynamics and bringing the SL down from 'coherence collapse' to a quasi-periodic regime. Nevertheless, regardless of the initial conditions, external optical injection was found to introduce stabilisation into SL's dynamics, as evidenced by low range of values in figure 5.1b in the post-injection window. As can be appreciated in figure 5.1a, both lasers in the injection window (*i.e.* between dotted lines) were synchronised. This fact is further substantiated in figure 5.3a.

In order to further analyse the power envelope in the pre-injection window for $\tau_n = 4$ ns, a subset of the data is presented in figure 5.2a. The time-domain trace corresponding to the carrier lifetime of four nanoseconds is seen to have exhibited a sustained oscillation of a significantly higher amplitude than that of the other two traces. Frequency components of the average traces are presented in figure 5.2b. The oscillation of the $\tau_n = 4$ ns trace in figure 5.2a is attributed to external-cavity modes (XCMs), as evidenced by the train of peaks in figure 5.2b. Black dashed circles in figure 5.2b denote frequency component of $f \approx 3.7$ GHz and its higher harmonics, which are clearly of higher amplitude than the surrounding XCM peaks. If this peak and its harmonics were to coincide with the relaxation oscillation frequency, then they would experience preferential amplification. To investigate this hypothesis, calculation of the relaxation oscillation frequency, f_R, was performed [249]:

$$f_R = \frac{1}{2\pi}\sqrt{\frac{G_n}{e}\left(J - J_{th}\right)}. \tag{5.1}$$
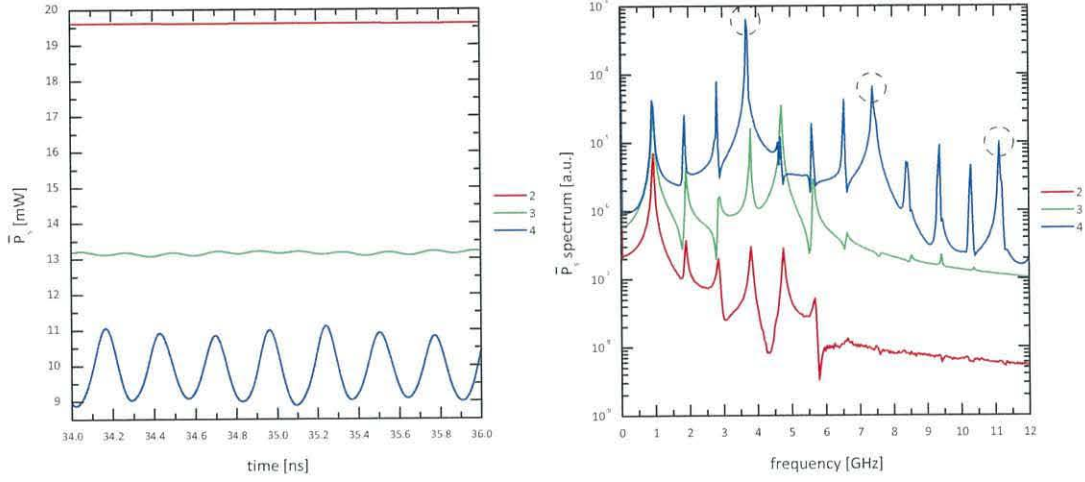
(a) 2 ns window of data shown in figure 5.1a.   (b) Frequency spectrum of the pre-injection window.

Figure 5.2: Average SL power over 2 ns window and frequency spectrum of the pre-injection window – Dashed circles indicate a peak of *ca.* 3.7 GHz and its higher harmonics. 10,240 simulations were performed with random initial conditions and averaged for each of the three values of τ_n. The legend corresponds to carrier lifetime expressed in nanoseconds.

Left side of the square root components will be defined according to equation (2.87) as:

$$G_n = v_g \frac{\partial g}{\partial N},\qquad(5.2)$$

where the term on the right side of equation can be isolated from equation (2.88) as:

$$v_g \frac{\partial g}{\partial N} = \frac{1}{\tau_{ph}(N_{th} - N_0)}.\qquad(5.3)$$

Drive current is defined as a product of current multiplier and threshold current as in equation (2.104):

$$J = I_r J_{th},\qquad(5.4)$$

where, following equation (2.105), threshold current is defined as:

$$J_{th} = \frac{eN_{th}}{\tau_n}, \tag{5.5}$$

and threshold carriers, from equation (2.106), are defined as:

$$N_{th} = N_0 + \frac{1}{g\tau_{ph}}. \tag{5.6}$$

Finally, by combining equations (5.1) through (5.6), the value of relaxation oscillation frequency is calculated as:

$$
\begin{aligned}
f_R &= \frac{1}{2\pi}\sqrt{\frac{G_n}{e}(J - J_{th})} \\
&= \frac{1}{2\pi}\sqrt{\frac{1}{\tau_{ph}(N_{th} - N_0)e}(I_r - 1)J_{th}} \\
&= \frac{1}{2\pi}\sqrt{g(I_r - 1)\frac{1}{\tau_n}\left(N_0 + \frac{1}{g\tau_{ph}}\right)} \\
&\approx 3.85 \text{ GHz}.
\end{aligned}
\tag{5.7}
$$

Since the above calculated value of relaxation oscillation frequency differs from the prominent peak of $f \approx 3.7$ GHz by only 4%, it then provides evidence to support the case that resonant enhancement of the XCM did in fact occur. When calculated for τ_n of 2 and 3 ns, the respective frequencies obtained were 5.44 and 4.44 GHz, which also correspond to peaks in the spectra of these values of τ_n in figure 5.2b.

Another feature of figure 5.2b is that for greater values of carrier lifetime, the frequency components are of higher amplitude. This feature could perhaps be explained on the grounds of decreasing damping coefficient.

The pre-injection gradient of the average phase difference in figure 5.3a was found to rise with an increase in τ_n. The post-injection gradients remained positive, however, the relationship with carrier lifetime was not that clear. The high-amplitude oscillation of
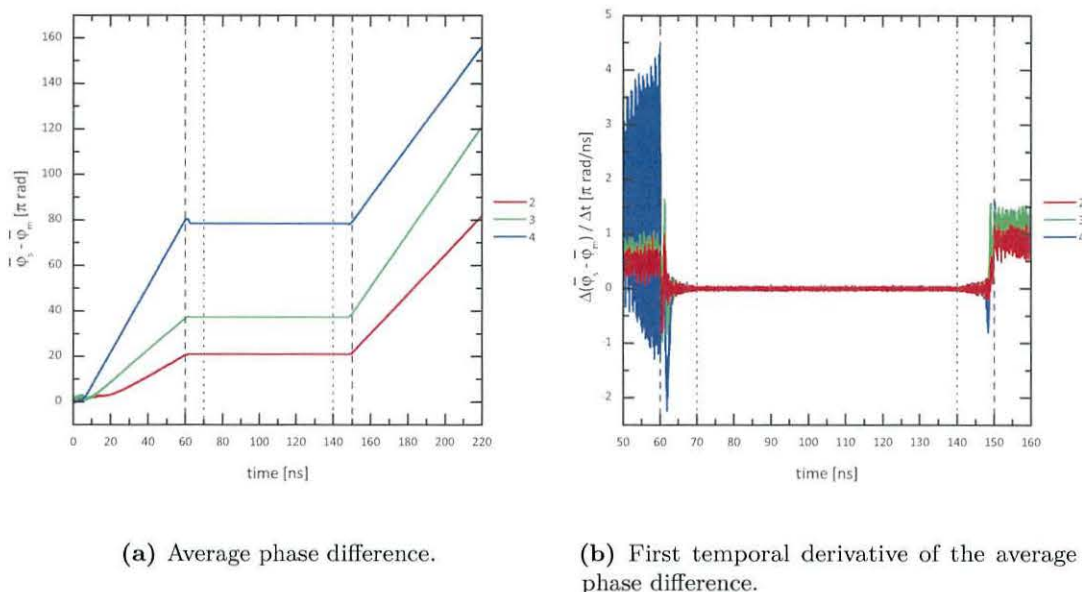
(a) Average phase difference.

(b) First temporal derivative of the average phase difference.

Figure 5.3: Average phase difference and its first derivative – 10,240 simulations were performed with random initial conditions and averaged for each of the three values of τ_n. The legend corresponds to carrier lifetime expressed in nanoseconds.

the first temporal derivative of the phase difference near the dashed lines in figure 5.3b is reminiscent of figure 5.1b. All three traces display a diminishing envelope between dashed and dotted lines in the rising-slope window and an expanding one between dotted and dashed lines in the falling-slope window. This feature can be ascribed to converging and diverging trajectories of ML and SL in the respective windows.

Similarly, the average carrier difference in figure 5.4a serves as strong evidence that the lasers were synchronised, which is manifested by stable suppression of carriers in the full-injection window. Even though the rising slope of SL's average power in figure 5.1a developed a double gradient with a conspicuous 'kink', SL's falling slope appeared with a much less pronounced 'kink'. Nevertheless, the SL's average carriers revealed both kinks, a negative one in the rising- (see figure 5.4c), and a positive one in the falling-slope window (see figure 5.4e); both are very close to the dashed lines. Comparably to figure 5.1b, where larger values of τ_n rendered a smaller range of values
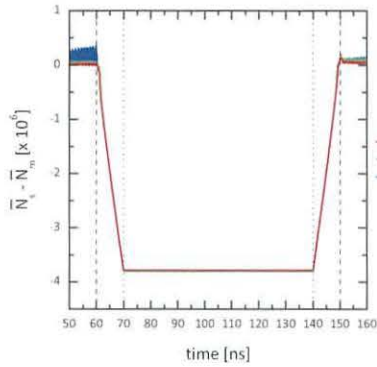
(a) Average carriers difference.
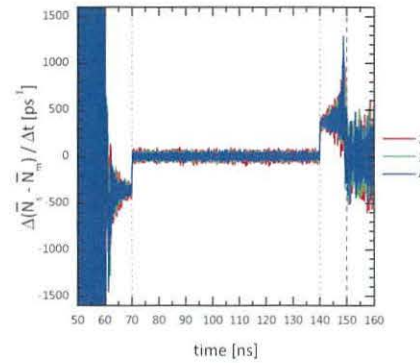
(b) First temporal derivative of the average carrier difference in figure 5.4a.
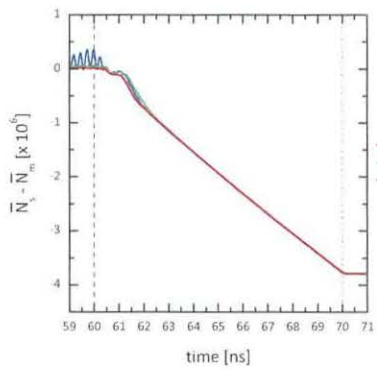
(c) Rising slope window of figure 5.4a.
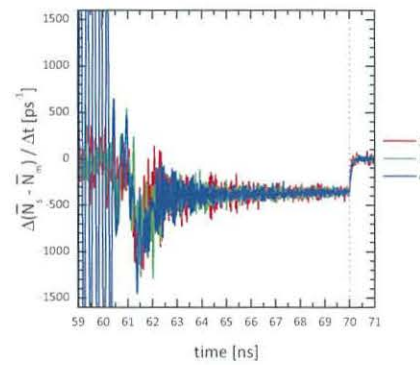
(d) Rising slope in figure 5.4b.
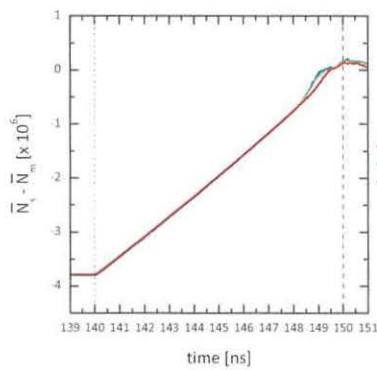
(e) Falling slope window of figure 5.4a.
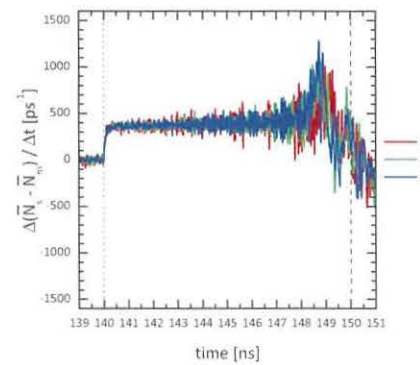
(f) Falling slope in figure 5.4b.

Figure 5.4: Average carrier difference and its first derivative – 10,240 simulations were performed with random initial conditions and averaged for each of the three values of τ_n. The legend corresponds to carrier lifetime expressed in nanoseconds.

123
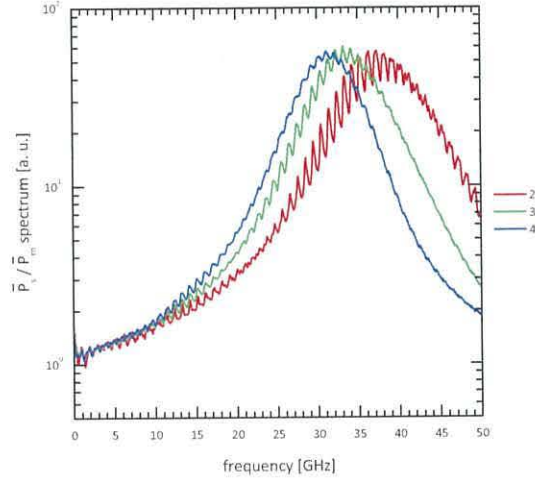
Figure 5.5: STF for three values of carrier lifetime – 10,240 simulations were performed with random initial conditions and averaged for each of the three values of τ_n. The legend corresponds to carrier lifetime expressed in nanoseconds.

in the injection window, also in figure 5.4b can the same feature be observed.

The diminishing and expanding envelopes of oscillation mentioned earlier in the context of average optical power and carriers, are probably best presented in figure 5.4b, where an almost step-change in the number of carriers can be seen along the dotted lines. This feature is investigated further in figures 5.4d and 5.4f, where a gradual carrier response can be appreciated near the dotted lines. The carrier dynamics in rising-slope window in figure 5.4f displayed, with a good approximation, a negative symmetrical relationship to that in falling-slope window in figure 5.4d.

STF traces presented in figure 5.5 experienced more pronounced XCM peaks and valleys for shorter τ_n. Changing the carrier lifetime from two to four nanoseconds resulted in STF's maxima exhibiting a negative shift by *ca.* 7 GHz. This result is consistent with an argument that lower values of τ_n would accommodate dynamics phenomena of higher characteristic frequencies.

To conclude, it has been found in this study that increasing the value of carrier lifetime by 100% (*i.e.* from two to four nanoseconds) does *not* trigger any deleterious

effects. Aside from obvious lower level of optical power and a shifted spectral content, the process of locking and unlocking remains the same. A previously unreported feature of pre-injection oscillations that would not average out to a linear limit has been observed and attributed to preferential amplification of relaxation oscillation frequency. Nonetheless, introducing optical injection from ML pushed SL into a different phase-space solution which did not exhibit any oscillations.

5.2 Sweep of Linewidth Enhancement Factor

There has been some discussion [357, 358] of the effects of linewidth enhancement factor (LEF) on locking dynamics. It is this discussion that has served as motivation for this study. Similarly to the previous section, where various values of carrier lifetime were considered, an investigation of the influence of the LEF on the synchronisation dynamics was conducted. The values range from 4.0 to 6.5 (the default being 5.0, see table 2.1) with a step of 0.5. Each value was simulated 256 times with random initial conditions. For each of the six simulation series, the value of LEF was applied simultaneously to both ML and SL. The carrier lifetime, τ_n, was fixed at 3 ns, whereas the optical injection strength was set at $\kappa_c^{max} = 80$ ns^{-1}. The laser set-up used is identical with that employed in all the previous numerical investigations (see figure 1.1b).

Figure 5.6 was prepared by taking the average SL optical power and average SL carriers and plotting one against the other (*i.e.* phase plot). The data points were split into five distinct temporal windows and plotted as such: *a*) pre-injection; *b*) rising-slope injection; *c*) full-injection; *d*) falling-slope injection; and *e*) post-injection. The average optical power difference in figure 5.7a was obtained by running 256 simulations, subsequently averaging the ML and SL power traces, and subtracting one from the other. The optical phase difference in figure 5.7b was obtained the same way. The correlation coefficient between ML and SL optical powers in figure 5.8 was calculated in

5 μs, non-overlapping, time slots of single-run data and plotted for the six values of LEF. The average carrier difference in figure 5.9 followed the procedure used with regard to figure 5.7b. Lastly, the SL spectrum in figure 5.10a was calculated in the middle of the full-injection window for each value of the linewidth enhancement factor; when divided by ML's spectrum, it was used to obtain the spectral transfer function in figure 5.10b.

The following three regions were identified:

- for $\alpha \in [4.0, 5.0]$ the traces displayed characteristic signs of chaotic oscillation and averaged to a pattern which had been observed in numerical simulations in the previous chapter;

- for $\alpha \in [5.5, 6.0]$ lasers still displayed signs of chaotic oscillation, although the distinctive feature here constituted the fact that SL experienced additional self-induced oscillation patterns in the pre-injection window;

- for $\alpha = 6.5$ SL displayed signs of being chaotic in the figures of the optical power and phase difference, however, not in the SL's carrier number in the injection window, which is why it is postulated that at this value of LEF SL failed to lock-on to injection from ML.

Figure 5.6a represents SL's average trajectory in the pre-injection window. The trajectories adopted by the traces in all subfigures of figure 5.6 were mostly clockwise. The SL would begin oscillating at some initial point (as imposed by random initial conditions), and then migrate towards the nearest attractor. The traces of $\alpha = 5.5$ and 6.0 developed a bigger ellipse in comparison to those of smaller α, whereas the trace of $\alpha = 6.5$ developed initial transients first, which then gave way to clamped carriers and deep modulation of photons (hence the elongated horizontal bar). Figure 5.6b represents the rising-slope injection window. SL is seen here to traverse the phase-space (clockwise and downwards) towards greater optical powers and depleted carriers as a result of the injection. The initially elliptic traces of $\alpha = 5.5$ and 6.0 became more localised. The

(a) Pre-injection window, $(t \in [0, 60]$ ns$)$.

(b) Rising slope, $(t \in [60, 70]$ ns$)$.

(c) Full injection window, $(t \in [70, 140]$ ns$)$.

(d) Falling slope, $(t \in [140, 150]$ ns$)$.

(e) Post-injection window, $(t \in [150, 220]$ ns$)$.
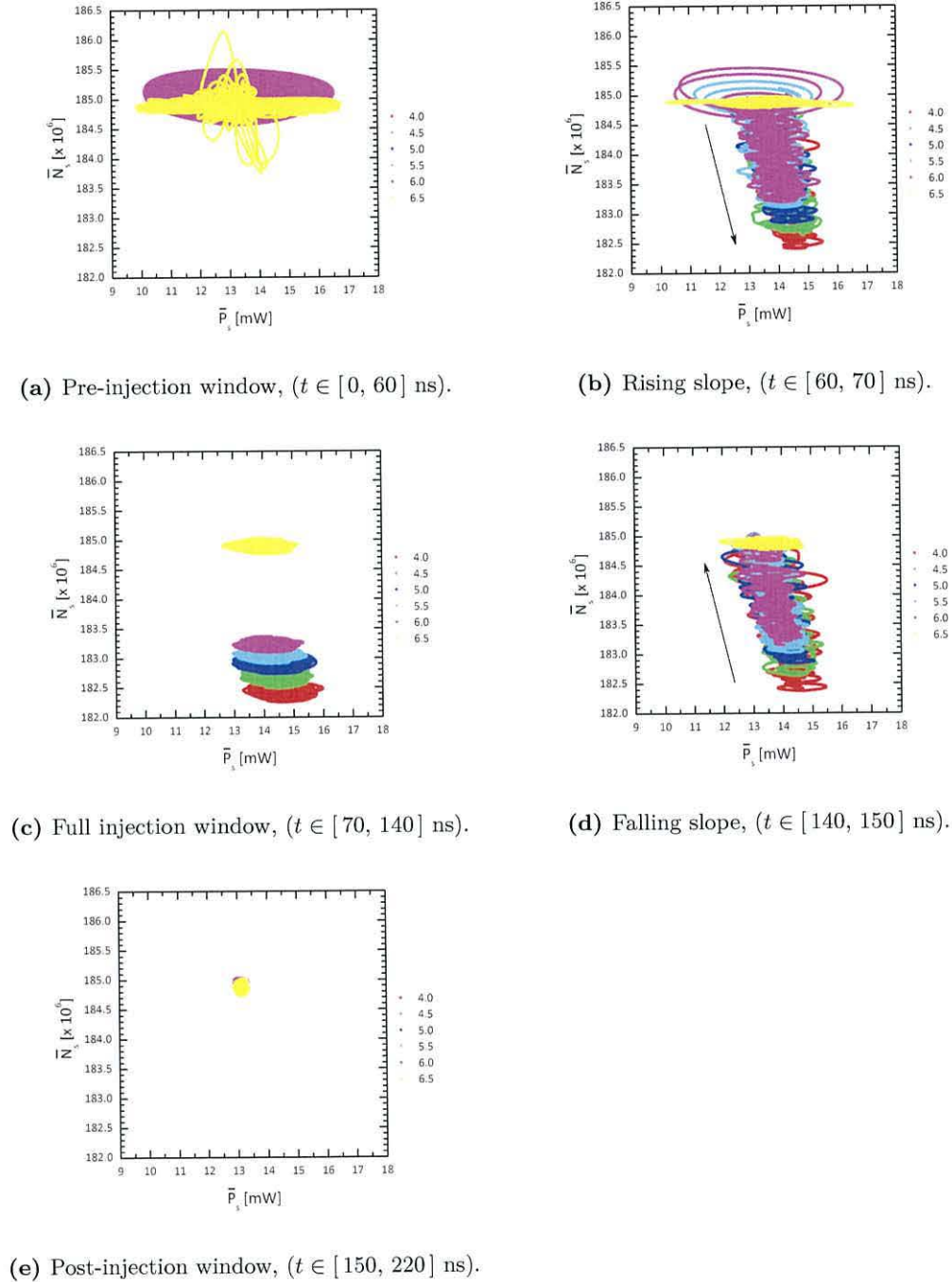
Figure 5.6: Average SL carriers versus average SL power – The average trajectories in all temporal windows and for all values of LEF followed a roughly clockwise trajectory. Where appropriate, black arrows denote the traverse direction of the trajectories. 256 simulations were performed with random initial conditions and averaged for each of the values of LEF. The legend corresponds to the values of LEF.

127
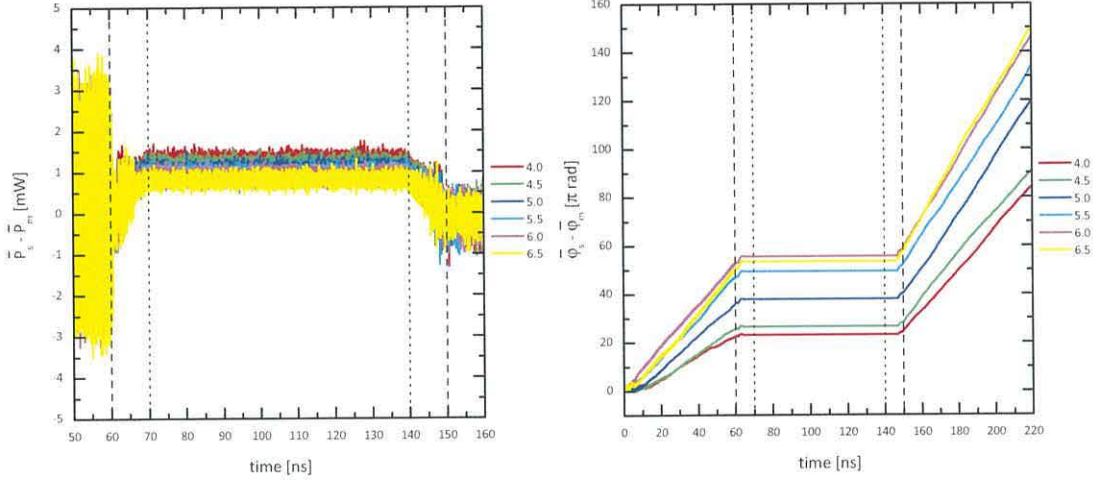
(a) Average optical power difference.

(b) Average phase difference.

Figure 5.7: Average difference of optical power and phase – 256 simulations were performed with random initial conditions and averaged for each of the values of LEF. The legend corresponds to the values of LEF.

trace of $\alpha = 6.5$, whose trajectory initially resembled a horizontal bar, also became localised. Figure 5.6c represents the full-injection window, whereby all the six traces form comparably shaped and localised ellipses. Traces corresponding to LEF between 4.0 and 6.0 can be seen to be synchronised and separated by an offset in the number of carriers, and (to a lesser degree) in optical power. In contrast, the trace of $\alpha = 6.5$ remained where it was in figure 5.6b. It can, nonetheless, be argued that the optical injection exerted a stabilising effect. Figure 5.6d represents the falling-slope injection window, which can be treated as the reversal traverse (clockwise and upwards) of that in figure 5.6b. Figure 5.6e represents the post-injection window, where all the traces are confined to, and occupy almost the same point in the phase-space.

The following values of linewidth enhancement factor: 5.5, 6.0, 6.5, exhibited large amplitude fluctuations in the pre-injection window in figure 5.7a. Increasing the value of LEF did not affect the ML average power traces.[1] It did, however, have an impact

---

[1]Which is why they are not included here.
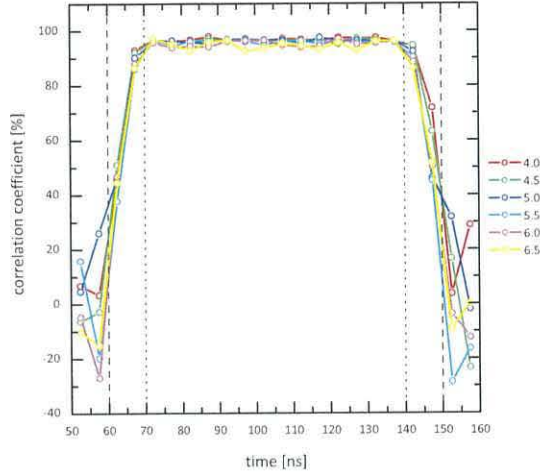
Figure 5.8: Correlation coefficient between ML and SL optical powers – Correlation was calculated for consecutive 5 µm slices. Single-simulation traces were used with identical initial conditions. The legend corresponds to the values of LEF.

on SL average power traces in the full-injection window. Namely, with the increase in value of the α-factor, the SL average power decreased. In the post-injection window, the only difference (and a small one at that) was the range of values of average power difference, which decreased with increasing value of LEF.

Increasing the value of LEF in figure 5.7b resulted (with the exception of $\alpha = 6.5$) in a proportional decrease in the time delay between the beginning of simulation and the moment when average phase difference traces adopted a stable gradient in the pre-injection window. That pre-injection gradient was found to be proportional to LEF (again, with the exception of $\alpha = 6.5$). This feature can be explained as a direct consequence of lasers adopting more negative phase gradients with increase in LEF.

Perhaps the most striking feature of figure 5.7b is that the characteristic time required for the lasers to lock-on (on the rising slope of ramping function, $t \in [61, 63]$ ns), as well as, to unlock (on the falling slope of ramping function, $t \in [147.5, 149.5]$ ns) was found to be independent of the LEF, at least for the range of values chosen in this survey. The phase difference was stable over the entire duration of injection window for *all* values of
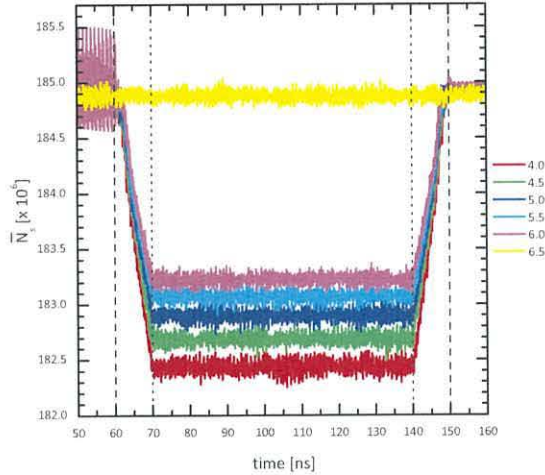
Figure 5.9: Average SL carriers – 256 simulations were performed with random initial conditions and averaged for each of the values of LEF. The legend corresponds to the values of LEF.

α. Moreover, as a result of external injection, the post-injection gradients were greater than the pre-injection ones. Since ML's phase gradients remained virtually constant (for each value of LEF), *ergo* it is the SL's phase gradients that became less negative in the post-injection window in comparison to the pre-injection window. Also, a nonlinear dependence of the average phase difference on LEF was observed in the full-injection window. The amount of phase offset was the most significant for $\alpha \in [4.5, 5.5]$. The offset between any other adjacent pair was significantly smaller.

As shown in figure 5.8, no significant difference in synchronisation quality between ML and SL in the full-injection window was observed. Traces in the pre- and post-injection windows display a markedly weaker correlation of no more than $\pm 30\%$.

What figure 5.9 signifies is the fact that with an increase in LEF, carrier suppression over the full-injection window in SL decreases. Only for $\alpha = 6.5$ did the SL carriers retain the same level in the full-injection window as outside of it. Similarly to what has been said before, in the case of average SL carriers in figure 5.9, it can be shown that for certain values of LEF (specifically, the range between 5.5 and 6.5) the dynamic

(a) Average SL spectrum.

(b) Average STF.
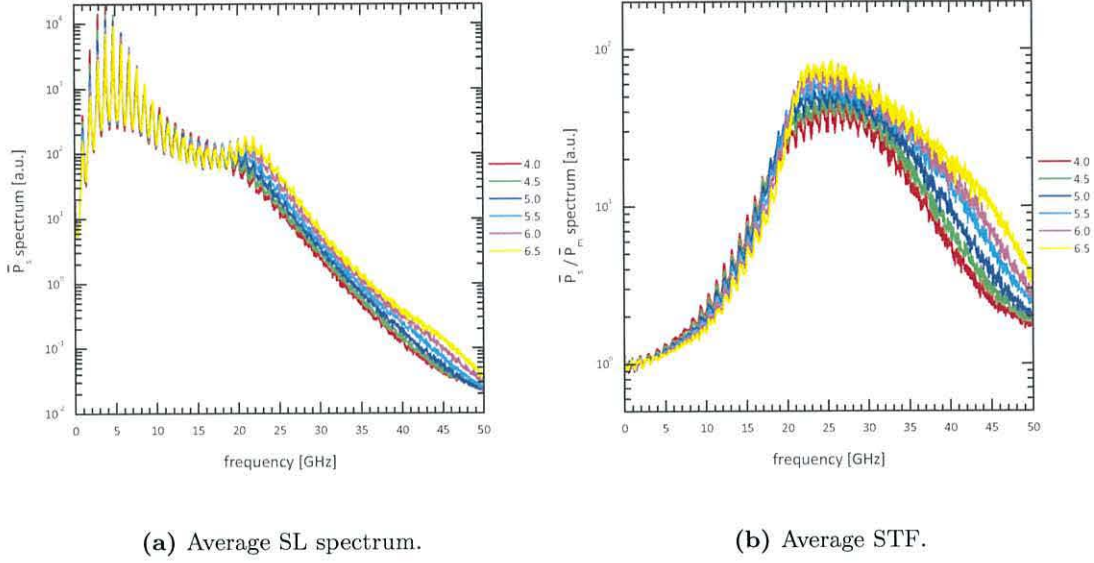
Figure 5.10: SL spectrum and STF as a function of LEF – 256 simulations were performed with random initial conditions and averaged for each of the values of LEF. The legend corresponds to the values of LEF.

developed a recurring pattern of pre-injection perturbations irrespective of the initial conditions. On the other hand, the post-injection region in figure 5.9 is devoid of any perturbations, which is reminiscent of optical power difference seen in figure 5.7a.

The SL power and carriers traces in the post-injection window, however, did average out to a roughly straight line thus implying that post-injection fluctuations were not, in general, present. This feature could be explained on account of introduction of sufficient amount of optical injection, which resulted in shifting phase-space of SL sufficiently away from its pre-injection phase-space.

One can immediately appreciate the effect LEF has on average SL spectrum in figure 5.10a; with the increase in value of the α-factor, the spectrum develops increasingly pronounced secondary peak at the approximate frequency of 21–22 GHz. This peak is then followed by a long tail of larger amplitude for larger values of LEF. The spectral peaks around the resonance frequency are also dependent on the value of linewidth enhancement factor; increasing α-factor results in smaller peaks and shallower valleys.

In general, the greater the α-factor, the higher the amplitude and the frequency of the secondary peak in SL's spectrum.

Spectral transfer function in figure 5.10b corroborates the above observation. Increasing the value of LEF resulted in increasing the amplitude of the peak in the STF, but also in a reduction of the peak's corresponding frequency. Traces can be seen to cross at the frequency of around 19–20 GHz. Below that value, increasing LEF lowers the amplitude of STF. Above that value, increasing LEF increases the value of STF. Throughout the entire frequency range, larger values of linewidth enhancement factor were seen to render XCM peaks less pronounced.

5.3 Conclusions

No substantive effect of device substitution has been observed. Other parameters being equal, varying values of carrier lifetime and linewidth enhancement factor did not affect the synchronisation process to a significant degree. Nonetheless, varying these parameters did affect the details of chaos dynamics—*vide* SL spectra or STF.

In section 5.1 an investigation of the effect of the carrier lifetime has on SL's dynamics was performed. As expected, optical power levels were greatly affected. Additionally, 'kinks' in the SL's optical power figures were observed and tied with SL's optical power first derivative. The pronounced XCM peaks in the spectra of the average SL optical power (in figure 5.2b) were found to correspond with laser's relaxation oscillation frequency, which manifested itself in their preferential amplification (in particular, for $\tau_n = 4$ ns). The transitions of SL's carriers were found to prompt fewer oscillations when SL was subjected to changing, but already high, values of optical injection (see proximity of dotted lines in figure 5.4b). Conversely, SL's carriers displayed high-amplitude oscillations when the SL was in transition from no injection to low injection and *vice versa* (see proximity of dashed lines). The SL carriers were observed to be

capable of swift transitions between regimes of stable and changing injection. The carrier lifetime affected the SL's spectrum and STF to the extent of moving the STF peak towards lower frequencies with increasing value of τ_n. Shorter carrier lifetimes were found to be more accommodating of high-frequency phenomena; they also gave rise to smaller transients in the phase difference derivative.

Comparison of the effect various values of linewidth enhancement factor have on SL dynamics was performed in section 5.2. Three ranges of dynamical properties were observed with varying degrees of chaos-synchronisation properties. By sweeping the LEF from 4.0 up to 6.0 no significant process occurred, which would exert a deleterious effect on the synchronisation dynamics. Only did the $\alpha = 6.5$ case exhibit lack of carrier synchronisation, although it still developed optical power and phase difference plots comparable to other values of LEF. This point alone can be interpreted as evidence supporting published observations that the synchronisation indeed becomes more difficult for greater values of α. The actual moment when phase lock occurs and disappears was found to be independent of the value of α. Nevertheless, phase offset was found to be nonlinearly dependent on LEF, in particular for the values between 4.5 and 5.5. External optical injection was found to exert a lasting stabilising effect on SL for those values of LEF which had triggered pre-injection perturbations. SL's spectrum displayed a tendency to develop a secondary peak with increasing value of linewidth enhancement factor. That tendency was later reflected in the STF, whose peak was proportional to LEF.

Chapter 6

Experimental investigation of the transient locking process

This chapter describes two different experimental configurations which aim to:

- investigate the SL's transient response to optically chopped cw injection from ML (section 6.1);

- investigate the dynamics of TE and TM modes of an ECSLD (section 6.2).

6.1 Synchronisation transients

The main motivation of this survey was to investigate the transient dynamics of chaos-synchronised ML–SL set-up whose injection arm would be subjected to periodic perturbation by an optical chopper (see figure 6.1). The rationale behind this survey was that owing to the finite non-zero cross-section of the injection beam and the slowly-changing (relative to lasers' carrier dynamics time-scale) transmission profile of the optical chopper's wheel, the effective transmission profile would be very smooth in contrast to the step-like electrical output of chopper's controller that was used as sampling trigger for the digital oscilloscope. As a direct consequence, it would also be

possible to investigate the SL's dynamics in a circumstance where the laser is exposed to this slowly changing optical injection rate [359].

The dynamics of the transients occurring in SL switching regions of optical chaos injection and optical feedback proved to be complex, however, an unexpected and previously unreported phenomenon has been observed experimentally and found to occur in unidirectionally coupled ECSLDs (see figure 1.1a). The hallmark of this new phenomenon manifests itself in the form of an hourglass-shaped plot of SL-vs-ML time-domain optical power, with two centres of high power density. Both lasers need to be rendered chaotic in a closed-loop configuration (see figure 1.1b) and subsequently synchronised. Removing the ECM stabilises the ML and ensures cw operation is obtained; the SL's ECM, on the other hand, would remain in place. It is at this stage that the switching transients would emerge. The switching would not emerge, however, if the lasers were not synchronised *a priori*. This phenomenon is neither self-sustaining nor self-perpetuating—it only occurs when switching between different regimes takes place, *ergo*, for as long as the optical chopper is operating.

Experimental configuration

The configuration, which is depicted in figure 6.1, was very similar to, and builds upon, the ones employed in sections 3.1 and 3.2. Assumptions and limitations carry over from those previous experiments. The particular lasers in this experiment shared the same value of solitary threshold current of $I_{th} = 27.1$ mA, and the same value of solitary lasing wavelength $\lambda = 824.4$ nm. Details pertaining to the other components can be found on page 62. The injection arm in this case consisted of two optical isolators, an optical attenuator, optical chopper (Stanford Research Systems SR540 chopper controller), and a half-wave plate. The detection side of the ML was also expanded to allow for recording of the TE and the TM polarisations independently. Optical spectra were recorded with Agilent 86141B optical spectrum analyser.

In this experimental survey the exact values of parameters (here I_{ML}, T_{ML}, I_{SL}, and T_{SL}) were not the focus of the study, but rather it is the state of 'coherence collapse' that was deemed crucial. Nonetheless, the exact values employed in the experiment are listed in table 6.1. The phenomenon was observed under different operating conditions, rather than only for a unique set of parameters; it was also observed to be independent of chopper's frequency, however, due to hardware limitations, the experimental investigation was performed over a limited frequency range between 100 Hz and 3.4 kHz. A typical time-domain amplitude trace of the optical chopper can be appreciated in figure 6.2.

Basic laser parameters

Both drive currents and lasers' temperatures were recorded and are presented in table 6.1. The NDF_1 was used to adjust the optical power so that it would not exceed the maximum permissible incident power on the detector. The HWP_1 was used to rotate the incoming optical beam to align it with the PBS thereby assuring that the subsequent split into two polarisations was optimised. Optical isolators ISO_1 and ISO_2 were used to minimise back-reflection from the detectors. Detectors D_1 and D_2 were used to record the ML's TE and TM (respectively) polarisation time-domain optical output. The NDF_2 was used to control the ML's optical feedback rate. Optical isolators ISO_3 and ISO_4 were used to achieve isolation of $ca.$ -80 dB and prevent the SL from driving the ML. The optical chopper (CHP) was used to introduce regular and controlled perturbation to the injected optical beam. The NDF_3 was used to control the strength of the optical injection. The HWP_2 was used to rotate the injected optical beam to align it with the SL. The NDF_4 was used to control the SL's optical feedback rate. The SL's time-domain optical power trace was recorded with detector D_3.

All the NDFs and the HWPs, as well as, the optical chopper were aligned obliquely so as to form a non-normal angle between the incident optical beam and the components' facets, thereby reducing the etalon effect and back-reflection.
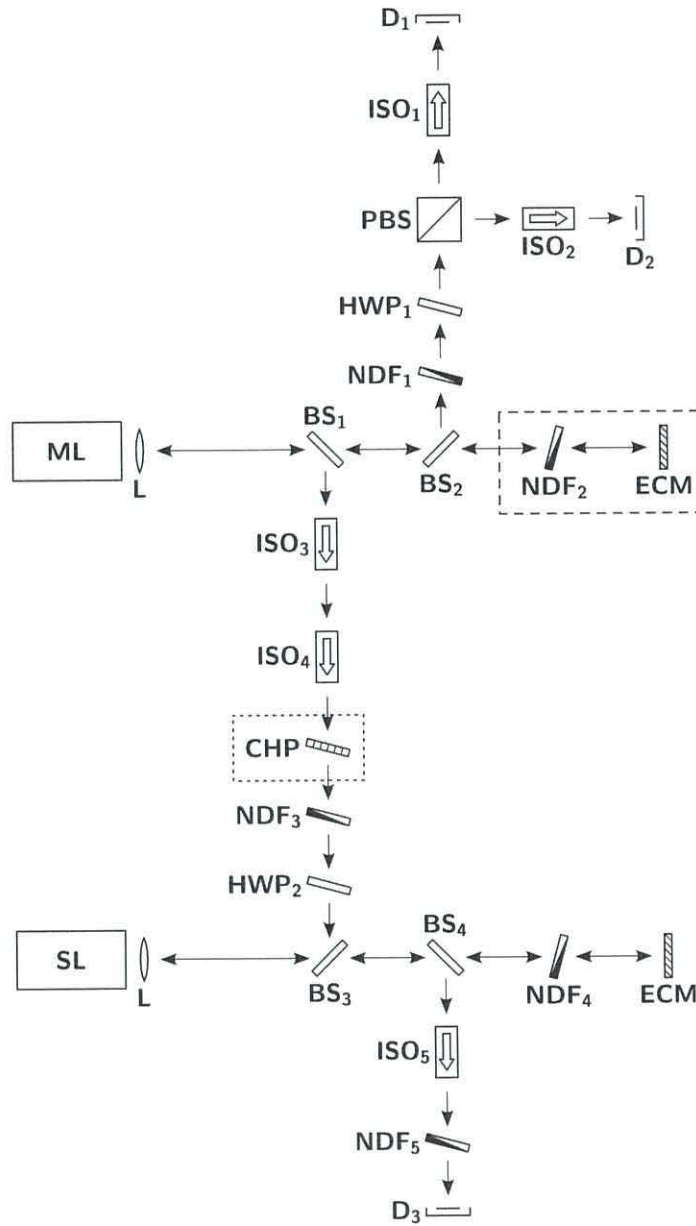
Figure 6.1: Experimental set-up – The element confined in the dotted box would be introduced into, whereas the two elements confined in the dashed box would be removed from the set-up as outlined in the procedure on the next page. BS (beam splitter), CHP (optical chopper), D (detector), ECM (external-cavity mirror), HWP (half-wave plate), ISO (optical isolator), L (collimating lens), NDF (natural density filter), PBS (polarising beam-splitter).
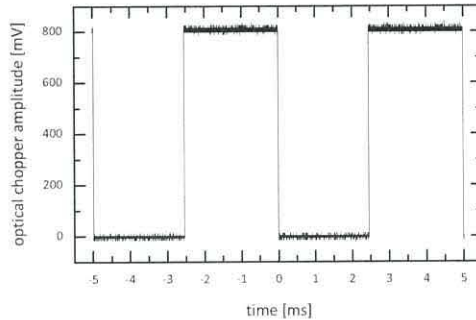
Figure 6.2: Typical electrical output of the optical chopper's controller used as a trigger – Chopper's operating frequency in this figure was set to 200 Hz.

Experimental procedure

The optimisation procedure followed was very similar to that employed in sections 3.1 and 3.2. Full details of are outlined below:

1. Both lasers were rendered chaotic separately. To prevent interaction between the lasers, the injection arm would remain blocked;

2. The set-up was left undisturbed for 30 minutes[1] to reach equilibrium with the environment;

3. The unidirectional optical injection was introduced and SL synchronised to the ML by adjusting the injection rate (via NDF_3), as well as, the SL's drive current, temperature and optical feedback rate (via NDF_4) so as to maximise the correlation coefficient. Exact values of I_{SL} and T_{SL} can be found in table 6.1;

4. An optical chopper was introduced into the injection arm (see dotted rectangle in figure 6.1) and the first results were recorded (see column 'A' in table 6.1);

5. ML ECM was removed thereby rendering ML solitary (see dashed rectangle in figure 6.1). The second set of results was recorded (see column 'B' in table 6.1). Note change of scale in ML dynamics in figures 6.3 and 6.4;

---

[1]Local practice.

138

Table 6.1: Experimental parameters employed in the transients investigation –
ML's parameters were kept fixed, whereas SL's were adjusted in four consecutive measurements.

Parameter		Setting			
		A	B	C	D
I_{ML}	[mA]		40.28		
T_{ML}	[°C]		22.16		
I_{SL}	[mA]	34.97	34.97	36.49	31.08
T_{SL}	[°C]	21.59	21.59	21.44	21.77

6. I_{SL} and T_{SL} were adjusted twice and thus the third and fourth batch of results were recorded (see columns 'C' and 'D' in table 6.1).

To capture the long-term dynamics, time-domain traces of the ML's and the SL's optical power (figure 6.3) were recorded with a digital oscilloscope over 500 µs time window. The very same datasets were used in plotting of 10 µs traces (figure 6.4) which are centred on the middle of the injection window. The purpose of this was to portray lasers' dynamics with high temporal resolution. Visual cue is provided in the form of vertical dashed grey lines in figure 6.3. Simultaneously, lasers' optical power spectra and spectral transfer function (STF) were recorded (figure 6.5) with the same digital oscilloscope. Smoothed traces for all three frequency-domain plots were calculated in Origin®. Density contour plots (figure 6.6) were prepared in Origin® *a posteriori* the experiment from the above mentioned five-microsecond time-domain traces. CC in figure 6.7 was calculated in 10 µs, non-overlapping, time slots from data in figure 6.3 and plotted accordingly for all four subexperiments. Finally, in figure 6.8 presented are 10 ns time-domain traces of data in figure 6.3.
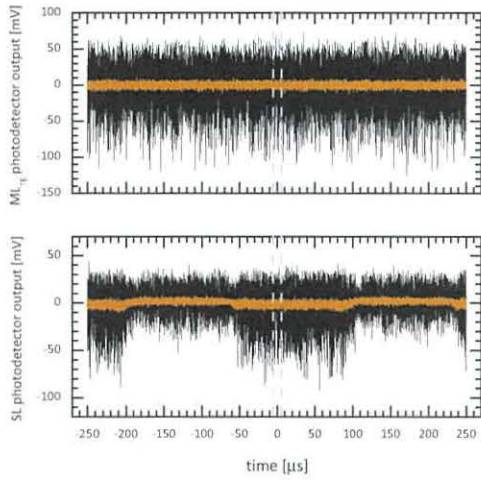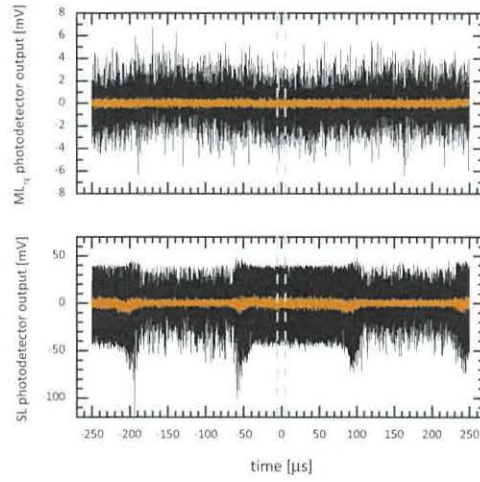
(a) Both ML and SL chaotic.

(b) ML stable; SL chaotic.

(c) ML stable; SL chaotic and increased I_{SL}.

(d) ML stable; SL chaotic and periodically stabilised.

Figure 6.3: ML_{TE} and SL optical power time-domain traces – The orange colour denotes the average of 100 traces. Subcaptions correspond to a particular column in table 6.1. Detector's typical conversion gain at 850 nm is 300 V/W.

Typical temporal and spectral traces—Chopped injection locking

Having followed the procedure and reached point 4 (see also column 'A' in table 6.1), the ML was still chaotic and the SL displayed two temporal patterns of oscillation—injection locking and its own inherent chaotic dynamics—alternating at the optical chopper's frequency $f_{CHP} = 3.4$ kHz.

In figure 6.3a one can readily appreciate marked difference in the range of amplitude variation in SL's time-domain trace; injection window is clearly defined. Also, traces of higher temporal resolution are presented in figure 6.4a; the temporal scale of that figure corresponds to the vertical dashed lines in the former figure.

In accordance with the injection-locking theory, if two lasers are synchronised, their spectral components share a high degree of similarity with the exception of the attenuation of the low-frequency components in the SL, which is presented in figure 6.5a. The synchronicity of the two lasers can also be seen in figure 6.6a, where the lasers' amplitude variation forms a diagonal line.

In the injection window, corresponding to higher-amplitude fluctuations seen in figure 6.3a, the correlation coefficient (CC) between ML and SL amounted to *ca.* 82% (see figures 6.4a and 6.6a). In the injection-blocked window, corresponding to lower-amplitude fluctuations in figure 6.3a, CC was approximately equal zero.

ML ECM removed—cw injection

As mentioned before, three further measurements were conducted in addition to the first measurement of typical dynamics:

- The **second** experiment (see point 5 in the procedure and column 'B' in table 6.1) in which ML's ECM was removed from the set-up thereby turning ML into a solitary laser. From this moment onwards, the chaotic SL would be injected with chopped optical cw beam.
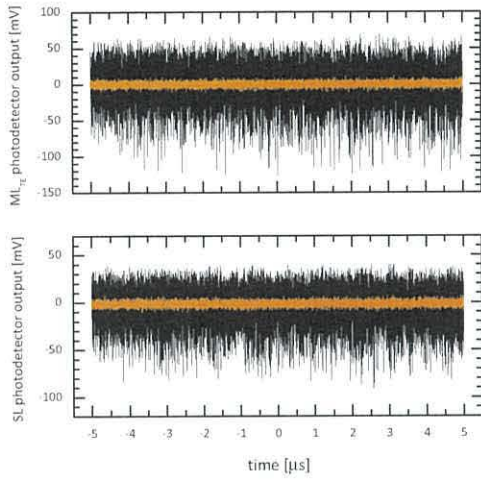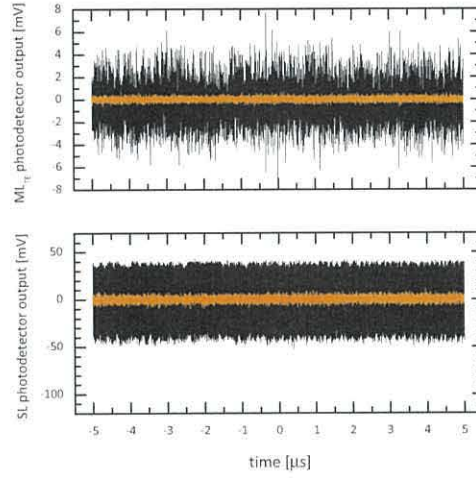
(a) Both ML and SL chaotic.

(b) ML stable; SL chaotic.

(c) ML stable; SL chaotic and increased I_{SL}.

(d) ML stable; SL chaotic and periodically stabilised.

Figure 6.4: Expanded view of ML_{TE} and SL optical power time-domain traces – Data ranges correspond to the grey dashed lines in figure 6.3. The orange colour denotes the average of 100 traces. Subcaptions correspond to a particular column in table 6.1. Detector's typical conversion gain at 850 nm is 300 V/W.

- The **third** experiment (see point 6 and column 'C') which represents the situation where I_{SL} and T_{SL} were adjusted so as to obtain the hourglass-shape of the highest amplitude possible. Had ML's ECM been re-introduced at this point, the ML–SL set-up would have displayed chaos synchronisation.

- The **fourth** and final experiment (see point 6 and column 'D') which represents the situation where I_{SL} and T_{SL} were further adjusted so as to break that pseudo-synchronisation state altogether. The chopped optical cw injection from ML served the role of stabilising the SL's dynamics and suppressing the SL's chaotic oscillation.

The orange traces present in figure 6.3 denote an average of 100 traces acquired and processed in the digital oscilloscope. These average traces clearly illustrate the different dynamics that can be induced. The average value and standard deviation of the orange lines show significant disparity between figures 6.3a through 6.3d. That range remained approximately constant between measurements 'A' (figure 6.3a) and 'B' (figure 6.3b) in spite of ML injecting much lower amount of power into SL in the latter case (owing to removal of its ECM). However, it increased significantly in 'C' (figure 6.3c) as a result of adjusting SL's parameters. It was then reduced to a minuscule scale with the transition to measurement 'D' (figure 6.3d); in fact, in this case, injection from ML gave rise to a *smaller* range of values in comparison to that outside of the injection window. That observation would suggest that the range of values of average optical power in SL is much more sensitive to SL's parameters rather than injection from ML. The above discussion applies to figure 6.4 analogously.

Figure 6.5a presents typical traces of ML and SL optical spectrum—one with clearly discernible peaks stemming from ML's ECM, as well as, amplification of spectral components around 1.5–3.0 GHz range by SL. Removal of ML's ECM rendered the laser solitary, hence its flat spectrum in figure 6.5b. The SL, on the other hand, developed
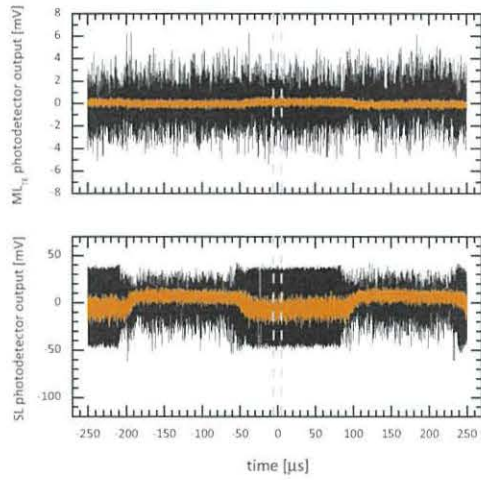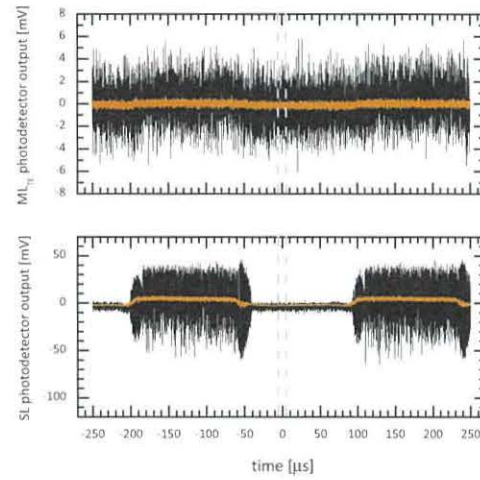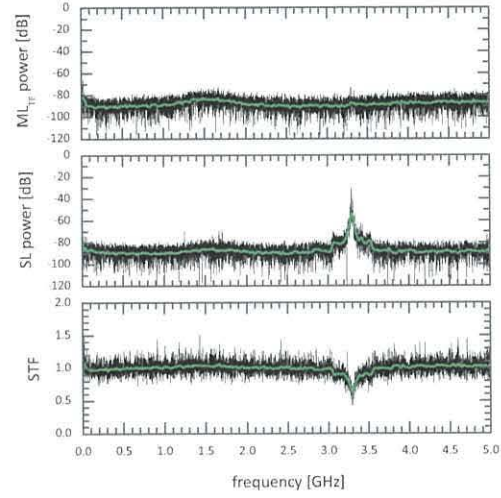
(a) Both ML and SL chaotic.

(b) ML stable; SL chaotic.
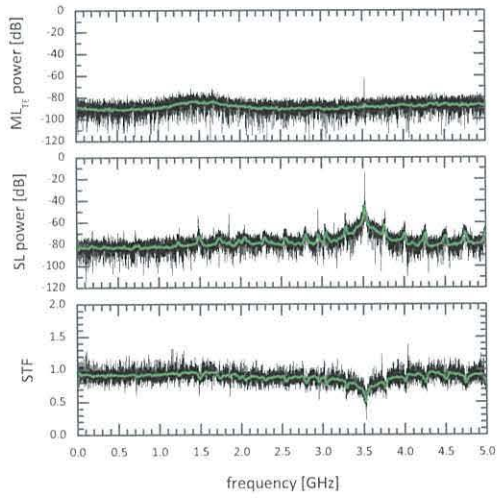
(c) ML stable; SL chaotic and increased I_{SL}.
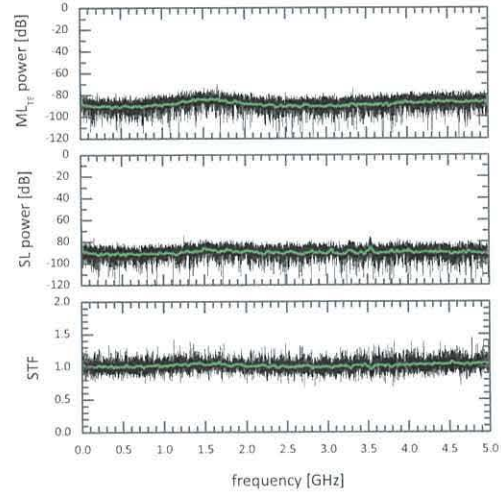
(d) ML stable; SL chaotic and periodically stabilised.

Figure 6.5: Optical power spectra and STF of the instantaneous time-domain traces – Traces in figure 6.4 were used in calculation of spectrum. The data was smoothed with 50-sample adjacent smoothing and the resultant trace is denoted in green. Subcaptions correspond to a particular column in table 6.1. Detector's typical conversion gain at 850 nm is 300 V/W.

a flat spectrum, too, but with a conspicuous peak at the frequency $f_B = 3.29$ GHz in the injection window. That observation would suggest two conclusions—firstly, that the ML stabilised the SL, and secondly, that SL exhibited a selective amplification of a single frequency. Further adjustment of SL's parameters resulted in a shift of that peak in SL's spectral towards higher frequencies (see figure 6.5c), where the main peak corresponds to the frequency $f_C = 3.52$ GHz. Furthermore, a train of higher- and lower-order cavity modes also developed. This experiment also shows that the aforementioned mechanism of selective amplification in SL is sensitive to SL's drive current and temperature. Finally, measurement 'D' in figure 6.5d saw the disappearance of SL's spectral components and effectively turned the SL into a solitary laser in the injection window. Throughout the entire experiment the optical chopper's frequency was set to $f_{CHP} = 3.4$ kHz which is six orders of magnitude smaller than the frequency of the two main peaks found in spectra.

Transition between stages 'A' (figure 6.6a) and 'B' (figure 6.6b) was accompanied by a shift from high-quality synchronisation density plot in the shape of a diagonal line to an hourglass-like figure. SL's amplitude range in the density plot experienced a decrease from $[-40, +30]$ mV to ± 25 mV, which is a consequence of removing ML's ECM—by removing the external mirror, the number of photons in the ML's internal cavity decreased resulting in lower optical power. This, in turn, translated into lower injection rate and consequently fewer photons in SL's internal cavity. ML's amplitude range in the density plot is confined to ± 3 mV near the two density centres and it constitutes uncorrelated stimulated emission from ML; taking into consideration ML was, at that time, lasing at cw, then this amplitude range represents the magnitude of noise in ML's output. CC in the injection window suffered severe penalty dropping from 82% to mere 3% (see figure 6.7). Outside of injection window, the CC was close to zero. Lastly, SL's spectrum underwent transformation with emergence of amplification peak at the aforementioned frequency f_B.
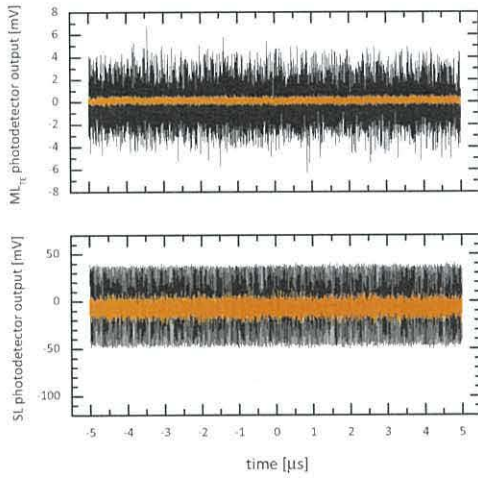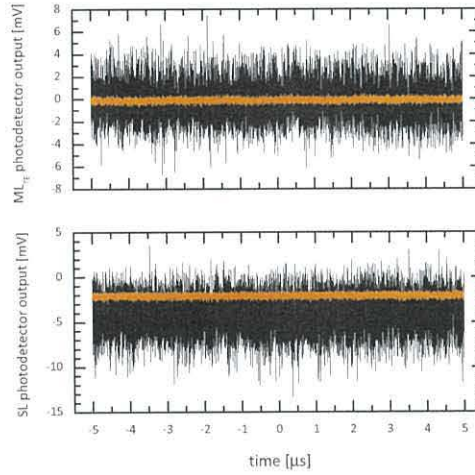
(a) Both ML and SL chaotic.

(b) ML stable; SL chaotic.

(c) ML stable; SL chaotic and increased I_{SL}.
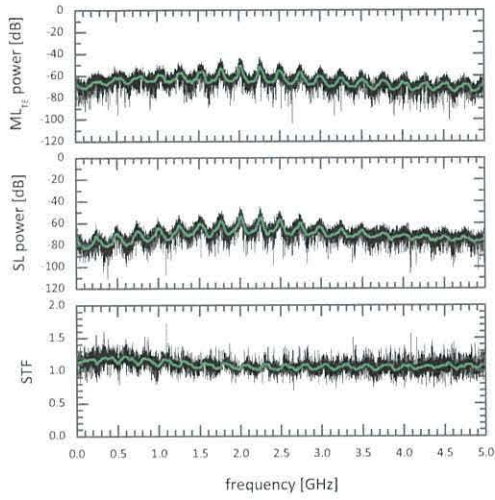

(d) ML stable; SL chaotic and periodically stabilised.
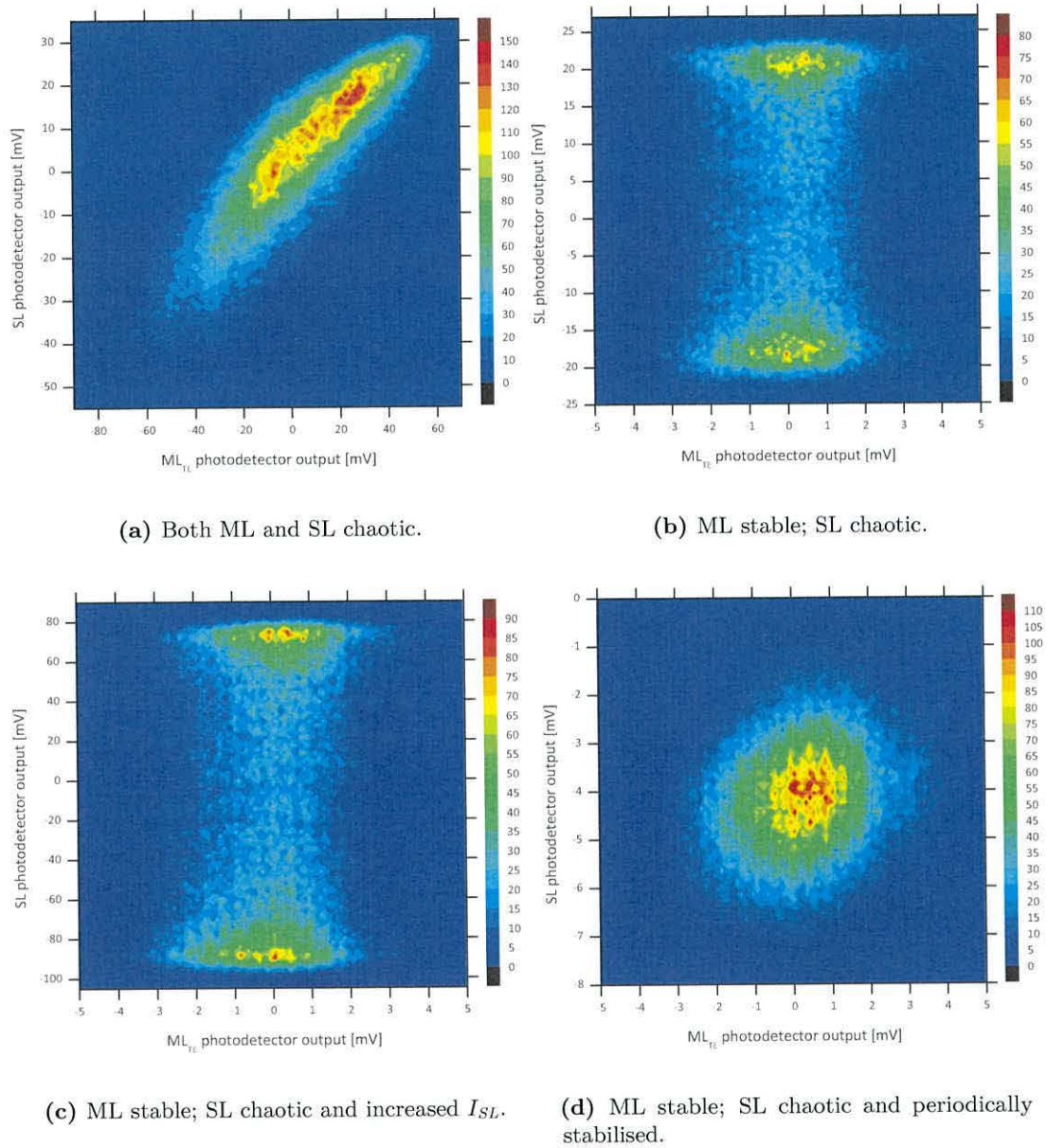
Figure 6.6: Density plots of ML_{TE} versus SL – Traces in figure 6.4 were used in plotting these density plots. The colour bar denotes the number of samples within given area. Subcaptions correspond to a particular column in table 6.1. Detector's typical conversion gain at 850 nm is 300 V/W.

146

Transition between stages 'B' (figure 6.6b) and 'C' (figure 6.6c) was accompanied by a significant increase in SL's amplitude range in density plot up to $[-100, +80]$ mV paired with unchanged range in ML's amplitude. The overall shape of the hourglass was also retained. This outcome was obtained after optimising SL's drive current and temperature so as to achieve the greatest amplitude range in SL—no other changes were introduced into the set-up, hence the same dynamics of ML was observed. The value of CC fell to approximately 2% in the injection window. Lastly, SL's spectrum experienced a peak transition between frequencies f_B and f_C, which be explained on the grounds of shifting laser's emission to shorter wavelengths with increase in drive current.

Transition between stages 'C' (figure 6.6c) and 'D' (figure 6.6d) was accompanied by reduction of SL's amplitude range to $[-7, -1]$ mV; ML's range, again, was the same as in stages 'B' and 'C' since no changes were introduced to the set-up, except for SL's drive current and temperature. Optical cw injection from ML served the purpose of stabilising otherwise chaotic SL [360–362].

Density plots in figure 6.6 display a certain locality of intensity spots. Due to the limitations of the survey of the system, the most probable causes of these spots are:

- quantisation performed by the detector itself;

- limited resolution of the digital oscilloscope;

- quantisation performed in Origin® as an inevitable step in preparation of a contour plot.

The hourglass shape could perhaps be explained on the basis of nonuniform distribution of quantised samples of sinusoidal time-domain traces—the closer to peaks and troughs, the higher the density of samples, hence the higher density of data points in figures 6.6b and 6.6c. For this very reason the area between two centres of density in those two figures is so sparsely filled. The only significant difference between these two figures is
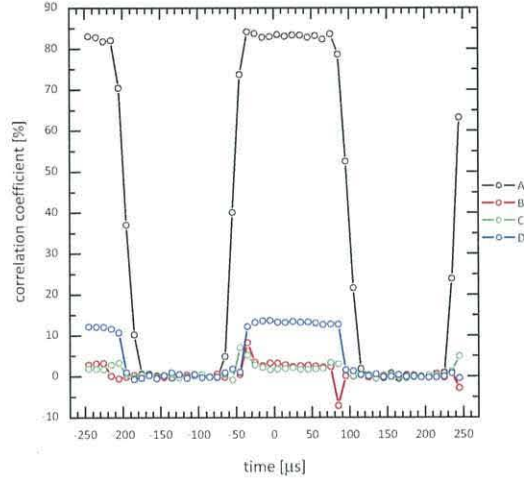
Figure 6.7: Correlation coefficient between ML and SL time-domain traces – Correlation was calculated for consecutive 10 μm slices.

the much greater SL amplitude in the latter case, however, the general distribution of density points is approximately the same. This observation could be substantiated by the fact, that between both measurements the peak in SL spectra did not significantly change its frequency.

Correlation traces are presented in figure 6.7. Trace 'A' gives testimony to high correlation between the lasers over the course of optical injection that reached 82%. The process of synchronisation and desynchronisation is seen to be gradual. Traces 'B' and 'C' display negligible synchronisation in the injection window. Most interesting, however, are the spurts of positive and negative correlation in the order of ±8% during the transition stage between injection and no injection. The fact that trace 'D' reached approximately 12–13% can be used to explain why density plot in figure 6.6d displays a slight ellipticity. All four traces show no synchronisation between the lasers took place when the injection arm was blocked.

Figure 6.8 provides detailed traces of ML and SL optical power. Both lasers oscillate chaotically in figure 6.8a, where they also are synchronised. In figures 6.8b and 6.8c

ML is no longer chaotic, however, SL exhibits a very regular pattern of oscillation at frequencies f_B and f_C, respectively, that correspond to conspicuous peaks in figures 6.5b and 6.5c. Lastly, SL in figure 6.8d is lasing at cw, just like ML, and they are both unsynchronised.

In figure 6.5c, the main frequency peak $f_m = 3.52417$ GHz, the nearest left side peak $f_{m-1} = 3.27789$ GHz, the nearest right side peak $f_{m+1} = 3.76770$ GHz. Therefore, the measured mode spacing amounts to:

$$f_m - f_{m-1} = 246.28 \text{ MHz},$$
$$f_{m+1} - f_m = 243.53 \text{ MHz},$$

which when averaged equals $\overline{f}_{sep} = 244.90$ MHz. To obtain the factual mode number of the highest peak:

$$
\begin{aligned}
m &= \frac{f_m}{\overline{f}_{sep}} \\
&= \frac{3.52417 \cdot 10^9 \, \frac{1}{s}}{244.90 \cdot 10^6 \, \frac{1}{s}} \\
&\approx 14.
\end{aligned}
$$
(6.1)

Knowing values of maximum mode frequency and which mode number it corresponds to allows one to recalculate the value of mode spacing:

$$
\begin{aligned}
f_{sep} &= \frac{f_m}{m} \\
&= \frac{3.52417 \cdot 10^9 \, \frac{1}{s}}{14} \\
&= 251.73 \text{ MHz}.
\end{aligned}
$$
(6.2)

Finally, knowing the value of mode separation allows one to calculate the length of the optical cavity where this frequency is equivalent to the fundamental mode (again
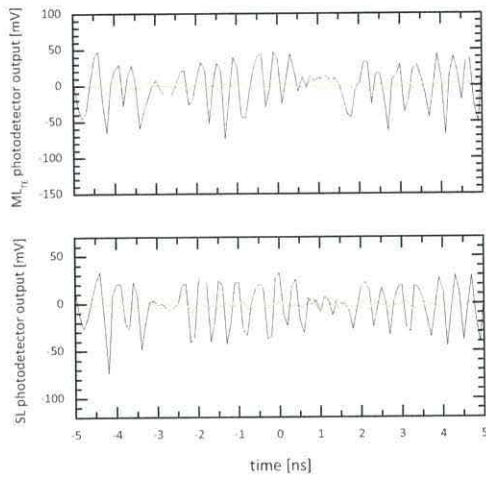
(a) Magnified traces in figure 6.4a.
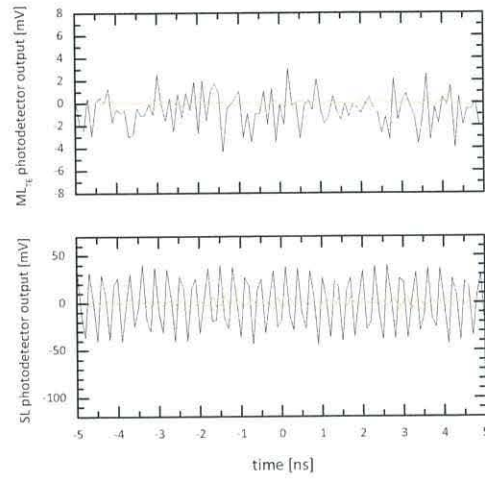
(b) Magnified traces in figure 6.4b.
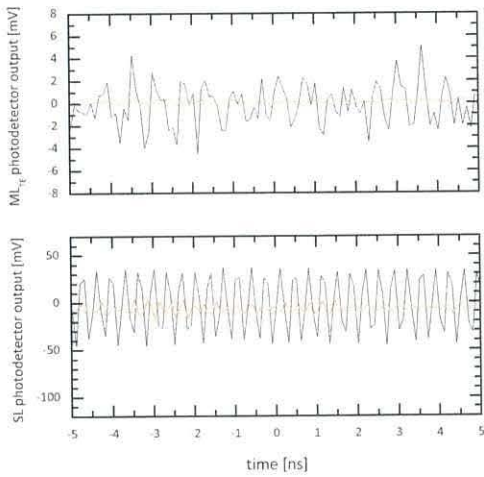
(c) Magnified traces in figure 6.4c.
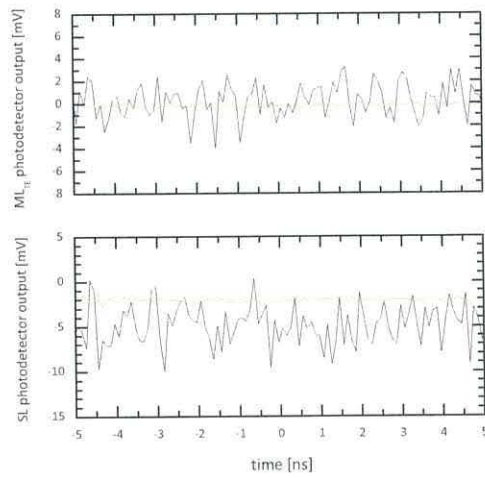
(d) Magnified traces in figure 6.4d.

Figure 6.8: Detailed temporal traces of ML and SL optical power – Vertical scale in each figure corresponds to that of the referenced figure. Detector's typical conversion gain at 850 nm is 300 V/W.

assuming that medium of propagation is essentially air (*i.e.* $n \equiv 1$):

$$
\begin{aligned}
f_{sep} &= \frac{c}{2nL} \\
L &= \frac{c}{2nf_{sep}} \\
&= \frac{299,792,458 \, \frac{m}{s}}{2 \cdot 1 \cdot 251.73 \cdot 10^6 \, \frac{1}{s}} \\
&\approx 59.55 \text{ cm.}
\end{aligned}
\tag{6.3}
$$

This sort of distance from SL would require a reflector to be placed between optical isolators ISO_3 and ISO_4. It is not entirely unreasonable to conclude that back-reflection might have occurred off ISO_3's facet, however, taking into consideration that:

- optical isolators' facets are anti-reflection coated;

- an optical beam confined in this hypothetical cavity would need to traverse from SL through half-wave plate HWP_2 and orthogonally-polarised facet of optical isolator ISO_4 and face more than 40 dB of attenuation,

it casts doubt on this particular explanation. It is further compounded by the fact that figure 6.5d is devoid of such peak. Throughout measurements 'B', 'C', and 'D' the exact same experimental configuration was employed with the only difference being laser's drive current and temperature.

Similarly, it is not inconceivable for the SL to have influenced the ML in spite of attenuation of its field in the injection arm. ML spectra in figures 6.5b and 6.5c do contain a small peak roughly corresponding to the main peak in respective SL's spectra. However, if this really were the case, then those small peaks in ML's spectra would also have appeared in average traces (in green), just like the peaks in SL's spectra. Additionally, SL's field having experienced at least 80 dB of attenuation (two ISOs and possible misalignment) would in such circumstance carry −90 ('C') to −100 dB ('B') of power, at most. It is doubtful that optical injection of this magnitude would exert

meaningful effect on the then solitary ML.

It would thus suggest that the origin of the frequency peak is SL's spectra needs to be looked for in the SL itself.

6.2 Dynamics of TE and TM modes of an ECSLD

The original motivation behind this particular measurement was to investigate whether splitting a laser's TE and TM polarisations (while at the same time subjected to external-cavity optical feedback) would allow use to infer the carrier dynamics from the TM spontaneous emission and thereby construct the chaotic attractor from experimental data. In due course of the experiment the original objective proved to be unrealisable with the employed set-up (for unforeseen reasons) and therefore the focus shifted to an investigation of TM dynamics, which resulted in the observation that the TM mode can, in fact, lase in such a configuration.

It is generally assumed that the TE mode of an SLD is the dominant one, whereas the TM is highly suppressed, firstly due to slightly higher threshold gain, and secondly due to higher reflection penalties of the laser facets. While this assumption is valid for solitary lasers, it will be shown that the TM mode can lase in an ECM configuration [363]. There is no prospect for direct comparison between the results presented in this thesis and those found in published materials [364–372] primarily because no deliberate polarisation rotation was here employed.

Experimental configuration

The experimental set-up is presented in figure 6.9. A single semiconductor laser was used in an external-cavity set-up. A portion of its optical field was diverted via the BS, through the PBS to the detectors. The NDF_1 was used to adjust and control the laser's optical feedback rate, the NDF_2 was used to adjust the optical power so that it
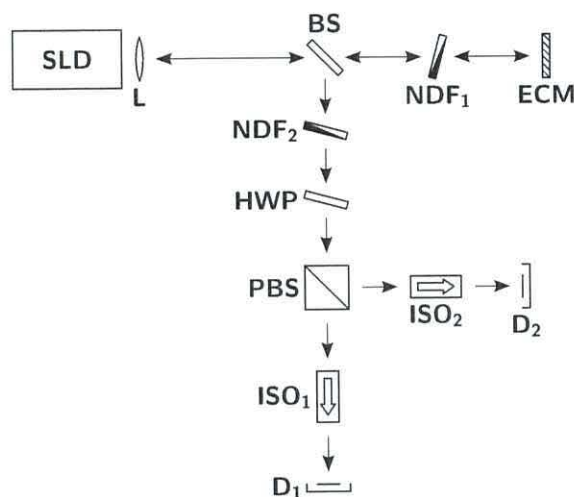
Figure 6.9: Experimental set-up – BS (beam splitter), D (detector), ECM (external-cavity mirror), HWP (half-wave plate), ISO (optical isolator), L (collimating lens), NDF (natural density filter), PBS (polarising beam-splitter).

would not exceed the limit imposed by the detectors. The HWP was used to rotate the incoming optical beam to align it with the PBS thereby assuring that the subsequent split into two polarisations was optimised. Optical isolators were used to minimise back-reflection from the detectors. Detector D_1 was used to record the TE polarisation, whereas D_2 was used to record the TM polarisation. For the technical details regarding the employed components, refer to section 3.1.

Basic experimental procedure

The laser was rendered chaotic (with parameters $I = 40.00$ mA and $T = 20.62$ °C) and left undisturbed for 30 minutes. Then, a single measurement of laser's TE mode as a function of drive current was performed (see figure 6.10). Later, three analogous measurements of laser's TM mode were performed with different values of optical feedback rate (see figure 6.11). Three different strengths of optical feedback rate—low, medium, and high—were effected via the rotation angle at which NDF_1 was fixed: 60, 100, and 133 degrees, respectively.

The optical spectrum was recorded along with the optical power via the use of a fibre splitter connected to the detector D_1 (for TE modes), or D_2 (for TM modes). Every measurement was followed by an idle stage lasting 30 minutes when the laser's parameters were reset to the above mentioned values.

The optical spectra obtained from the optical spectrum analyser were aggregated to form contour plots as a function of laser's drive current (as presented in figures 6.10a, 6.11a, 6.11b, and 6.11c). Each optical intensity–drive current (L–I) plot (as presented in figures 6.10b, 6.11d, 6.11e, and 6.11f) was recorded simultaneously with its corresponding optical spectrum.

TE modes of an ECSLD

Typical characteristics of a TE mode of a semiconductor laser subject to external optical feedback are presented in figure 6.10.

(a) Optical power spectrum [dBm].
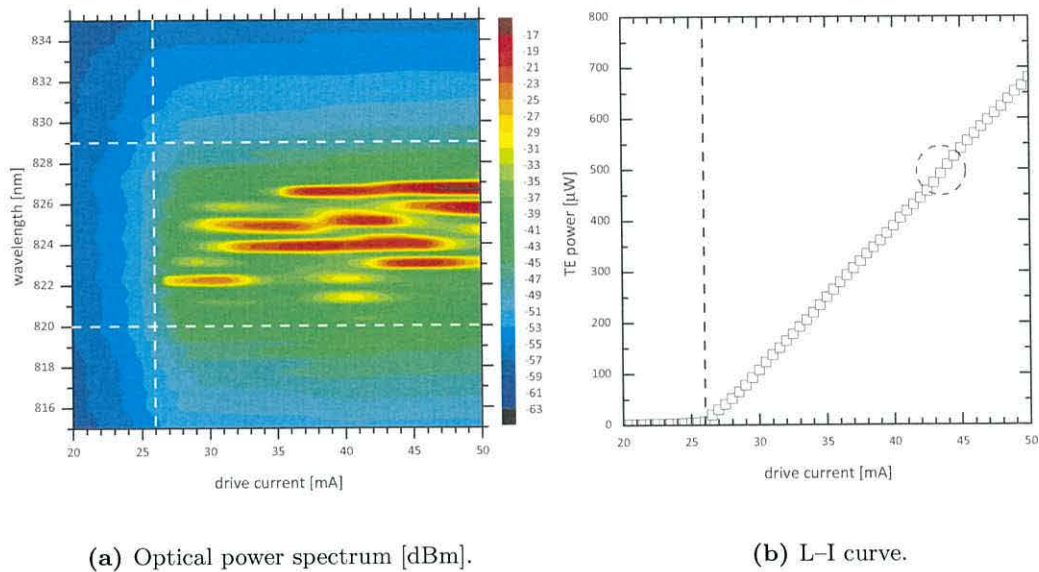
(b) L–I curve.

Figure 6.10: Contour plot of optical power spectrum and L–I curve for TE polarisation at high optical feedback rate – The vertical dashed lines in both figures signify the boundary between regimes of spontaneous and stimulated emission. The horizontal dashed lines in the contour plot are provided as a visual cue and highlight where the majority of power in the spectrum is.

154

As can be appreciated in figure 6.10a, the laser's spectral components experienced a shift towards longer wavelengths with increasing current—the first major mode emerged at *ca.* 822 nm and the most significant mode at 827 nm. Another feature present in the figure is that between 41 and 45 mA there is a region where more modes were supported; this fact was accompanied by a reduction in power and a slight 'kink' in L–I curve, as indicated by the dashed circle in figure 6.10b.

TM modes of an ECSLD

The result of the first measurement (at a low value of optical feedback), as presented in figure 6.11a, revealed the presence of two readily discernible regimes of operation:

- spontaneous emission with a broad, but flat, spectrum (below 25.5 mA);

- multi-peak configuration, *i.e.* chaos (above 25.5 mA).

The modal structure in the figure also reflects this change, with the number of supported modes progressing from one to four.

By moving to the second measurement (at a medium value of optical feedback), as presented in figure 6.11b, a third, intermediate, regime emerged. This new regime is characterised by its pattern of emission that supports one mode at a time, however, that mode is not stable and can experience hopping whose frequency is dependent upon optical feedback level [373].

The final, third, measurement (at a high value of optical feedback), as presented in figure 6.11c, represents the case where all three regimes are clearly defined.

Similarly to 'kink' seen in figure 6.10b, a significantly more pronounced change in gradient (or actually, quantum efficiency [275]) can be appreciated in L–I curve in figure 6.11d; the cause of this phenomenon is competition between external-cavity modes. A characteristic point of transition (*i.e.* threshold) between the regime of spontaneous

emission (R_1) and regime of stimulated emission (R_2) is present in the figure thereby illustrating that TM mode did, in fact, lase in the presence of external-cavity mirror.

Figure 6.11e gives an indication of modal instability present in the intermediate (R_2) region. The value of threshold current is seen to decrease as a result of increased optical feedback; it decreases even further in figure 6.11f for a higher value of optical feedback. The nonlinear destabilisation seen in R_2 in figure 6.11f is possibly due to mode competition.

The $R_2 \rightarrow R_3$ region transition in figure 6.11b is more abrupt than the $R_1 \rightarrow R_2$ transition in figure 6.11a. Furthermore, the $R_2 \rightarrow R_3$ transition in figure 6.11c is the most abrupt of the three.

In spite of varying the amount of optical feedback (and also affecting the external-cavity resonance condition), the most significant mode throughout the three measurements was the one at 826 nm. According to the Lang–Kobayashi model, with increasing feedback, the laser would try to stabilise itself on one of the longitudinal modes, and in fact, it has been shown [290] that laser will lock on to the mode with the lowest linewidth.

To summarise, the evidence for TM lasing is:

- presence of visually discernible threshold current;

- visually discernible modal structure.

The reason for the shift of the threshold current towards lower values of drive current with an increase in optical feedback rate (the leftmost vertical dashed line in figures 6.11e and 6.11f moving towards the *left*) could be explained on the basis of accompanying increase in number of photons fed back in to, and circulating in the laser cavity thereby contributing to population inversion, and finally recombining owing to stimulated emission.
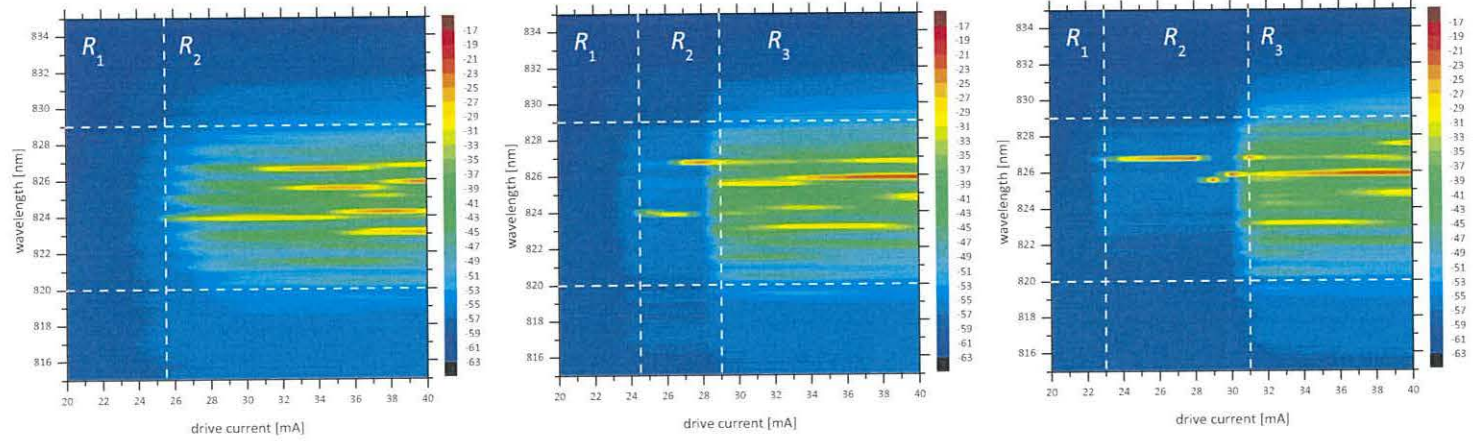
(a) Optical power spectrum for low value of optical feedback.

(b) Optical power spectrum for medium value of optical feedback.

(c) Optical power spectrum for high value of optical feedback.
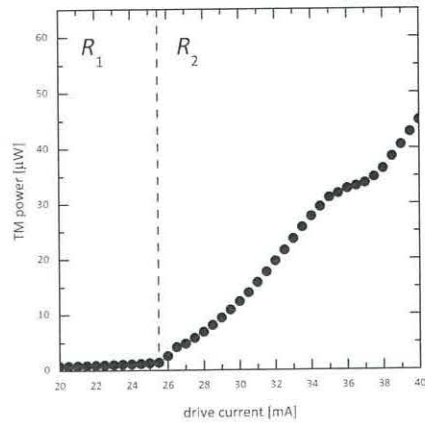
(d) L–I curve for low value of optical feedback.
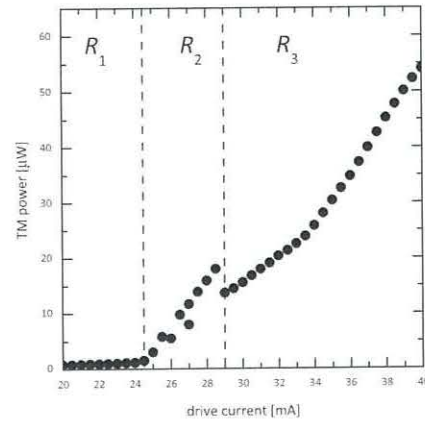
(e) L–I curve for medium value of optical feedback.
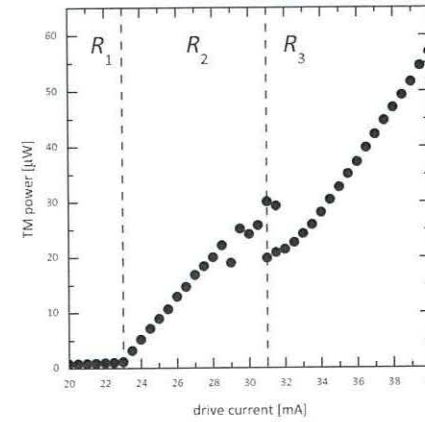
(f) L–I curve for high value of optical feedback.

Figure 6.11: Contour plots of optical power spectrum and L–I curves for TM polarisation at three levels of optical feedback – The vertical dashed lines in the figures signify the boundary between regimes. The horizontal dashed lines in the contour plots are provided as a visual cue and highlight where the majority of power in the spectrum is. The colour scale denotes optical power in [dBm].

The reason for the shift of onset of 'coherence collapse' towards higher values of drive current with increase in optical feedback rate (the rightmost vertical dashed line in figures 6.11e and 6.11f moving towards the *right*) could be explained on the basis of suppression of that regime with the increase of the drive current, as presented in [300] and in figure 2.3.

One can also notice a shift of ECSLD's spectrum towards longer wavelengths with increasing optical feedback (compare figures 6.11a, 6.11b, and 6.11c). This phenomenon is consistent with previous results [87, 88] where an increase of photon density in laser cavity decreased the number of carriers. This then contributed to an increase in value of refractive index thereby increasing the effective length of laser cavity, hence the longer wavelengths satisfying constructive resonance condition inside that cavity.

6.3 Conclusions

Two experimental surveys were conducted—one revolved around the concept of chaos-synchronisation through optically chopped injection, while the other focused on aspects of chaos-synchronised TM polarisation of an ECSLD and its dynamic properties.

Section 6.1 is dedicated to the presentation of a certain switching dynamics whereby chaotic SL is subjected to optically chopped injection from a solitary ML. Four sets of SL's parameters were investigated and their effect on SL's dynamics was analysed. In particular, for certain parameter values, a previously unreported feature has been observed—in due course of the experiment, SL's time-domain optical power plotted against ML's formed a shape akin to an hourglass. Such a shape can most probably be attributed to the dominating frequency peaks in the SL's spectrum (and clearly visible sinusoidal oscillation in figures 6.8b and 6.8c) conjoined with lack of synchronisation between the two lasers, hence the generally vertical shape as opposed to diagonal in synchronisation diagram. During the analysis, the possibility of unintended reflections

was eliminated. Conversely, electrical character has not been ruled out. As an unfortunate consequence, however, the origin of said resonance peaks and selective frequency amplification remains elusive. Further experimental surveys into the boundaries of the parameter space would be necessary to allow for conclusive statements to be made pertaining to the extent of the reported phenomenon.

Section 6.2 raises an issue of lasing of a TM mode in a laser subject to direct (as opposed to rotated) optical feedback. Notwithstanding the fact that TM mode had been shown by other research groups to be able to sustain lasing, it is in this thesis where it is presented for the first time[2] that TM mode can also lase in the regime of 'coherence collapse'. Focus is then moved onto the dynamics of said mode. Optical power spectrum along with an L–I curve is recorded for TE polarisation. In a separate measurement, TM polarisation was investigated for three different values of optical feedback. Limited comparison can be drawn between polarisations as only one experiment involving the TE mode was performed. The TE mode was stable, developed a pattern of oscillation and mostly retained it throughout the whole experiment. As for the TM mode, it was not found to be very stable since it developed a single stable solution first, then hopped, and finally developed a multi-peak pattern, as well. Physical origin of that hopping remains elusive and would require further experimental investigation in order to be unravelled. The reason for the instabilities seen in figure 6.11 could be explained as manifestation of regime II or III of the injection strength vs external cavity length diagram (see figure 2.3), where the laser is experiencing mode-hopping, whose frequency is dependent upon these two parameters. On the other hand, the data gathered here are not inconsistent with the phenomenon of spatial hole burning, whereby spectral power density can lead to a significantly lower gain of the dominant mode thereby favouring neighbouring modes now experiencing higher gain. Thirdly, the unstable features present in figures 6.11e and 6.11f could as well be interpreted as a manifestation

---

[2]At least to the best extent of the author's knowledge.

of hysteresis [374, 375]. Finally, the characteristic traits were identified in TM mode's dynamics that proved that it indeed experienced lasing.

Chapter 7

Conclusions

7.1   Review of the Thesis

Chapter 1 contains a broad ranging introduction into chaos communications as a scholarly field of research and the principal points of interest of this thesis. The historical overview in this chapter was split into three sections—the history of the development of chaos communications itself, as well as, that of cryptography and steganography—two disciplines from which chaos communications draws inspiration and on which it is based. The typical configurations employed in experimental and numerical investigations of chaos communications were also presented.

A brief account of the history of lasers, with particular attention paid to the development of semiconductor lasers, was provided in chapter 2 along with a presentation of semiconductor laser diodes' (SLDs') characteristic parameters in comparison to other laser types. The core of this chapter, however, was devoted to the theoretical foundation and the mathematical framework used in addressing the physical phenomena pertaining to the emission of radiation by a semiconductor laser. To this end, the derivation of the commonly used rate equations was performed starting from Maxwell's equations and stating assumptions and limitations along the way. Additional mathematical apparatus

was introduced to allow for the appropriate treatment of dynamical effects present in SLDs subject to external optical perturbation. Thus, the concept of chaos was introduced and expanded into the Lorenz–Haken model. In the final part of the derivation, the extended Lang–Kobayashi model was presented—this model was used to describe the dynamical phenomena that emerge in a configuration where an SLD is subjected to external-cavity feedback or to optical injection from another laser. The regimes of feedback-induced dynamics were presented and defined. The chapter concludes with a discussion of the implications of numerically solving the Lang–Kobayashi model and presents the default parameter values used throughout this thesis.

The first experimental results are contained in chapter 3. The first part of this chapter is concerned with the initial presentation of the experimental methodology and an investigation of the robustness of the chaos synchronisation to parameter mismatch in an open-loop configuration. This mismatch was introduced into the *a priori* synchronised system in the form of drive current and device temperature. Aggregated cross-correlation plots were used to present the evolution of the correlation between the lasers as a function of parameter mismatch. A correspondence between the output power fluctuations observed experimentally and those reported in published materials has been observed. For the chosen parameter range, the ML and SL temperature plots were found to be almost symmetrical. A relation between the parameter mismatch and the amplification or attenuation of spectral components has also been observed. In short, the results obtained are in line with the theoretical predictions of earlier published work. This chapter also dealt with the question of the message transmission using the Chaos Modulation scheme in an open-loop configuration. Additionally, an attempt at naïve interception of that message was performed. The message was introduced at four frequencies and six power levels in order to ascertain whether it would give rise to conspicuous frequency components in the power spectrum. It was found that for the message to remain hidden its rf power should remain below -25 dBm, a value

lower that previously reported, which may be explained by lower dimensionality of chaos, as the lasers operated in the LFF regime. Degradation of synchronisation quality was observed for increasing levels of message power because the modulation amplitude drove the ML current below threshold. Lastly, it was found that certain details of ML's configuration (such as external-cavity round-trip time) could be easily deducted by an attacker. Having collected enough temporal data, an attacker could also estimate the modulation depth of the hidden message. These factors led to the conclusion that transmission of sensitive information in LFF regime is inherently insecure.

Attention then shifted from experimental investigations to the numerical simulation. The aim of chapter 4 was to introduce and present the numerical technique used to solve the Lang–Kobayashi model. The effect of the ramping time duration on SL's dynamics was investigated with the aim of examining the locking mechanism. In order to uncover the underlying trends in the dynamics, which are masked by high-amplitude chaotic oscillation, averaging of multiple simulations (run with random initial conditions) were introduced. As a result of the analysis, 'kinks' in the average trace of the phase difference and SL's carriers were observed and determined to be independent of initial conditions. Furthermore, the single-run analysis revealed a possibility of using optical phase as a carrier of a hidden message; it was found that such a message could be potentially transmitted at a frequency of up to 37 GHz, which is significantly higher than that of 1 GHz reported in the literature. Then, the difference between the dynamics triggered by two values of carrier lifetime was investigated. The lower value of τ_n proved to give rise to more stable dynamics and ease of obtaining phase-lock. The higher value of τ_n not only made synchronisation take longer to stabilise, but also made it easier to lose the existing synchronisation. This analysis was also conducted at various levels of optical injection. As a result, three regimes of disparate synchronisation quality were observed. The positive and negative 'kinks' were again observed in the average traces of the phase difference, however in this survey their temporal position

and magnitude were found to be dependent upon the injection strength. The effect of injection strength was investigated from the perspective of the SL's average spectra and spectral transfer function (STF). The development of peaks in the STF was observed along with development of a second prominent peak in SL's spectrum.

Numerical parameter-space exploration was also employed in chapter 5, where the investigation was motivated by the desire to examine how variations in the intrinsic parameters of an SLD affected the synchronisation process. In the first part, three values of carrier lifetime were chosen. It was found that, in general, varying the value of τ_n did not affect the synchronisation process in a significant manner (in spite of having varied τ_n by 100% from 2 ns to 4 ns); it did, nonetheless, affect the SL's spectrum by shifting the peak STF and altering the overall spectral profile. Also, as indicated by the Lang–Kobayashi model equations, power levels were decreased by increasing carrier lifetime. Similarly to the results obtained in chapter 4, the lower value of τ_n was found to render the lasers more stable. Conspicuous peaks in the average spectra of SL optical power were found to correspond to relaxation oscillation frequency and its higher harmonics, which explains their preferential amplification. Variation in the linewidth enhancement factor had little effect on the synchronisation, at least for the values considered in this thesis. The value of α did, nevertheless, affect the number of suppressed SL carriers, and (to a lesser extent) the SL optical power in the full-injection window. For the values considered, three ranges of dynamical properties were observed and defined. The instant in time when the phase lock takes place was found to be independent of the value of α. External optical injection was found to exert a stabilising effect for all values of α, but in particular in the cases characterised by pre-injection oscillations. From the phase-plots it was concluded that laser synchronisation is indeed more feasible for the lower values of α, which fits well with the theoretical prediction that reducing α reduces the complexity of the chaos. Lastly, increasing α resulted in SL's spectrum developing a pronounced secondary peak around 21–22 GHz, which

translated into a frequency shift and amplification of the peak in the STF plot.

The purpose of chapter 6 was to further experimentally investigate the dynamical properties based on the approach presented in chapter 3. The initial focus was on the dynamics of SL exposed to optical injection subjected to periodic perturbation introduced by an optical chopper. Initially, both lasers were set-up to achieve chaos synchronisation. Later, as the ML's external-cavity mirror was removed, switching transients between regimes of injection locking and self-feedback were observed in the time-domain traces of SL's optical power. This also led to the discovery of a previously unreported phenomenon that manifested itself in the form of an hourglass shaped ML–SL phase portrait, as well as, a spectrum dominated by a peak, accompanied by its higher and lower harmonics. The possibility of an optical origin of this peak, emerging through a hypothetical optical resonance cavity, was investigated and rejected. Since only temperature and drive current were varied, it is therefore postulated that this phenomenon stems from the laser's inherent dynamics. The second part of this chapter reports on experimental investigation of interplay between TE and TM modes of an external-cavity semiconductor laser diode. Measurements of the TE mode optical spectrum and optical power were performed, along with further measurements of the TM mode. It was found that the TM mode in such a basic, optical self-feedback, configuration did in fact lase. Furthermore, an analysis of development of frequency components with drive current was performed for three levels of optical feedback as a consequence of an observation of an abrupt transition of the TM optical power. The observed TE mode was stable, whereas the TM mode was seen to experience hopping and discontinuities in the L–I plots. As the TM mode was investigated for three levels of optical feedback, three possible explanations are postulated. Firstly, this instability could be a result of the laser moving from II to III regime of injection strength. Secondly, it is not incongruent to suggest that the observed mode-hopping came as a result of spatial hole burning. Thirdly, the L–I traces could also be interpreted as evidence of

hysteresis.

7.2 Future work

During the course of this thesis work certain research topics were identified as having the potential for further study and development. They are listed and organised with respect to relevant chapters.

Chapter 3

An automated data acquisition procedure could be incorporated in order to further investigate the effect of temperature detuning on STFs seen in section 3.1. This approach could possibly lead to explanation of amplification of certain spectral components.

Chapter 4

The positive and negative 'kinks' seen in carrier ratio figures in sections 4.2.2 and 4.2.3 need further investigation. At this stage, there is not enough data to ascertain what the physical phenomenon behind these 'kinks' is. Aside from the 'kinks' lies the question of double gradients, also seen in the figures of carrier ratio. In order to characterise this feature, one would need to conduct additional investigations of carrier dynamics, *e.g.* by keeping the *gradient* of the ramping function constant and vary:

- the κ_c^{max} and, consequently, vary also either the T_1 & T_4, or the T_2 & T_3 pair;

- the T_1 & T_4 and the T_2 & T_3 pairs while keeping the κ_c^{max} constant.

Chapter 5

The multiple averaging approach adopted in this chapter could be applied to investigate the effect of material gain, g, variation. However, for this approach to yield sensible

results, it is postulated that the simplistic linear gain model in the Lang–Kobayashi model would need to be enhanced to account for effects such as spatial hole burning.

A thorough investigation of the effect of photon lifetime could prove beneficial, as it was reported [111] that photon lifetime plays the most critical role in synchronisation quality in case of parameter mismatch. It is, nonetheless, noted that such investigation would be inherently mired in difficulties—altering value of τ_{ph} would imply changing the values of cavity reflectivity coefficients, r, which would in turn affect other aspects of device performance.

In general, automated sweeps could be adopted to extract material data from various semiconductor structures. This could then be used to adjust the Lang–Kobayashi model in order to minimise discrepancies between numerical and experimental results.

Chapter 6

The switching dynamics and the hourglass shape reported in section 6.1 would most certainly qualify for further experimental investigation. The physical origin of the peaks in ML's spectrum remains elusive. The origin of certain features in dynamics could not be attributed to any optical resonance cavity.

Lastly, the most intriguing feature presented in chapter 6 is the lasing of TM polarisation of an external-cavity SLD subject to optical feedback, as presented in section 6.2. The most immediate extension of that experimental investigation would entail simultaneous recording of both, TE and TM polarisations, along with optical power and optical spectrum for various values of feedback rate.

Bibliography

[1] S. Singh. *The Code Book*. Fourth Estate Ltd, London, UK, 1999. ISBN 1-85702-879-1.

[2] D. Kahn. *The Codebreakers: The Comprehensive History of Secret Communication from Ancient Times to the Internet*. Scribner, New York, NY, USA, 1996. ISBN 0-684-83130-9.

[3] I. Cox, M. Miller, J. Bloom, J. Fridrich, and T. Kalker. *Digital Watermarking and Steganography*. The Morgan Kaufmann Series in Multimedia Information and Systems. Morgan Kaufmann Publishers, Burlington, MA, USA, 2nd edition, 2007. ISBN 0-123-72585-2.

[4] G. Kipper. *Investigator's Guide to Steganography*. Auerbach Publications, 2003. ISBN 0-849-32433-5.

[5] L. B. Alberti. De cifris, 1466.

[6] L. B. Alberti. *A Treatise on Ciphers*. Galimberti Tipografi Editori, Torino, 1997. trans. by A. Zaccagnini.

[7] B. de Vigenère. *Traicté des chiffres ou secrètes manières d'escrire*. Abel l'Angelier, Paris, France, 1586.

[8] A. Kerckhoffs. La cryptographie militaire. *Journal des sciences militaires*, 9:5–38, January 1883.

[9] A. Kerckhoffs. La cryptographie militaire. *Journal des sciences militaires*, 9:161–191, February 1883.

[10] C. E. Shannon. Communication theory of secrecy systems. *Bell Syst. Tech. J.*, 28(4):656–715, 1949. URL http://netlab.cs.ucla.edu/wiki/files/shannon1949.pdf.

[11] C. E. Shannon. A mathematical theory of communication. *Bell Syst. Tech. J.*, 27:379–423, 623–656, July–October 1948. URL http://plan9.bell-labs.com/cm/ms/what/shannonday/shannon1948.pdf.

[12] I. Peterson. *The Jungles of Randomness: A Mathematical Safari*. John Wiley & Sons, New York, NY, USA, 1997. ISBN 0-471-16449-6.

[13] W. Kozaczuk. *Enigma: How the German cipher was broken, and how it was read by the Allies in World War Two*. Foreign Intelligence Book Series. University Publications of America, Frederick, MD, USA, 1984. ISBN 0-313-27007-4.

[14] H. Sebag-Montefiore. *Enigma: The Battle for the Code*. John Wiley & Sons, 2001. ISBN 0-471-40738-0.

[15] D. Kahn. *Seizing the Enigma: The Race to Break the German U-Boat Codes, 1939–1943*. Houghton Mifflin, Boston, MA, USA, 1991. ISBN 0-395-42739-8.

[16] W. Diffie and M. E. Hellman. New directions in cryptography. *IEEE Trans. Inform. Theory*, 22(6):644–654, November 1976.

[17] R. L. Rivest, A. Shamir, and L. Adleman. A method for obtaining digital signatures and public-key cryptosystems. *Commun. ACM*, 21(2):120–126, February 1978.

[18] S. Wiesner. Conjugate coding. *ACM SIGACT News*, 15 (1):78–88, 1983. Original manuscript written ca. 1970.

[19] C. H. Bennett and G. Brassard. Quantum cryptography: Public key distribution and coin tossing. In *Proc. IEEE Int. Conf. Computers Syst. Signal Processing*, pages 175–179, Bangalore, India, December 1984.

[20] Q. Liu and S. Sauge. How you can build an eavesdropper for a quantum cryptosystem. In *26th Chaos Communication Congress*, 2009. URL http://events.ccc.de/congress/2009/Fahrplan/events/3576.en.html.

[21] I. Gerhardt and V. Makarov. How we eavesdropped 100% of a quantum cryptographic key. In *Hacking at Random*, 2009. URL https://har2009.org/program/events/168.en.html.

[22] L. Lydersen, C. Wiechers, C. Wittmann, D. Elser, J. Skaar, and V. Makarov. Hacking commercial quantum cryptography systems by tailored bright illumination. *Nat. Photon.*, 4(10):686–689, October 2010.

[23] Z. L. Yuan, J. F. Dynes, and A. J. Shields. Avoiding the blinding attack in QKD. *Nat. Photon.*, 4(12):800–801, December 2010.

[24] R. P. Feynman. Simulating physics with computers. *Int. J. Theor. Phys.*, 21(6–7):467–488, June 1982.

[25] D. Z. Albert. Bohm's alternative to quantum mechanics. *Sci. Am.*, 270(5):58–67, May 1994.

[26] D. Deutsch. Quantum theory, the Church–Turing principle and the universal quantum computer. In *Proc. R. Soc. Lond.*, volume 400 of *A*, pages 97–117, July 1985.

[27] D. Deutsch. Quantum computational networks. In *Proc. R. Soc. Lond.*, volume 425 of *A*, pages 73–90, September 1989.

[28] A. Politi, J. C. F. Matthews, and J. L. O'Brien. Shor's quantum factoring algorithm on a photonic chip. *Science*, 325(5945):1221, September 2009.

[29] L. M. K. Vandersypen, M. Steffen, G. Breyta, C. S. Yannoni, M. H. Sherwood, and I. L. Chuang. Experimental realization of Shor's quantum factoring algorithm using nuclear magnetic resonance. *Nature*, 414(6866):883–887, December 2001.

[30] C.-Y. Lu, D. E. Browne, T. Yang, and J.-W. Pan. Demonstration of a compiled version of Shor's quantum factoring algorithm using photonic qubits. *Phys. Rev. Lett.*, 99(25):250504, December 2007.

[31] B. P. Lanyon, T. J. Weinhold, N. K. Langford, M. Barbieri, D. F. V. James, A. Gilchrist, and A. G. White. Experimental demonstration of a compiled version of Shor's algorithm with quantum entanglement. *Phys. Rev. Lett.*, 99(25):250505, December 2007.

[32] D. Hanneke, J. P. Home, J. D. Jost, J. M. Amini, D. Leibfried, and D. J. Wineland. Realization of a programmable two-qubit quantum processor. *Nat. Phys.*, 6(1):13–16, November 2009.

[33] P. W. Shor. Algorithms for quantum computation: Discrete logarithms and factoring. In *Proc. 35th Ann. Symp. Foundations Comp. Sci.*, pages 124–134, Santa Fe, NM, USA, November 1994.

[34] L. K. Grover. A fast quantum mechanical algorithm for database search. In *Proc. 28th Ann. ACM Symp. Theory Comput.*, pages 212–219, Philadelphia, PA, USA, May 1996.

[35] Hong Zhu. Survey of computational assumptions used in cryptography broken or not by Shor's algorithm. Master's thesis, McGill University, Montréal, Canada, School of Computer Science, December 2001. URL http://crypto.cs.mcgill.ca/~crepeau/PDF/memoire-hong.pdf.

[36] M. A. Barreno. The future of cryptography under quantum computers. Senior thesis, Dartmouth College of Computer Science, July 2002. URL http://www.cs.dartmouth.edu/~sws/theses/marco.pdf.

[37] M. S. Brown. Classical cryptosystems in a quantum setting. Master's thesis, University of Waterloo, Ontario, Canada, April 2008. URL http://arxiv.org/abs/quant-ph/0404061v1.

[38] J. Buchmann, C. Coronado, M. Doering, D. Engelbert, C. Ludwig, R. Overbeck, A. Schmidt, U. Vollmer, and R.-P. Weinmann. Post-quantum signatures, September 2004. URL http://itslab.csce.kyushu-u.ac.jp/iwap04/PostQuantumSignatures.pdf.

[39] D. J. Bernstein, J. Buchmann, and E. Dahmen. Post-quantum cryptography. Springer, Berlin, Germany, 2009. ISBN 3-540-88701-6.

[40] E. Cole. Hiding in Plain Sight: Steganography and the Art of Covert Communication. John Wiley & Sons, 2003. ISBN 0-471-44449-9.

[41] R. J. Anderson. Why cryptosystems fail. Commun. ACM, 37(11):32–40, November 1994.

[42] J. Wilkins. Mercury, or the Secret and Swift Messenger: Shewing How a Man may with Privacy and Speed communicate his Thoughts to a Friend at any distance. I. Norton, London, UK, 1st edition, 1641.

[43] J. Wilkins. Mercury: or the Secret and Swift Messenger, volume 6 of Foundations of Semiotics. John Benjamins Publishing, 1984. ISBN 9-027-23276-8. Reprinted from the 3rd edition.

[44] F. A. P. Petitcolas, R. J. Anderson, and M. G. Kuhn. Information hiding—A survey. In IEEE Proc., volume 87, pages 1062–1078, July 1999.

[45] G. W. W. Stevens. Microphotography: photography and photofabrication at extreme resolution. John Wiley & Sons, New York, NY, USA, 2nd edition, 1968.

[46] G. Tissandier. Les Merveilles de la Photographie. Bibliothèque des merveilles. Librairie Hachette et cie, Paris, France, 1874.

[47] J. D. Hayhurst. The pigeon post into Paris 1870–1871. Ashford, Middlesex, 1970.

[48] B. Newman. Secrets of German Espionage. The Right Book Club, London, UK, 1940.

[49] J. E. Hoover. The enemy's masterpiece of espionage. Reader's Digest, 48:49–53, April 1946.

[50] R. J. Anderson and F. A. P. Petitcolas. On the limits of steganography. IEEE J. Sel. Areas Commun., 16(4):474–481, May 1998.

[51] K. Gopalan. Audio steganography using bit modification. In Proceedings of the 2003 International Conference on Multimedia and Expo, volume 2, pages 629–632, Washington, DC, USA, July 2003. IEEE Computer Society.

[52] M. Qiao, A. H. Sung, and Q. Liu. Steganalysis of MP3Stego. In IEEE - INNS - ENNS International Joint Conference on Neural Networks, pages 2566–2571, Los Alamitos, CA, USA, June 2009. IEEE Computer Society.

[53] Changyong Xu, Xijian Ping, and Tao Zhang. Steganography in compressed video stream. In Int. Conf. Innovative Comput. Inf. Control, volume 1, pages 269–272, Los Alamitos, CA, USA, August–September 2006.

[54] N. F. Johnson and S. Jajodia. Exploring steganography: Seeing the unseen. Computer, 31(2):26–34, February 1998.

[55] H. Noda, M. Niimi, and E. Kawaguchi. High-performance JPEG steganography using quantization index modulation in DCT domain. Patt. Recogn. Lett., 27(5):455–462, April 2006.

[56] M. L. BenSaad and X.-M. Sun. Techniques with statistics for web page watermarking. In Proceedings of World Academy of Science, Engineering and Technology, volume 6, pages 300–303, June 2005.

[57] C. H. Rowland. Covert channels in the TCP/IP protocol suite. First Monday, 2(5), May 1997. URL http://firstmonday.org/htbin/cgiwrap/bin/ojs/index.php/fm/article/view/528/449.

[58] T. Sohn, J.-T. Seo, and J. Moon. Information and Communications Security, chapter A study on the covert channel detection of TCP/IP header using support vector machine, pages 313–324. Lecture Notes in Computer Science. Springer, Berlin, Germany, 2003. ISBN 978-3-540-20150-2.

[59] S. J. Murdoch and S. Lewis. Embedding covert channels into TCP/IP. In Information Hiding: 7th International Workshop, volume 3727 of Lecture Notes in Computer Science, pages 247–261, 2005.

[60] S. Cabuk, C. E. Brodley, and C. Shields. IP covert channel detection. ACM Transactions on Information and System Security, 12(4):22, April 2009.

[61] M. Bennett, M. F. Schatz, H. Rockwood, and K. Wiesenfeld. Huygens's clocks. Proc. R. Soc. Lond., 458(2019):563–579, March 2002.

[62] I. I. Blekhman. Synchronization in Science and Technology. ASME Press Translations. American Society of Mechanical Engineers, New York, NY, USA, 1988. ISBN 0-791-80003-2.

[63] A. Pikovsky, M. Rosenblum, and J. Kurths. Synchronization: A Universal Concept in Nonlinear Sciences. Cambridge Nonlinear Science Series. Cambridge University Press, 2003. ISBN 0-521-53352-X.

[64] A. L. Fradkov and B. Andrievsky. Synchronization and phase relations in the motion of two-pendulum system. Int. J. Nonlinear Mech., 42(6):895–901, July 2007.

[65] J. H. Tiner. Isaac Newton: Inventor, Scientist, and Teacher. Sowers Series. Mott Media, 1984. ISBN 0-915-13406-3.

[66] K. F. Sundman. Mémoire sur le problème de trois corps. Acta Math., 36(1):105–179, December 1913.

[67] Q.-D. Wang. The global solution of the N-body problem. Celest. Mech. Dyn. Astron., 50(1):73–88, March 1990.

[68] W. K. Heisenberg. Über den anschaulichen Inhalt der quantentheoretischen Kinematik und Mechanik. Z. Phys., 43(3–4):172–198, March 1927.

[69] E. H. Kennard. Zur Quantenmechanik einfacher Bewegungstypen. Z. Phys., 44(4–5):326–352, April 1927.

[70] A. Einstein. Zur Elektrodynamik bewegter Körper. Ann. Phys., 322(10):891–921, 1905.

[71] A. Einstein. Kosmologische Betrachtungen zur allgemeinen Relativitätstheorie. *Sitzungsber. Preuss. Akad. Wiss.*, pages 142–152, 1917.

[72] T. Yamada and H. Fujisaka. Stability theory of synchronized motion in coupled-oscillator systems. II. *Prog. Theor. Phys.*, 70(5):1240–1248, November 1983.

[73] T. Yamada and H. Fujisaka. Stability theory of synchronized motion in coupled-oscillator systems. III. *Prog. Theor. Phys.*, 72(5):885–894, November 1984.

[74] V. S. Afraimovich, N. N. Verichev, and M. I. Rabinovich. Stochastic synchronization of oscillations in dissipative systems. *Izv. Vyssh. Uchebn. Zaved. Radiofiz.*, 29(9):1050–1060, 1986.

[75] L. M. Pecora and T. L. Carroll. Synchronization in chaotic systems. *Phys. Rev. Lett.*, 64(8):821–824, February 1990.

[76] S. H. Strogatz. Nonlinear Dynamics and Chaos: Part 1—Chaotic Waterwheel, . URL http://www.youtube.com/watch?v=7iNCfNBEJHo. Retrieved on 2010-02-10.

[77] S. H. Strogatz. Nonlinear Dynamics and Chaos: Part 2—Double Pendulum, . URL http://www.youtube.com/watch?v=anwl6OZ1UuQ. Retrieved on 2010-02-10.

[78] S. H. Strogatz. Nonlinear Dynamics and Chaos: Part 3—Airplane Wing Vibrations, . URL http://www.youtube.com/watch?v=_Ys8qGxr--M. Retrieved on 2010-02-10.

[79] S. H. Strogatz. Nonlinear Dynamics and Chaos: Part 4—Chemical Oscillators, . URL http://www.youtube.com/watch?v=8R33KWPmqlo. Retrieved on 2010-02-10.

[80] S. H. Strogatz. Nonlinear Dynamics and Chaos: Part 5—Synchronized Chaos and Private Communications, . URL http://www.youtube.com/watch?v=J-ca_bqWp4I. Retrieved on 2010-02-10.

[81] S. H. Strogatz. Nonlinear Dynamics and Chaos: Part 6a—Musical Variations from a Chaotic Mapping, . URL http://www.youtube.com/watch?v=dL4VKuKNgXI. Retrieved on 2010-02-10.

[82] S. H. Strogatz. Nonlinear Dynamics and Chaos: Part 6b—Musical Variations from a Chaotic Mapping, . URL http://www.youtube.com/watch?v=Wz3cmlVwI30. Retrieved on 2010-02-10.

[83] S. Sivaprakasam and K. A. Shore. Signal masking for chaotic optical communication using external-cavity diode lasers. *Opt. Lett.*, 24(17):1200–1202, September 1999.

[84] B. Tromborg, J. Osmundsen, and H. Olesen. Stability analysis for a semiconductor laser in an external cavity. *IEEE J. Quantum Electron.*, 20(9):1023–1032, October 1984.

[85] S. Sivaprakasam and K. A. Shore. Demonstration of optical synchronization of chaotic external-cavity laser diodes. *Opt. Lett.*, 24(7):466–468, April 1999.

[86] I. Fischer, Y. Liu, and P. Davis. Synchronization of chaotic semiconductor laser dynamics on subnanosecond time scales and its potential for chaos communication. *Phys. Rev. A*, 62(1):011801, June 2000.

[87] A. Murakami, K. Kawashima, and K. Atsuki. Cavity resonance shift and bandwidth enhancement in semiconductor lasers with strong light injection. *IEEE J. Quantum Electron.*, 39(10):1196–1204, October 2003.

[88] A. Murakami, K. Kawashima, and K. Atsuki. Corrections to Cavity resonance shift and bandwidth enhancement in semiconductor lasers with strong light injection. *IEEE J. Quantum Electron.*, 39(11):1504, November 2003.

[89] A. Murakami and K. A. Shore. Chaos-pass filtering in injection-locked semiconductor lasers. *Phys. Rev. A*, 72(5):053810, November 2005.

[90] A. Murakami and K. A. Shore. Analogy between optically driven injection-locked laser diodes and driven damped linear oscillators. *Phys. Rev. A*, 73(4):043804, April 2006.

[91] K. A. Shore, M. W. Lee, J. Paul, Yanhua Hong, A. Murakami, I. Pierce, and P. S. Spencer. Chaos synchronisation and message extraction in optical chaos communications. In O. Descalzi, O. A. Rosso, and H. A. Larrondo, editors, *XV Conf. Nonequilibrium Stat. Mech. Nonlin. Phys.*, volume 913 of *AIP Conference Proceedings*, pages 68–72, Mar del Plata, Argentina, May 2007.

[92] S. J. Lea and P. S. Spencer. Frequency domain analysis of the chaotic synchronization of injection-locked semiconductor lasers. *Opt. Quantum Electron.*, 40(2–4):97–108, March 2006.

[93] R. Roy and K. S. Thornburg, Jr. Experimental synchronization of chaotic lasers. *Phys. Rev. Lett.*, 72(13):2009–2012, March 1994.

[94] H. Fujino and J. Ohtsubo. Experimental synchronization of chaotic oscillations in external-cavity semiconductor lasers. *Opt. Lett.*, 25(9):625–627, May 2000.

[95] R. Vicente, T. Pérez, and C. R. Mirasso. Open- versus closed-loop performance of synchronized chaotic external-cavity semiconductor lasers. *IEEE J. Quantum Electron.*, 38(9):1197–1204, September 2002.

[96] M. W. Lee, J. Paul, S. Sivaprakasam, and K. A. Shore. Comparison of closed-loop and open-loop feedback schemes of message decoding using chaotic laser diodes. *Opt. Lett.*, 28(22):2168–2170, November 2003.

[97] A. Argyris and D. Syvridis. Performance of open-loop all-optical chaotic communication systems under strong injection condition. *IEEE J. Lightwave Technol.*, 22(5):1272–1279, May 2004.

[98] A. Bogris, D. Kanakidis, A. Argyris, and D. Syvridis. Performance characterization of a closed-loop chaotic communication system including fiber transmission in dispersion shifted fibers. *IEEE J. Quantum Electron.*, 40(9):1326–1336, September 2004.

[99] A. Argyris, D. Kanakidis, A. Bogris, and D. Syvridis. Experimental evaluation of an open-loop all-optical chaotic communication system. *J. Sel. Top. Quantum Electron.*, 10(5):927–935, September–October 2004.

[100] T. Sugawara, M. Tachikawa, T. Tsakamoto, and T. Shimizu. Observation of synchronization in laser chaos. *Phys. Rev. Lett.*, 72(22):3502–3505, May 1994.

[101] G. D. VanWiggeren and R. Roy. Communication with chaotic lasers. *Science*, 279(5354):1198–1200, February 1998.

[102] J. B. Geddes, K. M. Short, and K. Black. Extraction of signals from chaotic laser data. *Phys. Rev. Lett.*, 83(25):5389–5392, December 1999.

[103] Q. L. Williams and R. Roy. Fast polarization dynamics of an erbium-doped fiber ring laser. *Opt. Lett.*, 21(18):1478–1480, September 1996.

[104] Q. L. Williams, J. García-Ojalvo, and R. Roy. Fast intracavity polarization dynamics of an erbium-doped fiber ring laser: Inclusion of stochastic effects. *Phys. Rev. A*, 55(3):2376–2386, March 1997.

[105] J. García-Ojalvo and R. Roy. Intracavity chaotic dynamics in ring lasers with an injected signal. *Phys. Lett. A*, 229(6):362–366, June 1997.

[106] H. D. I. Abarbanel and M. B. Kennel. Synchronizing high-dimensional chaotic optical ring dynamics. *Phys. Rev. Lett.*, 80(14):3153–3156, April 1998.

[107] E. Ott, C. Grebogi, and J. A. Yorke. Controlling chaos. *Phys. Rev. Lett.*, 64(11):1196–1199, March 1990.

[108] E. Ott, C. Grebogi, and J. A. Yorke. Controlling chaos: Erratum. *Phys. Rev. Lett.*, 64(23):2837, June 1990.

[109] M. J. Ogorzałek. Taming chaos—Part I: Synchronization. *IEEE Trans. Circ. Syst. I*, 40(10):693–699, October 1993.

[110] M. J. Ogorzałek. Taming chaos: Part II—Control. *IEEE Trans. Circ. Syst. I*, 40(10):700–706, October 1993.

[111] A. Sánchez-Díaz, C. R. Mirasso, P. Colet, and P. García-Fernández. Encoded Gbit/s digital communications with synchronized chaotic semiconductor lasers. *IEEE J. Quantum Electron.*, 35(3):292–297, March 1999.

[112] A. Argyris, D. Syvridis, L. Larger, V. Annovazzi-Lodi, P. Colet, I. Fischer, J. García-Ojalvo, C. R. Mirasso, L. Pesquera, and K. A. Shore. Chaos-based communications at high bit rates using commercial fibre-optic links. *Nature*, 438(7066):343–346, November 2005.

[113] C. W. Wu and L. O. Chua. A unified framework for synchronization and control of dynamical systems. *Int. J. Bifurcation Chaos*, 4(4):979–998, August 1994.

[114] G. Kolumbán, M. P. Kennedy, and L. O. Chua. The role of synchronization in digital communications using chaos—Part I: Fundamentals of digital communications. *IEEE Trans. Circ. Syst. I*, 44(10):927–936, October 1997.

[115] G. Kolumbán, M. P. Kennedy, and L. O. Chua. The role of synchronization in digital communications using chaos—Part II: Chaotic modulation and chaotic synchronization. *IEEE Trans. Circ. Syst. I*, 45(11):1129–1140, November 1998.

[116] G. Kolumbán and M. P. Kennedy. The role of synchronization in digital communications using chaos—Part III: Performance bounds for correlation receivers. *IEEE Trans. Circ. Syst. I*, 47(12):1673–1683, December 2000.

[117] G. Kolumbán, M. P. Kennedy, Z. Jákó, and G. Kis. Chaotic communications with correlator receivers: Theory and performance limits. In *IEEE Proc.*, volume 90, pages 711–732, May 2002.

[118] L. Kocarev, K. S. Halle, K. Eckert, L. O. Chua, and U. Parlitz. Experimental demonstration of secure communications via chaotic synchronization. *Int. J. Bifurcation Chaos*, 2(3):709–713, September 1992.

[119] K. M. Cuomo and A. V. Oppenheim. Circuit implementation of synchronized chaos with applications to communications. *Phys. Rev. Lett.*, 71(1):65–68, July 1993.

[120] C. W. Wu and L. O. Chua. A simple way to synchronize chaotic systems with applications to secure communication systems. *Int. J. Bifurcation Chaos*, 3(6):1619–1627, December 1993.

[121] G. Pérez and H. A. Cerdeira. Extracting messages masked by chaos. *Phys. Rev. Lett.*, 74(11):1970–1973, March 1995.

[122] L. Kocarev and U. Parlitz. General approach for chaotic synchronization with applications to communication. *Phys. Rev. Lett.*, 74(25):5028–5031, June 1995.

[123] K. M. Short. Steps toward unmasking secure communications. *Int. J. Bifurcation Chaos*, 4(4):959–977, August 1994.

[124] K. M. Short and A. T. Parker. Unmasking a hyperchaotic communication scheme. *Phys. Rev. E*, 58(1):1159–1162, July 1998.

[125] X. Huang, J. Xu, W. Huang, and Z. Lu. Unmasking chaotic mask by a wavelet multiscale decomposition algorithm. *Int. J. Bifurcation Chaos*, 11(2):561–569, February 2001.

[126] B. P. Bezruchko, A. S. Karavaev, V. I. Ponomarenko, and M. D. Prokhorov. Reconstruction of time-delay systems from chaotic time series. *Phys. Rev. E*, 64(5):056216, October 2001.

[127] V. I. Ponomarenko and M. D. Prokhorov. Extracting information masked by the chaotic signal of a time-delay system. *Phys. Rev. E*, 66(2):026215, August 2002.

[128] G. Álvarez, F. Montoya, M. Romera, and G. Pastor. Breaking two secure communication systems based on Chaotic Masking. *IEEE Trans. Circ. Syst. II*, 51(10):505–506, October 2004.

[129] A. V. Oppenheim, G. W. Wornell, S. H. Isabelle, and K. M. Cuomo. Signal processing in the context of chaotic signals. In *IEEE Int. Conf. Acoustics Speech Signal Process.*, volume 4, pages 117–120, San Francisco, CA, USA, March 1992.

[130] K. M. Cuomo and A. V. Oppenheim. Chaotic signals and systems for communications. In *IEEE Int. Conf. Acoustics Speech Signal Process.*, volume 3, pages 137–140, Minneapolis, MN, USA, April 1993.

[131] K. M. Cuomo, A. V. Oppenheim, and S. H. Strogatz. Synchronization of Lorenz-based chaotic circuits with applications to communications. *IEEE Trans. Circ. Syst. II*, 40(10):626–633, October 1993.

[132] U. Parlitz, L. Kocarev, T. Stojanovski, and H. Preckel. Encoding messages using chaotic synchronization. *Phys. Rev. E*, 53(5):4351–4361, May 1996.

[133] T. Yang, L.-B. Yang, and C.-M. Yang. Cryptanalyzing chaotic secure communications using return maps. *Phys. Lett. A*, 245(6):495–510, August 1998.

[134] S. Bu and B.-H. Wang. Improving the security of chaotic encryption by using a simple modulating method. *Chaos Solitons Fractals*, 19(4):919–924, March 2004.

[135] C. Y. Chee, D. Xu, and S. R. Bishop. A zero-crossing approach to uncover the mask by chaotic encryption with periodic modulation. *Chaos Solitons Fractals*, 21(5):1129–1134, September 2004.

[136] X. Wu, H. Hu, and B. Zhang. Analyzing and improving a chaotic encryption method. *Chaos Solitons Fractals*, 22(2):367–373, October 2004.

[137] G. Álvarez, F. Montoya, M. Romera, and G. Pastor. Cryptanalyzing an improved security modulated chaotic encryption scheme using ciphertext absolute value. *Chaos Solitons Fractals*, 23(5):1749–1756, March 2005.

[138] K. M. Short. Unmasking a modulated chaotic communications scheme. *Int. J. Bifurcation Chaos*, 6(2):367–375, February 1996.

171

[139] K. M. Short. Signal extraction from chaotic communications. *Int. J. Bifurcation Chaos*, 7(7):1579–1597, July 1997.

[140] S. Li, G. Álvarez, and G. Chen. Breaking a chaos-based secure communication scheme designed by an improved modulation method. *Chaos Solitons Fractals*, 25(1):109–120, July 2005.

[141] R. J. Jones, S. Sivaprakasam, and K. A. Shore. Integrity of semiconductor laser chaotic communications to naïve eavesdroppers. *Opt. Lett.*, 25(22):1663–1665, November 2000.

[142] U. Parlitz, L. O. Chua, L. Kocarev, K. S. Halle, and A. Shang. Transmission of digital signals by chaotic synchronization. *Int. J. Bifurcation Chaos*, 2(4):973–977, December 1992.

[143] H. Dedieu, M. P. Kennedy, and M. Hasler. Chaos Shift Keying: Modulation and demodulation of a chaotic carrier using self-synchronizing Chua's circuits. *IEEE Trans. Circ. Syst. II*, 40(10):634–642, October 1993.

[144] T. Yang. Recovery of digital signals from Chaotic Switching. *Int. J. Circ. Theory Appl.*, 23(6):611–615, November–December 1995.

[145] T. Yang, L.-B. Yang, and C.-M. Yang. Breaking Chaotic Switching using generalized synchronization: Examples. *IEEE Trans. Circ. Syst. I*, 45(10):1062–1067, October 1998.

[146] T. Yang, L.-B. Yang, and C.-M. Yang. Breaking chaotic secure communication using a spectrogram. *Phys. Lett. A*, 247(1-2):105–111, October 1998.

[147] T. Yang, L.-B. Yang, and C.-M. Yang. Application of neural networks to unmasking chaotic secure communication. *Physica D*, 124(1–3):248–257, 1998.

[148] H.-P. Ren, C.-Z. Han, and D. Liu. Breaking Chaotic Shift Key communication via adaptive key identification. *Chinese Phys. B*, 17(4):1202–1208, April 2008.

[149] M. Long and S.-S. Qiu. Application of periodic orbit theory in chaos-based security analysis. *Chinese Phys.*, 16(8):2254–2258, August 2007.

[150] T. L. Carroll and L. M. Pecora. Using multiple attractor chaotic systems for communication. In *IEEE Conf. Electron. Circ. Syst.*, volume 1, pages 103–106, Lisboa, Portugal, July–October 1998.

[151] L. S. Tsimring and M. M. Sushchik. Multiplexing chaotic signals using synchronization. *Phys. Lett. A*, 213(3–4):155–166, April 1996.

[152] J. H. Peng, E. J. Ding, M. Ding, and W. Yang. Synchronizing hyperchaos with a scalar transmitted signal. *Phys. Rev. Lett.*, 76(6):904–907, February 1996.

[153] G. A. Johnson, D. J. Mar, T. L. Carroll, and L. M. Pecora. Synchronization and imposed bifurcations in the presence of large parameter mismatch. *Phys. Rev. Lett.*, 80(18):3956–3959, May 1998.

[154] C. R. Mirasso, J. Mulet, and C. Masoller. Chaos Shift-Keying encryption in chaotic external-cavity semiconductor lasers using a single-receiver scheme. *IEEE Photon. Technol. Lett.*, 14(4):456–458, April 2002.

[155] T. Schimming and M. Hasler. Comparison of different Chaos Shift Keying methods. In *European Conf. on Circ. Theory and Design*, volume 2, pages 185–188, Espoo, Finland, August 2001. URL http://lib.tkk.fi/ Books/2001/isbn9512263378/papers/1348.pdf.

[156] T. Stojanovski, L. Kocarev, and U. Parlitz. A simple method to reveal the parameters of the Lorenz system. *Int. J. Bifurcation Chaos*, 6(12b):2645–2652, December 1996.

[157] K. S. Halle, C. W. Wu, M. Itoh, and L. O. Chua. Spread spectrum communication through modulation of chaos. *Int. J. Bifurcation Chaos*, 3(2):469–477, April 1993.

[158] V. Ahlers, U. Parlitz, and W. Lauterborn. Hyperchaotic dynamics and synchronization of external-cavity semiconductor lasers. *Phys. Rev. E*, 58(6):7208–7213, December 1998.

[159] L. Kocarev, U. Parlitz, and T. Stojanovski. An application of synchronized chaotic dynamic arrays. *Phys. Lett. A*, 217(4–5):280–284, July 1996.

[160] C.-S. Zhou and C.-H. Lai. Extracting messages masked by chaotic signals of time-delay systems. *Phys. Rev. E*, 60(1):320–323, July 1999.

[161] V. S. Udaltsov, J.-P. Goedgebuer, L. Larger, J.-B. Cuenot, P. Levy, and W. T. Rhodes. Cracking chaos-based encryption systems ruled by nonlinear time delay differential equations. *Phys. Lett. A*, 308(1):54–60, February 2003.

[162] M. D. Prokhorov, V. I. Ponomarenko, A. S. Karavaev, and B. P. Bezruchko. Reconstruction of time-delayed feedback systems from time series. *Physica D*, 203(3–4):209–223, April 2005.

[163] U. Parlitz and L. Kocarev. Multichannel communication using autosynchronization. *Int. J. Bifurcation Chaos*, 6(3):581–588, March 1996.

[164] U. Parlitz. Estimating model parameters from time series by autosynchronization. *Phys. Rev. Lett.*, 76(8):1232–1235, February 1996.

[165] J. L. Breeden and A. Hübler. Reconstructing equations of motion from experimental data with unobserved variables. *Phys. Rev. A*, 42(10):5817–5826, November 1990.

[166] E. Baake, M. Baake, H. G. Bock, and K. M. Briggs. Fitting ordinary differential equations to chaotic data. *Phys. Rev. A*, 45(8):5524–5529, April 1992.

[167] T. Yang, C. W. Wu, and L. O. Chua. Cryptography based on chaotic systems. *IEEE Trans. Circ. Syst. I*, 44(5):469–472, May 1997.

[168] A. T. Parker and K. M. Short. Reconstructing the key-stream from a chaotic encryption scheme. *IEEE Trans. Circ. Syst. I*, 48(5):624–630, May 2001.

[169] F. Anstett, G. Millerioux, and G. Bloch. Message-embedded cryptosystems: cryptanalysis and identifiability. In *44th IEEE Conference on Decision and Control*, pages 2548–2553, December 2005.

[170] J. Y. Chen, K. W. Wong, L. M. Cheng, and J.-W. Shuai. A secure communication scheme based on the phase synchronization of chaotic systems. *Chaos*, 13(2):508–514, June 2003.

[171] G. Álvarez, F. Montoya, G. Pastor, and M. Romera. Breaking a secure communication scheme based on the phase synchronization of chaotic systems. *Chaos*, 14(2):274–278, June 2004.

[172] A. A. Minai and T. D. Pandian. Communicating with noise: How chaos and noise combine to generate secure encryption keys. *Chaos*, 8(3):621–628, September 1998.

[173] S. Li, G. Álvarez, G. Chen, and Xuanqin Mou. Breaking a chaos-noise-based secure communication scheme. *Chaos*, 15(1):013703, February 2005.

[174] U. Parlitz and S. Ergezinger. Robust communication based on chaotic spreading sequences. *Phys. Lett. A*, 188(2):146–150, May 1994.

[175] C.-S. Zhou and Tian-lun Chen. Extracting information masked by chaos and contaminated with noise: Some considerations on the security of communication approaches using chaos. *Phys. Lett. A*, 234(6):429–435, October 1997.

[176] J.-F. Hu and J.-B. Guo. Breaking a chaotic secure communication scheme. *Chaos*, 18(1):013121, March 2008.

[177] J.-F. Hu and J.-B. Guo. Publisher's Note: "Breaking a chaotic secure communication scheme". *Chaos*, 18(2): 029901, June 2008.

[178] B. C. Lam, A. L. Kellner, M. M. Sushchik, H. D. I. Abarbanel, and P. K. L. Yu. Observation of chaotic instability in the active mode locking of a semiconductor laser. *J. Opt. Soc. Am. B*, 10(11):2065–2070, November 1993.

[179] H. G. Winful, Y. C. Chen, and J. M. Liu. Frequency locking, quasiperiodicity, and chaos in modulated self-pulsing semiconductor lasers. *Appl. Phys. Lett.*, 48(10): 616–618, March 1986.

[180] R. J. Jones, P. Rees, P. S. Spencer, and K. A. Shore. Chaos and synchronization of self-pulsating laser diodes. *J. Opt. Soc. Am. B*, 18(2):166–172, February 2001.

[181] R. P. Walker, P. Rees, I. Pierce, P. S. Spencer, and G. W. Roberts. Analysis of chaos generated by a modulated self-pulsating laser diode. In *IEE Proc. Opto-Electron.*, volume 152, pages 90–96, April 2005.

[182] J. Mørk, J. Mark, and B. Tromborg. Route to chaos and competition between relaxation oscillations for a semiconductor laser with optical feedback. *Phys. Rev. Lett.*, 65(16):1999–2002, October 1990.

[183] L. N. Langley, K. A. Shore, and J. Mørk. Dynamical and noise properties of laser diodes subject to strong optical feedback. *Opt. Lett.*, 19(24):2137–2139, December 1994.

[184] L. A. Melnikov, E. M. Rabinovich, and V. V. Tuchin. Quasi-periodic oscillations and chaos in a gas-discharge active mode-locked laser. *J. Opt. Soc. Am. B*, 5(5):1134–1138, May 1988.

[185] D. L. MacFarlane and L. W. Casperson. Pulse-train instabilities of a synchronously pumped mode-locked dye laser: Experimental phase plots. *J. Opt. Soc. Am. B*, 7 (3):285–287, March 1990.

[186] D. L. MacFarlane and L. W. Casperson. Pulse-train instabilities in a mode-locked Argon laser: Experimental studies. *J. Opt. Soc. Am. B*, 4(11):1777–1780, November 1987.

[187] S. Craver, J.-L. Dugelay, F. Hartung, N. F. Johnson, M. Kutter, J.-H. Lee, S. Lai, F. Marongiu-Buonaiuti, A. Perrig, and S. Roche. *Information Hiding Techniques for Steganography and Digital Watermarking*. Computer Security series. Artech House, Norwood, MA, USA, 2000. ISBN 1-58053-035-4.

[188] A. B. Orúe, V. Fernández, G. Álvarez, G. Pastor, M. Romera, F. Montoya, C. Sanchez-Avila, and S. Li. Breaking a SC-CNN-based Chaotic Masking secure communication system. *Int. J. Bifurcation Chaos*, 19 (4):1329–1338, April 2009.

[189] C. Tresser and P. Worfolk. Chaotic signal masking with arbitrarily fine recovery. *Appl. Math. Lett.*, 10(5):103–106, September 1997.

[190] G. Álvarez, S. Li, F. Montoya, G. Pastor, and M. Romera. Breaking projective chaos synchronization secure communication using filtering and generalized synchronization. *Chaos Solitons Fractals*, 24(3):775–783, May 2004.

[191] A. Einstein. Zur Quantentheorie der Strahlung. *Phys. Z.*, 18:121–128, 1917.

[192] R. W. Landenburg. Experimental proof of 'negative dispersion'. *Nature*, 122(3073):438–439, September 1928.

[193] S. G. Lukishova. Valentin A. Fabrikant: negative absorption, his 1951 patent application for amplification of electromagnetic radiation (ultraviolet, visible, infrared and radio spectral regions) and his experiments. *J. Europ. Opt. Soc. Rap. Public.*, 5, September 2010.

[194] W. E. Lamb, Jr. and R. C. Retherford. Fine structure of the hydrogen atom by a microwave method. *Phys. Rev.*, 72(3):241–243, August 1947.

[195] W. E. Lamb, Jr. and R. C. Retherford. Fine structure of the hydrogen atom. Part I. *Phys. Rev.*, 79(4):549–572, August 1950.

[196] W. E. Lamb, Jr. and R. C. Retherford. Fine structure of the hydrogen atom. Part II. *Phys. Rev.*, 81(2):222–232, January 1951.

[197] W. E. Lamb, Jr. Fine structure of the hydrogen atom. Part III. *Phys. Rev.*, 85(2):259–276, January 1952.

[198] W. E. Lamb, Jr. and R. C. Retherford. Fine structure of the hydrogen atom. Part IV. *Phys. Rev.*, 86(6):1014–1022, June 1952.

[199] A. Kastler. Applications of polarimetry to infra-red and micro-wave spectroscopy. *Nature*, 166(4211):113, July 1950.

[200] J. P. Gordon, H. J. Zeiger, and C. H. Townes. Molecular microwave oscillator and new hyperfine structure in the microwave spectrum of NH_3. *Phys. Rev.*, 95(1): 282–284, July 1954.

[201] J. P. Gordon, H. J. Zeiger, and C. H. Townes. The maser—New type of microwave amplifier, frequency standard, and spectrometer. *Phys. Rev.*, 99(4):1264–1274, August 1955.

[202] N. G. Basov and A. M. Prokhorov. Possible methods for obtaining active molecules for a maser. *Zh. Eksp. Teor. Fiz.*, 28:249, 1955.

[203] N. G. Basov and A. M. Prokhorov. Possible methods for obtaining active molecules for a maser. *J. Exp. Theor. Phys.*, 1:184, 1955.

[204] A. L. Schawlow and C. H. Townes. Infrared and optical masers. *Phys. Rev.*, 112(6):1940–1949, December 1958.

[205] J. Hecht. *Beam: The Race to Make the Laser*. Oxford University Press, 2005. ISBN 0-195-14210-1.

[206] A. M. Prokhorov. Molecular amplifier and generator for submillimeter waves. *Zh. Eksp. Teor. Fiz.*, 34:1658–1659, June 1958.

[207] A. M. Prokhorov. Molecular amplifier and generator for submillimeter waves. *J. Exp. Theor. Phys.*, 7:1140–1141, December 1958.

[208] G. R. Gould. The LASER, Light Amplification by Stimulated Emission of Radiation. In P. A. Franken and R. H. Sands, editors, *The Ann Arbor Conference on Optical Pumping*, page 128, University of Michigan, MI, USA, June 1959.

[209] T. H. Maiman. Stimulated optical radiation in ruby. *Nature*, 187(4736):493–494, August 1960.

[210] A. Javan, W. R. Bennett, Jr., and D. R. Herriot. Population inversion and continuous optical maser oscillation in a gas discharge containing a He–Ne mixture. *Phys. Rev. Lett.*, 6(3):106–110, February 1961.

[211] R. N. Hall, G. E. Fenner, J. D. Kingsley, T. J. Soltys, and R. O. Carlson. Coherent light emission from GaAs junctions. *Phys. Rev. Lett.*, 9(9):366–368, November 1962.

[212] N. Holonyak, Jr., S. W. Ing, Jr., R. C. Thomas, and S. F. Bevacqua. Double injection with negative resistance in semi-insulators. *Phys. Rev. Lett.*, 8(11):426–428, June 1962.

[213] M. I. Nathan, W. P. Dumke, G. Burns, F. H. Dill, Jr., and G. Lasher. Stimulated emission of radiation from GaAs p-n junctions. *Appl. Phys. Lett.*, 1(3):62–64, November 1962.

[214] T. M. Quist, R. H. Rediker, R. J. Keyes, W. E. Krag, B. Lax, A. L. McWhorter, and H. J. Zeiger. Semiconductor maser of GaAs. *Appl. Phys. Lett.*, 1(4):91–92, December 1962.

[215] Z. H. I. Alferov, V. M. Andreev, V. Korolkov, E. L. Portnoi, and D. N. Tretiakov. Coherent radiation of epitaxial heterojunction structures in the AlAs–GaAs system (Coherent emission in epitaxial structures with heterojunctions in AlAs–GaAs system). *Sov. Phys. Semicond.*, 2:1289–1291, 1969.

[216] Z. H. I. Alferov, V. M. Andreev, E. L. Portnoi, and M. K. Trukan. AlAs–GaAs heterojunction injection lasers with a low room-temperature threshold. *Sov. Phys. Semicond.*, 3(9):1107–1110, March 1970.

[217] I. Hayashi, M. B. Panish, P. W. Foy, and S. Sumski. Junction lasers which operate continuously at room temperature. *Appl. Phys. Lett.*, 17(3):109–111, August 1970.

[218] M. B. Panish. Heterostructure injection lasers. *IEEE Trans. Microwave Theory Tech.*, 23(1):20–30, January 1975.

[219] J. P. van der Ziel, R. Dingle, R. C. Miller, W. Wiegmann, and W. A. Nordland, Jr. Laser oscillation from quantum states in very thin GaAs–$Al_{0.2}Ga_{0.8}As$ multilayer structures. *Appl. Phys. Lett.*, 26(8):463–465, April 1975.

[220] R. Lang and K. Kobayashi. External optical feedback effects on semiconductor injection laser properties. *IEEE J. Quantum Electron.*, 16(3):347–355, March 1980.

[221] R. W. Tkach and A. R. Chraplyvy. Regimes of feedback effects in 1.5-μm Distributed Feedback Lasers. *IEEE J. Lightwave Technol.*, 4(11):1655–1661, November 1986.

[222] T. L. Carroll and L. M. Pecora. Synchronizing chaotic circuits. *IEEE Trans. Circ. Syst.*, 38(4):453–456, April 1991.

[223] L. M. Pecora and T. L. Carroll. Synchronized chaotic signals and systems. In *IEEE Int. Conf. Acoustics Speech Signal Process.*, volume 4, pages 137–140, San Francisco, CA, USA, March 1992.

[224] T. L. Carroll and L. M. Pecora. Synchronizing nonautonomous chaotic circuits. *IEEE Trans. Circ. Syst. II*, 40(10):646–650, October 1993.

[225] T. L. Carroll and L. M. Pecora. The effect of filtering on communication using synchronized chaotic circuits. In *IEEE Int. Symp. Circ. Syst.*, volume 3, pages 174–177, Atlanta, GA, USA, May 1996.

[226] J. L. Bromberg. The birth of laser. *Physics Today*, 41 (10):26–33, October 1988.

[227] N. Taylor. *LASER: The inventor, the Nobel laureate, and the thirty-year patent war.* Simon & Schuster, New York, 2000. ISBN 0-684-83515-0.

[228] S. K. Hwang, J. M. Liu, and J. K. White. 35-GHz intrinsic bandwidth for direct modulation in 1.3-μm semiconductor lasers subject to strong injection locking. *IEEE Photon. Technol. Lett.*, 16(4):972–974, April 2004.

[229] M. C. Wu, C. Chang-Hasnain, E. K. Lau, and X. Zhao. High-speed modulation of optical injection-locked semiconductor lasers. In *Conference on Optical Fiber communication/National Fiber Optic Engineers Conference*, pages 1–3, February 2008.

[230] I. D. Henning and J. V. Collins. Measurements of the semiconductor laser linewidth broadening factor. *Electron. Lett.*, 19(22):927–929, October 1983.

[231] A. Yariv, Rashit Nabiev, and Kerry Vahala. Self-quenching of fundamental phase and amplitude noise in semiconductor lasers with dispersive loss. *Opt. Lett.*, 15(23):1359–1361, December 1990.

[232] Y. Shevy and H. Deng. Frequency-stable and ultranarrow-linewidth semiconductor laser locked directly to an atom-cesium transition. *Opt. Lett.*, 23(6): 472–474, March 1998.

[233] C. H. Henry. Theory of the linewidth of semiconductor lasers. *IEEE J. Quantum Electron.*, 18(2):259–264, February 1982.

[234] J. C. Maxwell. On physical lines of force. Part 1. *Phil. Mag. (Series 4)*, 21(139):161–175, March 1861.

[235] J. C. Maxwell. On physical lines of force. Part 2. *Phil. Mag. (Series 4)*, 21(140):281–291, April 1861.

[236] J. C. Maxwell. On physical lines of force. Part 3. *Phil. Mag. (Series 4)*, 21(141):338–348, May 1861.

[237] J. C. Maxwell. On physical lines of force. Part 4. *Phil. Mag. (Series 4)*, 23(151):12–24, January 1862.

[238] J. C. Maxwell. On physical lines of force. Part 5. *Phil. Mag. (Series 4)*, 23(152):85–95, February 1862.

[239] J. C. Maxwell. A dynamical theory of the electromagnetic field. *Phil. Trans. R. Soc. Lond.*, 155:459–512, January 1865.

[240] J. C. Maxwell. *A Treatise on Electricity and Magnetism*, volume 1. Clarendon Press, Oxford, UK, 1873.

[241] J. C. Maxwell. *A Treatise on Electricity and Magnetism*, volume 2. Clarendon Press, Oxford, UK, 1873.

[242] Charles M. Bowden and G. P. Agrawal. Maxwell-Bloch formulation for semiconductors: Effects of coherent Coulomb exchange. *Phys. Rev. A*, 51(5):4132–4139, May 1995.

[243] J. Ohtsubo. Chaotic dynamics in semiconductor lasers with optical feedback. In E. Wolf, editor, *Prog. Optics*, volume 44, chapter 1, pages 1–84. Elsevier Science B. V., 2002.

[244] J. Ohtsubo. ERRATA "Chaotic dynamics in semiconductor lasers with optical feedback", 2002. URL http://www.sys.eng.shizuoka.ac.jp/~ohtsubo1/files/publication/2002/pdf02-9.pdf.

[245] G. P. Agrawal and N. K. Dutta. *Long-wavelength semiconductor lasers.* Van Nostrand Reinhold electrical/computer science and engineering series. Van Nostrand Reinhold, New York, NY, USA, 1986. ISBN 0-442-20995-9.

[246] R.-D. Li and P. Mandel. Laser dynamics beyond the Slowly Varying Envelope Approximation. *Opt. Commun.*, 75(1):72–83, February 1990.

[247] R. Bonifacio, R. M. Caloi, and C. Maroli. The slowly varying envelope approximation revisited. *Opt. Commun.*, 101(3–4):185–187, August 1993.

[248] A. A. Duarte and H. G. Solari. Slowly varying envelope approximation in a laser with optical feedback. *Phys. Rev. A*, 64(3):033803, August 2001.

[249] J. Ohtsubo. *Semiconductor lasers.* Springer Series in Optical Sciences. Springer, 2nd edition, 2008. ISBN 978-3-540-72647-0.

[250] G. H. M. van Tartwijk and G. P. Agrawal. Laser instability: A modern perspective. *Prog. Quantum Electron.*, 22(2):43–122, March 1998. Review Article.

[251] P. W. Milonni and J. H. Eberly. *Laser Physics.* John Wiley & Sons, 2nd edition, 2010. ISBN 0-470-38771-8.

[252] B. J. West and K. Lindenberg. On the rotating wave approximation. *Phys. Lett. A*, 102(4):189–193, May 1984.

[253] G. W. Ford and R. F. O'Connell. The rotating wave approximation (RWA) of quantum optics: serious defect. *Physica A*, 243(3–4):377–381, September 1997.

[254] I. Dolce, R. Passante, and F. Persico. The limits of the rotating wave approximation in electromagnetic field propagation in a cavity. *Phys. Lett. A*, 355(2):152–155, June 2006.

[255] F. T. Arecchi, G. L. Lippi, G. P. Puccioni, and J. R. Tredicce. Deterministic chaos in laser with injected signal. *Opt. Commun.*, 51(5):308–314, October 1984.

[256] T. W. Hänsch, M. Pernier, and A. L. Schawlow. Laser action of dyes in gelatin. *IEEE J. Quantum Electron.*, 7(1):45–46, January 1971.

[257] A. L. Schawlow. Lasers: The practical and the possible. *The Stanford Magazine*, pages 24–29, Spring/Summer 1979.

[258] T. W. Hänsch. Edible lasers and other delights of the 1970s. *Opt. Photon. News*, 16(2):14–16, February 2005.

[259] A. E. Siegman. *Lasers.* University Science Books, 1986. ISBN 0-935-70211-3.

[260] J. R. Tredicce, F. T. Arecchi, G. L. Lippi, and G. P. Puccioni. Instabilities in lasers with an injected signal. *J. Opt. Soc. Am. B*, 2(1):173–183, January 1985.

[261] M. C. Torrent, S. Balle, M. San Miguel, and J. M. Sancho. Detection of a weak external signal via the switch-on-time statistics of a semiconductor laser. *Phys. Rev. A*, 47(4):3390–3395, April 1993.

[262] R. Hui, A. Mecozzi, A. D'Ottavi, and P. Spano. Novel measurement technique of alpha factor in DFB semiconductor lasers by injection locking. *Electron. Lett.*, 26(14):997–998, July 1990.

[263] R. Hui, A. D'Ottavi, A. Mecozzi, and P. Spano. Injection locking in Distributed Feedback semiconductor lasers. *IEEE J. Quantum Electron.*, 27(6):1688–1695, June 1991.

[264] C. Lin, J. K. Andersen, and F. Mengel. Frequency chirp reduction in a 2.2 Gbit/s directly modulated InGaAsP semiconductor laser by cw injection. *Electron. Lett.*, 21(2):80–81, January 1985.

[265] N. A. Olsson, H. Temkin, R. A. Logan, L. F. Johnson, G. J. Dolan, J. P. van der Ziel, and J. C. Campbell. Chirp-free transmission over 82.5 km of single mode fiber at 2 Gbit/s with injection locked DFB semiconductor laser. *IEEE J. Lightwave Technol.*, 3(1):63–67, February 1985.

[266] P. A. Andrekson, N. A. Olsson, T. Tanbun-Ek, and M. A. Washington. High power semiconductor laser injection-locking at 1.3 μm. *IEEE J. Lightwave Technol.*, 10(7):903–907, July 1992.

[267] S. Mohrdiek, H. Burkhard, and H. Walter. Chirp reduction of directly modulated semiconductor lasers at 10 Gb/s by strong cw light injection. *IEEE J. Lightwave Technol.*, 12(3):418–424, March 1994.

[268] J. Wang, M. K. Haldar, L. Li, and F. V. C. Mendis. Enhancement of modulation bandwidth of laser diodes by injection locking. *IEEE Photon. Technol. Lett.*, 8(1):34–36, January 1996.

[269] J. Dellunde and M. C. Torrent. Optoelectronic feedback stabilization of current modulated laser diodes. *Appl. Phys. Lett.*, 68(12):1601–1603, March 1996.

[270] H. Haken. Analogy between higher instabilities in fluids and lasers. *Phys. Lett. A*, 53(1):77–78, May 1975.

[271] E. N. Lorenz. Deterministic nonperiodic flow. *J. Atmos. Sci.*, 20:130–141, March 1963.

[272] R. C. Hilborn. *Chaos and Nonlinear Dynamics: An Introduction for Scientists and Engineers.* Oxford University Press, 2nd edition, 2000. ISBN 0-198-50723-2.

[273] G. H. M. van Tartwijk and G. P. Agrawal. Nonlinear dynamics in the generalized Lorenz–Haken model. *Opt. Commun.*, 133(1–6):565–577, January 1997.

[274] M. J. Tomás, E. Roldán, G. J. de Valcárcel, and R. Vilaseca. Generalization of the Lorenz–Haken model to atomic systems with different relaxation rates for the two laser levels. *Opt. Commun.*, 114(1–2):111–118, January 1995.

[275] K. Petermann. *Laser diode modulation and noise.* Advances in Optoelectronics. Kluwer Academic Publishers, 1991. ISBN 0-792-31204-X.

[276] G. H. M. van Tartwijk and D. Lenstra. Semiconductor lasers with optical injection and feedback. *Quantum Semiclass. Opt.*, 7(2):87–143, April 1995. Review Article.

[277] C. B. Su, V. Lanzisera, R. Olshansky, W. Powazinik, E. Meland, J. Schlafer, and R. B. Lauer. 15 GHz direct modulation bandwidth of vapour-phase regrown 1.3 μm InGaAsP buried-heterostructure lasers under cw operation at room temperature. *Electron. Lett.*, 21(13):577–579, June 1985.

[278] A. Bogris, P. G. Eliseev, and B. N. Sverdlov. Anomalous interaction of spectral modes in a semiconductor laser. *IEEE J. Quantum Electron.*, 11(7):510–515, July 1975.

[279] M. Asada and Y. Suematsu. Density-matrix theory of semiconductor lasers with relaxation broadening model—gain and gain-suppression in semiconductor lasers. *IEEE J. Quantum Electron.*, 21(5):434–442, May 1985.

[280] M. Yamada and Y. Suematsu. A condition of single longitudinal mode operation in injection lasers with index-guiding structure. *IEEE J. Quantum Electron.*, 15(8):743–749, August 1979.

[281] R. S. Tucker and D. J. Pope. Circuit modeling of the effect of diffusion on damping in a narrow-stripe semiconductor laser. *IEEE J. Quantum Electron.*, 19(7):1179–1183, July 1983.

[282] Ch. Risch and C. Voumard. Self-pulsation in the output intensity and spectrum of GaAs-AlGaAs cw diode lasers coupled to a frequency-selective external optical cavity. *J. Appl. Phys.*, 48(5):2083–2085, May 1977.

175

[283] C. Voumard. External-cavity-controlled 32-MHz narrow-band cw GaAlAs-diode lasers. *Opt. Lett.*, 1(2): 61–63, August 1977.

[284] R. O. Miles, A. Dandridge, A. B. Tveten, H. F. Taylor, and T. G. Giallorenzi. Feedback-induced line broadening in cw channel-substrate planar laser diodes. *Appl. Phys. Lett.*, 37(11):990–992, December 1980.

[285] P. Glas, R. Müller, and A. Klehr. Bistability, self-sustained oscillations, and irregular operation of a GaAs laser coupled to an external resonator. *Opt. Commun.*, 47(4):297–301, September 1983.

[286] D. Lenstra, B. H. Verbeek, and A. J. den Boef. Coherence collapse in single-mode semiconductor lasers due to optical feedback. *IEEE J. Quantum Electron.*, 21(6): 674–679, June 1985.

[287] Y. Cho and T. Umeda. Observation of chaos in a semiconductor laser with delayed feedback. *Opt. Commun.*, 59(2):131–136, August 1986.

[288] H. Yasaka and H. Kawaguchi. Linewidth reduction and optical frequency stabilization of a distributed feedback laser by incoherent optical negative feedback. *Appl. Phys. Lett.*, 53(15):1360–1362, October 1988.

[289] F. Favre, D. le Guen, J. C. Simon, and B. Landousies. External-cavity semiconductor laser with 15 nm continuous tuning range. *Electron. Lett.*, 22(15):795–796, July 1986.

[290] N. Schunk and K. Petermann. Numerical analysis of the feedback regimes for a single-mode semiconductor laser with external feedback. *IEEE J. Quantum Electron.*, 24 (7):1242–1247, July 1988.

[291] M. W. Fleming and A. Mooradian. Spectral characteristics of external-cavity controlled semiconductor lasers. *IEEE J. Quantum Electron.*, 17(1):44–59, January 1981.

[292] M. W. Fleming and A. Mooradian. Correction to "Spectral characteristics of external-cavity-controlled semiconductor lasers". *IEEE J. Quantum Electron.*, 17(8): 1586, August 1981.

[293] R. Wyatt and W. J. Devlin. 10 kHz linewidth 1.5 μm InGaAsP external cavity laser with 55 nm tuning range. *Electron. Lett.*, 19(3):110–112, February 1983.

[294] H. Temkin, N. A. Olsson, J. H. Abeles, R. A. Logan, and M. B. Panish. Reflection noise in index-guided InGaAsP lasers. *IEEE J. Quantum Electron.*, 22(2):286–293, February 1986.

[295] A. R. Chraplyvy, K. Y. Liou, R. W. Tkach, G. Eisenstein, Y. K. Jhee, T. L. Koch, P. J. Anthony, and U. K. Chakrabarti. Simple narrow-linewidth 1.5 μm InGaAsP DFB external-cavity laser. *Electron. Lett.*, 22(2):88–90, January 1986.

[296] R. F. Broom, E. Mohn, C. Risch, and R. Salathé. Microwave self-modulation of a diode laser coupled to an external cavity. *IEEE J. Quantum Electron.*, 6(6):328–334, June 1970.

[297] T. Morikawa, Y. Mitsuhashi, J. Shimada, and Y. Kojima. Return-beam-induced oscillations in self-coupled semiconductor lasers. *Electron. Lett.*, 12(17): 435–436, August 1976.

[298] O. Hirota and Y. Suematsu. Noise properties of injection lasers due to reflected waves. *IEEE J. Quantum Electron.*, 15(3):142–149, March 1979.

[299] C. H. Henry and R. F. Kazarinov. Instability of semiconductor lasers due to optical feedback from distant reflectors. *IEEE J. Quantum Electron.*, 22(2):294–301, February 1986.

[300] R. W. Tkach and A. R. Chraplyvy. Linewidth broadening and mode splitting due to weak feedback in single-frequency 1.5 μm lasers. *Electron. Lett.*, 21(23):1081–1083, November 1985.

[301] K. Kikuchi and T. Okoshi. Simple formula giving spectrum-narrowing ratio of semiconductor-laser output obtained by optical feedback. *Electron. Lett.*, 18 (1):10–12, January 1982.

[302] L. Goldberg, H. F. Taylor, A. Dandridge, J. F. Weller, and R. O. Miles. Spectral characteristics of semiconductor lasers with optical feedback. *IEEE J. Quantum Electron.*, 18(4):555–564, April 1982.

[303] F. Favre, D. le Guen, and J. C. Simon. Optical feedback effects upon laser diode oscillation field spectrum. *IEEE Trans. Microwave Theory Tech.*, 30(10): 1700–1705, October 1982.

[304] F. Kéfélian and P. Gallion. Theoretical analysis of optical injection locking of semiconductor DFB lasers, influence of the injection direction. In D. Lenstra, M. Pessa, and I. H. White, editors, *SPIE Proc.*, volume 6184 of *Semiconductor Lasers and Laser Dynamics II*, page 61840I, Strasbourg, France, April 2006.

[305] G. P. Agrawal and C. M. Bowden. Concept of Linewidth Enhancement Factor in semiconductor lasers: Its usefulness and limitations. *IEEE Photon. Technol. Lett.*, 5(6):640–642, June 1993.

[306] J. Buus. Dynamic line broadening of semiconductor lasers modulated at high frequencies. *Electron. Lett.*, 21(4):129–131, February 1985.

[307] K. E. Chlouverakis, K. M. Al-Aswad, I. D. Henning, and M. J. Adams. Determining laser linewidth parameter from Hopf bifurcation minimum in lasers subject to optical injection. *Electron. Lett.*, 39(16):1185–1187, August 2003.

[308] N. Schunk and K. Petermann. Stability analysis for laser diodes with short external cavities. *IEEE Photon. Technol. Lett.*, 1(3):49–51, March 1989.

[309] M. Peil, T. Heil, I. Fischer, W. Elsäßer, and J. M. Buldú. Chaos-synchronization of semiconductor laser systems in an open-loop configuration: The short cavity regime and its potential for secure communication systems. In *European Quantum Electron. Conf.*, page 19, June 2003.

[310] C. R. Mirasso, I. Fischer, M. Peil, and L. Larger. Optoelectronic devices for optical chaos communications. In J. Piprek, editor, *SPIE Proc.*, volume 5248 of *Semiconductor Optoelectronic Devices for Lightwave Communication*, pages 24–34, Orlando, FL, USA, September 2003.

[311] M. Peil, I. Fischer, and W. Elsäßer. A short external cavity semiconductor laser cryptosystem. *C. R. Physique*, 5(6):633–642, July–August 2004.

[312] S. Yanchuk, K. R. Schneider, and L. Recke. Dynamics of two mutually coupled semiconductor lasers: Instantaneous coupling limit. *Phys. Rev. E*, 69(5):056221, May 2004.

[313] M. Arizaleta Arteaga, M. López-Amo, J. Hernández, K. Koltys, A. Tabaka, H. Thienpont, and K. Panajotov. Spectral properties of edge-emitting semiconductor laser subject to optical feedback from extremely short external cavity. *Opt. Quantum Electron.*, 40(2-4): 69–81, March 2008.

[314] T. Heil, I. Fischer, W. Elsäßer, J. Mulet, and C. R. Mirasso. Chaos synchronization and spontaneous symmetry-breaking in symmetrically delay-coupled semiconductor lasers. *Phys. Rev. Lett.*, 86(5): 795–798, January 2001.

176

[315] J. Javaloyes, P. Mandel, and D. Pieroux. Dynamical properties of lasers coupled face to face. *Phys. Rev. E*, 67(3):036201, March 2003.

[316] S. Peters-Flynn. *Chaos Synchronisation Phenomena in Semiconductor Lasers*. PhD thesis, University of Wales, Bangor, UK, School of Informatics, September 2005.

[317] A. Croft, R. Davison, and M. Hargreaves. *Engineering mathematics*. Prentice Hall, 3rd edition, 2001. ISBN 0-130-26858-5.

[318] T. M. R. Ellis, I. R. Philips, and T. M. Lahey. *Fortran 90 programming*. Addison-Wesley, 1994. ISBN 0-201-54446-6.

[319] D. V. Anosov. Geodesic flows on closed Riemannian manifolds of negative curvature. *Proc. Steklov Inst. Math.*, 90:3–235, 1967.

[320] R. Bowen. Markov partitions for axiom A diffeomorphisms. *Amer. J. Math.*, 92(3):725–747, July 1970.

[321] S. Lea. *Chaos pass filtering in chaos communication systems*. PhD thesis, Bangor University, School of Electronic Engineering, 2010.

[322] G. C. Danielson and C. Lanczos. Some improvements in practical Fourier analysis and their application to X-ray scattering from liquids. *J. Franklin Inst.*, 233(4): 365–380, April 1942.

[323] G. C. Danielson and C. Lanczos. Some improvements in practical Fourier analysis and their application to X-ray scattering from liquids. *J. Franklin Inst.*, 233(5): 435–452, May 1942.

[324] W. H. Press, B. P. Flannery, S. A. Teukolsky, and W. T. Vetterling. *Numerical Recipes: The art of scientific computing*. Cambridge University Press, 1986. ISBN 0-521-30811-9.

[325] S. Sivaprakasam, P. S. Spencer, P. Rees, and K. A. Shore. Transition between anticipating and lag synchronization in chaotic external-cavity laser diodes. *Opt. Lett.*, 27(14):1250–1252, July 2002.

[326] S. Sivaprakasam, P. S. Spencer, P. Rees, and K. A. Shore. Regimes of chaotic synchronization in external-cavity laser diodes. *IEEE J. Quantum Electron.*, 38(9): 1155–1161, September 2002.

[327] R. Lang. Injection locking properties of a semiconductor laser. *IEEE J. Quantum Electron.*, 18(6):976–983, June 1982.

[328] F. Mogensen, H. Olesen, and G. Jacobsen. Locking conditions and stability properties for a semiconductor laser with external light injection. *IEEE J. Quantum Electron.*, 21(7):784–793, July 1985.

[329] J. Mørk, B. Tromborg, and J. Mark. Chaos in semiconductor lasers with optical feedback: Theory and experiment. *IEEE J. Quantum Electron.*, 28(1):93–108, January 1992.

[330] Yoshiro Takiguchi, Yun Liu, and Junji Ohtsubo. Low-frequency fluctuation induced by injection-current modulation in semiconductor lasers with optical feedback. *Opt. Lett.*, 23(17):1369–1371, September 1998.

[331] E. A. Viktorov and P. Mandel. Low frequency fluctuations in a multimode semiconductor laser with optical feedback. *Phys. Rev. Lett.*, 85(15):3157–3160, October 2000.

[332] A. Prasad, Y.-C. Lai, A. Gavrielides, and V. Kovanis. Low-frequency fluctuations in external cavity semiconductor lasers: understanding based on a simple dynamical model. *J. Opt. B: Quantum Semiclass. Opt.*, 3(4): 242–250, July 2001.

[333] G. H. M. van Tartwijk, A. M. Levine, and D. Lenstra. Sisyphus effect in semiconductor lasers with optical feedback. *IEEE J. Sel. Top. Quantum Electron.*, 1 (2):466–472, June 1995.

[334] M.-W. Pan, B.-P. Shi, and G. R. Gray. Semiconductor laser dynamics subject to strong optical feedback. *Opt. Lett.*, 22(3):166–168, February 1997.

[335] M. Fujiwara, K. Kubota, and R. Lang. Low-frequency intensity fluctuation in laser diodes with external optical feedback. *Appl. Phys. Lett.*, 38(4):217–220, February 1981.

[336] M. Fujiwara, K. Kubota, and R. Lang. Erratum: Low-frequency intensity fluctuation in laser diodes with external optical feedback. *Appl. Phys. Lett.*, 39(2):182, July 1981.

[337] J. Sacher, W. Elsäßer, and E. O. Göbel. Intermittency in the coherence collapse of a semiconductor laser with external feedback. *Phys. Rev. Lett.*, 63(20):2224–2227, November 1989.

[338] T. Sano. Antimode dynamics and chaotic itinerancy in the coherence collapse of semiconductor lasers with optical feedback. *Phys. Rev. A*, 50(3):2719–2726, September 1994.

[339] D. W. Sukow, J. R. Gardner, and D. J. Gauthier. Statistics of power-dropout events in semiconductor lasers with time-delayed optical feedback. *Phys. Rev. A*, 56 (5):R3370–R3373, November 1997.

[340] J. Mørk, B. Tromborg, and P. L. Christiansen. Bistability and low-frequency fluctuations in semiconductor lasers with optical feedback: A theoretical analysis. *IEEE J. Quantum Electron.*, 24(2):123–133, February 1988.

[341] A. Hohl, H. J. C. van der Linden, and R. Roy. Determinism and stochasticity of power-dropout events in semiconductor lasers with optical feedback. *Opt. Lett.*, 20(23):2396–2398, December 1995.

[342] D. Lenstra. Statistical theory of the multistable external-feedback laser. *Opt. Commun.*, 81(3–4):209–214, February 1991.

[343] Y. Takiguchi, H. Kan, and J. Ohtsubo. Modulation induced Low-Frequency Fluctuations in semiconductor lasers with optical feedback and their suppression by synchronous modulation. *Opt. Rev.*, 9(6):234–237, November–December 2002.

[344] K. Verheyden, K. Green, and D. Roose. Numerical stability analysis of a large-scale delay system modeling a lateral semiconductor laser subject to optical feedback. *Phys. Rev. E*, 69(3):036702, March 2004.

[345] M. S. Torre, C. Masoller, N. B. Abraham, and H. F. Ranea-Sandoval. Carrier dynamics in semiconductor lasers operating in the Low-Frequency Fluctuations regime. *J. Opt. B: Quantum Semiclass. Opt.*, 2(5):563–569, October 2000.

[346] M. G. Rosenblum, A. S. Pikovsky, and J. Kurths. Phase synchronization of chaotic oscillators. *Phys. Rev. Lett.*, 76(11):1804–1807, March 1996.

[347] J.-W. Shuai and D. M. Durand. Phase synchronization in two coupled chaotic neurons. *Phys. Lett. A*, 264(4): 289–297, December 1999.

[348] Z. Zheng and G. Hu. Generalized synchronization versus phase synchronization. *Phys. Rev. E*, 62(6):7882–7885, December 2000.

[349] D. Maza, A. Vallone, H. Mancini, and S. Boccaletti. Experimental phase synchronization of a chaotic convective flow. *Phys. Rev. Lett.*, 85(26):5567–5570, December 2000.

[350] J. Y. Chen, K. W. Wong, and J.-W. Shuai. *n:m* phase synchronization with mutual coupling phase signals. *Chaos*, 12(1):100–106, March 2002.

[351] M. Peil, T. Heil, I. Fischer, and W. Elsäßer. Synchronization of chaotic semiconductor laser systems: A vectorial coupling-dependent scenario. *Phys. Rev. Lett.*, 88(17):174101, April 2002.

[352] T. Heil, J. Mulet, I. Fischer, C. R. Mirasso, M. Peil, P. Colet, and W. Elsäßer. ON/OFF Phase Shift Keying for chaos-encrypted communication using external-cavity semiconductor lasers. *IEEE J. Quantum Electron.*, 38(9):1162–1170, September 2002.

[353] G. V. Osipov, B. Hu, C.-S. Zhou, M. V. Ivanchenko, and J. Kurths. Three types of transitions to phase synchronization in coupled chaotic oscillators. *Phys. Rev. Lett.*, 91(2):024101, July 2003.

[354] J. Sun and S.-Q. Zhu. Synchronization of chaotic intensities and phases in an array of n lasers. *Commun. Theor. Phys.*, 43(2):233–239, February 2005.

[355] V. Annovazzi-Lodi, M. Benedetti, S. Merlo, T. Perez, P. Colet, and C. R. Mirasso. Message encryption by phase modulation of a chaotic optical carrier. *IEEE Photon. Technol. Lett.*, 19(2):76–78, January 2007.

[356] A. Bogris, P. Rizomiliotis, K. E. Chlouverakis, A. Argyris, and D. Syvridis. Feedback phase in optically generated chaos: A secret key for cryptographic applications. *IEEE J. Quantum Electron.*, 44(2):119–124, February 2008.

[357] N. Schunk and K. Petermann. Noise analysis of injection-locked semiconductor injection lasers. *IEEE J. Quantum Electron.*, 22(5):642–650, May 1986.

[358] T. Heil, I. Fischer, and W. Elsäßer. Stabilization of feedback-induced instabilities in semiconductor lasers. *J. Opt. B: Quantum Semiclass. Opt.*, 2(3):413–420, June 2000.

[359] I. Kanter, N. Gross, E. Klein, E. Kopelowitz, P. Yoskovits, L. Khaykovich, W. Kinzel, and M. Rosenbluh. Synchronization of mutually coupled chaotic lasers in the presence of a shutter. *Phys. Rev. Lett.*, 98(15):154101, April 2007.

[360] J. S. Lawrence and D. M. Kane. Injection locking suppression of coherence collapse in a diode laser with optical feedback. *Opt. Commun.*, 167(1–6):273–282, August 1999.

[361] R. J. Jones, P. S. Spencer, and K. A. Shore. Controlling chaos in a semiconductor laser by external optical injection. In *IEE Proc. OptoElectron.*, volume 147, pages 67–70, February 2000.

[362] E. F. Manffra, I. L. Caldas, and R. L. Viana. Stabilizing periodic orbits in a chaotic semiconductor laser. *Chaos Solitons Fractals*, 15(2):327–341, January 2003.

[363] Y. Mitsuhashi. Polarization control of an antireflection-coated GaAlAs laser diode by an external optical feedback. *J. Appl. Phys.*, 53(12):9200–9201, December 1982.

[364] K. Otsuka and J.-L. Chern. High-speed picosecond pulse generation in semiconductor lasers with incoherent optical feedback. *Opt. Lett.*, 16(22):1759–1761, November 1991.

[365] K. Otsuka and J.-L. Chern. High-speed picosecond pulse generation in semiconductor lasers with incoherent optical feedback: erratum. *Opt. Lett.*, 17(10):763, May 1992.

[366] F. Rogister, A. Locquet, D. Pieroux, M. Sciamanna, O. Deparis, P. Mégret, and M. Blondel. Secure communication scheme using chaotic laser diodes subject to incoherent optical feedback and incoherent optical injection. *Opt. Lett.*, 26(19):1486–1488, October 2001.

[367] F. Rogister, D. Pieroux, M. Sciamanna, P. Mégret, and M. Blondel. Anticipating synchronization of two chaotic laser diodes by coherent optical coupling and its application to secure communications. *Opt. Commun.*, 207(1–6):295–306, June 2002.

[368] T. Heil, A. Uchida, P. Davis, and T. Aida. TE-TM dynamics in a semiconductor laser subject to polarization-rotated optical feedback. *Phys. Rev. A*, 68(3):033811, September 2003.

[369] R. Ju and P. S. Spencer. Dynamic regimes in semiconductor lasers subject to incoherent optical feedback. *IEEE J. Lightwave Technol.*, 23(8):2513–2523, August 2005.

[370] Y. Takeuchi, R. Shogenji, and J. Ohtsubo. Chaotic dynamics in semiconductor lasers subjected to polarization-rotated optical feedback. *Appl. Phys. Lett.*, 93(18):181105, November 2008.

[371] L. Khaykovich, T. Galfsky, Z. Shotan, and N. Gross. TE-TM coupled mode dynamics in a semiconductor laser subject to feedback with variably rotated polarization. *Opt. Commun.*, 282(10):2059–2061, May 2009.

[372] M. Ahmed. Longitudinal mode competition in semiconductor lasers under optical feedback: Regime of short-external cavity. *Opt. Laser Technol.*, 41(1):53–63, February 2009.

[373] S. Sivaprakasam, R. Saha, P. A. Lakshmi, and R. Singh. Mode hopping in external-cavity diode lasers. *Opt. Lett.*, 21(6):411–413, March 1996.

[374] T. Fujita, A. Schremer, and C. L. Tang. Polarization bistability in external cavity semiconductor lasers. *Appl. Phys. Lett.*, 51(6):392–394, August 1987.

[375] T. Fujita, A. Schremer, and C. L. Tang. Birefringence-induced polarization counter rotation in a semiconductor laser. *Appl. Phys. Lett.*, 51(19):1487–1489, November 1987.